uOttawa

L'Université canadienne
Canada's university

FACULTÉ DES ÉTUDES SUPÉRIEURES ET POSTOCTORALES

u Ottawa

L'Université canadienne
Canada's university

FACULTY OF GRADUATE AND POSDOCTORAL STUDIES

Andrew W. Cameron
AUTEUR DE LA THÈSE / AUTHOR OF THESIS

M.A.Sc. (Mechanical Engineering)
GRADE / DEGREE

Department of Mechanical Engineering
FACULTÉ, ÉCOLE, DÉPARTEMENT / FACULTY, SCHOOL, DEPARTMENT

Structure of a Low-Momentum Elevated Jet in a Cross-Flow

TITRE DE LA THÈSE / TITLE OF THESIS

Dr. Stavros Tavoularis
DIRECTEUR (DIRECTRICE) DE LA THÈSE / THESIS SUPERVISOR

Dr. Matthew Johnson
CO-DIRECTEUR (CO-DIRECTRICE) DE LA THÈSE / THESIS CO-SUPERVISOR

EXAMINATEURS (EXAMINATRICES) DE LA THÈSE / THESIS EXAMINERS

Dr. M. Yaras

Dr. W. Hallett

Gary W. Slater
Le Doyen de la Faculté des études supérieures et postdoctorales / Dean of the Faculty of Graduate and Postdoctoral Studies

Structure of a Low-Momentum Elevated Jet in a Cross-Flow

Andrew William Cameron

Thesis submitted to the Faculty of Graduate and Postdoctoral Studies
in partial fulfillment of the requirements for the degree of

MASTER OF APPLIED SCIENCE

in Mechanical Engineering

Ottawa-Carleton Institute for Mechanical and Aerospace Engineering
University of Ottawa
Ottawa, Canada

February 2008

Your file Votre référence
ISBN: 978-0-494-50859-6
Our file Notre référence
ISBN: 978-0-494-50859-6

Abstract

An elevated jet in a cross-flow is a free jet issuing orthogonally into a dominant cross-wind from a pipe extending above a ground-induced boundary layer. The present thesis is concerned with jets having low momentum-flux relative to the cross-flow. It presents flow visualization and velocity measurements conducted in a variable-speed, closed-circuit water channel.

Four major types of coherent structures were identified: von Kármán vortices, a pipe-end vortex, shear-layer vortices, and tendrils. The von Kármán vortices are similar to those shed by a finite cylinder with a free end. The pipe-end vortex is a stationary vortex forming immediately downstream of the pipe-end. The shear-layer vortices are formed by the Kelvin-Helmholtz instability in the mixing layer between the cross-flow and the jet. Finally, the tendrils are evolutions of sections of the shear-layer vortices, formed under certain conditions as the latter are stretched by the pipe-end vortex and move downstream.

The size of the pipe-end vortex is insensitive to the momentum-flux ratio as long as the latter is less than a critical value. For higher momentum-flux ratios, the pipe-end vortex grows in size and shifts beyond the free-end of the pipe. The Strouhal numbers of the shear-layer vortices and the tendrils increase drastically as the momentum-flux ratio decreases. The shear-layer vortices, marking the jet fluid, move away from the pipe exit upon their

generation, then reverse direction as they pass over the pipe-end vortex, while accelerating in the streamwise direction until their velocities approach the cross-flow speed.

A vorticity balance for each type of the vortices has been attempted. The von Kármán vortices obtain their vorticity from the pressure gradient along the outer surface of the pipe. The pipe-end vortex acquires its vorticity from the shear-layer vortices and generates some vorticity in a pressure gradient on the outer surface of the pipe as well. The shear-layer vortices acquire their vorticity from the cross-flow fluid flowing over the edge of the upstream pipe tip as well as from the vorticity inside the pipe from the jet flow. The vorticity in the tendrils originates in the shear-layer vortices.

Acknowledgements

First and foremost, I would like to thank Dr. Stavros Tavoularis and Dr. Matthew Johnson for their enthusiasm toward this project and welcoming me to the University of Ottawa. Their financial and academic support throughout this independent study followed by their strong and extremely diligent editing support are what made this thesis possible. Being able to work with such gifted and hard-working engineers is a special experience that I am quite honoured to have had. Of particular note was the extremely hard work that Dr. Tavoularis dedicated to the editing process toward the end of the project, often late into the night. I also greatly appreciate their flexibility in understanding my taking a leave of absence during the writing process. The experience I had while I was away is one that I will cherish for a lifetime and would have had great difficulty accomplishing later in life.

Dr. Warren Dunn was also a great help throughout the production of this thesis. He took a good deal of time during his post-doctoral experimentation to orient me through the fluid mechanics laboratory. His diligent documentation throughout his doctoral degree was also a great help in experimental problem solving when using the equipment he meticulously maintained. It is also greatly appreciated that he continued to assist after he had moved on with his career by providing any information and advice he could through my occasional mailings.

Dr. Sean Bailey was also a great help in the laboratory during his experimentation for his doctoral degree. He would often take time out of his day to assist in fixing old equipment, locating lost equipment, troubleshooting problems, helping with Matlab functions and providing moral support.

The ongoing support of fellow masters students Bill Stannus and Aaron Price was also a great help. Mr. Stannus and I worked through our in class requirements together and continued assisting each other where we could through our respective experimental trials. He was very generous with his Matlab skills when I was first learning the program. Mr. Price was also very generous volunteering his time and advice assisting me with efficient referencing practices, Matlab functions, general thesis tips and general support and encouragement.

Finally I would like to thank my encouraging family. My mother, brother and stepfather have been supportive throughout the process.

Table of Contents

List of Figures

List of Tables

Nomenclature

a	dimension a
b	dimension b
c	dimension c
D	outer diameter of the pipe
D_{AB}	diffusion coefficient
d	inner diameter of the pipe
f	frequency
L_e	entrance length
Q	pipe flow rate
q, $\vec{V}$	fluid velocity
R	momentum-flux ratio $\left(R = \frac{\rho_j q_j^2}{\rho_\infty q_\infty^2} \right)$
Re	Reynolds number
r	velocity ratio
r^2	coefficient of determination

St_d Strouhal number $\left(St = \frac{f \cdot d}{q}\right)$

v_v y-component of velocity of the vortex core

w_v z-component of velocity of the vortex core

Δt time difference between frames

ν kinematic viscosity

ρ fluid density

$\vec{\omega}$ vorticity

Subscripts

D calculation performed including outer diameter of the pipe

d calculation performed including inner diameter of the pipe

j pertaining to the jet fluid

x, y, z components in x-, y-, z- directions, respectively

∞ pertaining to the cross-flowing fluid

Other notation

$(\vec{\cdot})$ vector quantity

Chapter 1 Introduction

1.1 Motivation

The jet in a cross-flow is a fundamental flow configuration that has a variety of engineering applications such as dispersion of pollutants into the atmosphere, cross-stream fuel injection, effluent streams in rivers and lakes, and gas flaring among many others. A better understanding of the mechanisms that govern the mixing of the fluids involved in these situations would assist current efforts towards making these processes safer, more efficient and more environmentally responsible.

Waste gases are produced in most industrial and domestic processes. If the concentration of pollutants in these gases at the source is considered unsafe for human exposure or has the potential for adverse environmental impact, the pollutant must be neutralized or its concentration must be reduced. Because the process of neutralizing chemical substances often produces other waste gases and also requires additional resources, it is common to reduce undesirable concentrations by mixing the waste gas with air at or near the source. Elevating the emission of waste gases far above the ground surface is a widespread method to maintain the ground-level concentration pollutants at acceptable levels. Early studies in the field focused on the statistical modelling of dispersion by the use of Gaussian distributions (Wark and Warner, 1981). Ideal venting conditions for sufficient

concentration reduction by dispersion entail low pollutant emission concentrations, a relatively low density of the emitted gas, and, most importantly, a wind velocity that is sufficiently lower than the emission velocity from the stack to allow the vented gasses to escape the low-pressure region on the downstream side of the stack. When such conditions do not occur, more detailed analyses of the dispersion mechanisms at work need to be considered.

One particular engineering application that motivated the present study was oil-field flares. During the extraction of oil from subterranean reserves, dissolved gases are released from the oil when it is brought to atmospheric pressure at the surface. In many cases this gas is burned on site in an open flame stabilized on an elevated flare stack; this practise is commonly referred to as flaring. Combustion is meant to moderate the environmental impact of released substances and is a simple and generally safe way of disposing of flammable gases. However, recent studies have shown that the combustion that occurs is not always complete and emissions of unburned fuel and other combustion by-products can occur (Johnson and Kostiuk, 2000; 2002; Johnson et al., 2001).

When wind blows across the flame with sufficient speed, such that the ratio of the momentum flux of the fluid exiting the stack to that of the cross-flowing wind drops to sufficiently low levels, the combustion efficiency of the flare is reduced and emissions of unburned gases increase (Johnson and Kostiuk, 2000). Johnson et al. (2001) proposed a mechanism for fuel stripping in these flames, in which coherent structures in the jet in a cross-flow draw unburned fuel from the flame and counter the buoyancy force of the lighter-than-air fuel. In the case of a non-reacting jet in cross-flow, the action of coherent structures

can potentially transport high-concentration jet fluid to the ground level rather than allowing it to rise and become diluted.

A literature survey has revealed that even non-reacting flows from elevated sources in cross-streams at relatively low momentum-flux ratios have not been adequately studied experimentally, particularly with an emphasis on their vortical structures. The research presented in this thesis addresses this specific problem. In the interest of experimental clarity and simplicity, the present work is focussed on the structure of non-reacting jets in a cross-flow. To ensure that the structures could be visualized relatively easily, experiments were performed in a water channel. Despite the relatively low flow velocities that may be achieved in this water tunnel, the experimental Reynolds number range was comparable to that achievable in low-speed wind tunnels, because the kinematic viscosity of water is about 15 times lower than that of air under standard atmospheric conditions. To further simplify the conditions as well as permitting comparisons with previous research on similar flow arrangements, the jet fluid was made to be neutrally buoyant with respect to the cross-flowing fluid.

One limitation to testing in a neutrally buoyant, non-reacting, water environment is that the applicability of conclusions to the original reacting flow would be reduced with increasing distance downstream of the pipe. In a combusting flow, as fluid travels farther from the burner and the combustion reactions take place, the jet fluid temperature would increase significantly above that of the cross-flowing fluid; consequently, the jet fluid density would drop significantly below that of the cross-flow fluid, and buoyancy would play a role in the process. For this reason, this study will focus generally on the formation of structures

in the near field and will not pay significant attention to the evolution of the structures as they convect far downstream.

1.2 Objectives

The primary objective of this thesis is to gain further insight into the near-field, large-scale structure of an elevated jet issuing into a cross-stream with significantly higher momentum flux than the jet. This will be performed by both qualitative and quantitative means, including flow visualization and velocity measurement techniques. Focus will be placed on coherent vortical structures thought to be responsible for transporting jet fluid towards the "ground" on the lee side of the pipe.

1.3 Thesis Organization

This thesis has been separated into eight chapters. The motivation and objectives are outlined in Chapter 1. A review of findings of past researchers on topics relevant to this study is shown in Chapter 2, and the physical set-up of this experiment is described in Chapter 3. Chapter 4 shows some preliminary results that assisted the remaining experimentation. Chapter 5 offers an initial overview of the structure of the flow based on flow visualization. These results are used for planning a series of quantitative measurements which are presented in Chapter 6. Chapter 7 discusses the findings of the previous chapters in greater depth and finally conclusions and recommendations for future work are summarized in Chapter 8.

Chapter 2 Literature Review

As will be shown in the following sections, the complex flow configuration of a jet issuing within a cross-stream has been studied extensively. However, the vast majority of these studies focus on jets issuing from an orifice at the wall and their interaction with the boundary layer which developed on the same wall. An elevated jet is one that is released from the orifice of a pipe located far from the wall. It can thus be considered as free of interactions with the boundary layer on that wall.

An important parameter used by previous researchers to categorize elevated jets in cross-flows is the simplified momentum-flux ratio (Huang and Hsieh, 2002; 2003; Huang and Lan, 2005; Moussa et al., 1977), defined as the ratio of a characteristic momentum-flux of the pipe flow to the momentum-flux of the cross-flow:

$$R = \frac{\rho_j q_j^2}{\rho_\infty q_\infty^2} \tag{1}$$

where ρ_j and ρ_∞ are the densities of the jet fluid and the free stream fluid, respectively, and q_j and q_∞ are the jet fluid bulk velocity and the free stream velocity, respectively. The value of the momentum-flux ratio is a measure of the relative strength of the jet compared to the free stream and plays a significant role on the structure of the flow. Here, jets with R less than approximately 0.3 are considered to be of low momentum, whereas those with R greater than approximately 0.6 are considered to be of high momentum. Wall-issued jets in a cross-flow

of both high and low momentum-flux ratios have been studied fairly extensively. There has also been a fair amount of research on high-momentum elevated jets in a cross-flow, but comparatively very little on low-momentum elevated jets in a cross-flow.

A survey of literature pertaining to the research interests of this thesis is presented in this section. A more comprehensive survey for a broader spectrum of applications has been presented by Margason (1993).

2.1 Vorticity Dynamics

The following equation describing the evolution of vorticity, $\vec{\omega}$, in viscous flow of an incompressible fluid can be derived by applying the curl operation on the momentum (Navier-Stokes) equation, as demonstrated by Batchelor (1967)

$$\frac{D\vec{\omega}}{Dt} = \vec{\omega}\cdot\nabla\vec{V} + \nu\nabla^2\vec{\omega} \tag{2}$$

By expanding the material derivative, the same equation can also be presented as

$$\frac{\partial\vec{\omega}}{\partial t} = -\vec{V}\cdot\nabla\vec{\omega} + \vec{\omega}\cdot\nabla\vec{V} + \nu\nabla^2\vec{\omega} \tag{3}$$

to show more distinctly the terms which affect the temporal rate of change of vorticity at a fixed location, which is the single term on the left-hand side. The first term on the right-hand side represents the change of vorticity due to convection, the second term represents the change of vorticity due to deformation of vortex lines, and the third term represents the

change of vorticity due to viscous diffusion (Batchelor, 1967; Panton, 2005). This equation becomes relevant in the discussions below pertaining to the evolution of vorticity through the flow.

Morton (1984) has demonstrated that, in contrast to frequent descriptions in the literature, vorticity is not generated by the no-slip condition on a solid wall surface, but it is rather generated by tangential pressure gradients (an example illustrating this process will be presented shortly). Viscous redistribution of the vorticity the instant following generation occurs, which is often misunderstood as the generation mechanism. The analysis by Morton reinforces the long-standing evidence that vorticity cannot be generated within a homogeneous fluid and its generation must take place at solid surfaces.

Another key point in the article by Morton is that the only mechanism that exists for the destruction of vorticity within a fluid is cross-diffusive annihilation, by which fluid regions with vorticity of opposite signs diffuse into each other, cancelling the vorticity of each other. In contrast to previous assertions that vorticity can diffuse into a surface, Morton suggests that it is the pressure gradient on the surface which generates vorticity in the opposing direction, thereby countering the vorticity of the opposite sign.

As an example, consider a flow in the x-direction, which develops a boundary layer on a plane wall in the x-y plane. Assuming the no-slip condition at the wall, the x-component of the Navier-Stokes equation is reduced to

$$\frac{\partial p}{\partial x} = \mu \frac{\partial^2 u}{\partial z^2}. \tag{4}$$

In a similar fashion, the *x*-, *y*- and *z*- components of the vorticity vector may be reduced to, respectively,

$$\omega_x = 0 \tag{5}$$

$$\omega_y = \frac{1}{2}\frac{\partial u}{\partial z} \tag{6}$$

$$\omega_z = 0. \tag{7}$$

Equation 6 may also be expressed as

$$2\frac{\partial \omega_y}{\partial z} = \frac{\partial^2 u}{\partial z^2}. \tag{8}$$

Substituting equation 8 into equation 4, one ends up with the relation

$$\frac{\partial \omega_y}{\partial z} = \frac{1}{2\mu}\frac{\partial p}{\partial x}, \tag{9}$$

which shows that, in this example, it is the streamwise pressure gradient that generates the *y*-component of vorticity along the plane wall.

Applying the curl operation on the continuity equation for incompressible fluids, one obtains the following solenoidality condition of vorticity (Rosenhead, 1963)

$$\frac{\partial \omega_x}{\partial x} + \frac{\partial \omega_y}{\partial y} + \frac{\partial \omega_z}{\partial z} = 0. \tag{10}$$

This equation states that, if one considers an elementary control volume with faces normal to the x, y, z axes, respectively, and there is a net positive flux of ω_x, for example, vorticity through the faces normal to the x-axis ($\partial\omega_x / \partial x > 0$), then there must be a negative flux of vorticity through at least one of the other two pairs of opposite faces ($\partial\omega_y / \partial y + \partial\omega_z / \partial z < 0$). As mentioned previously, net vorticity loss within a control volume can only occur by cross-diffusive annihilation. For example, in fully developed plane Poiseuille flow, vorticity is continuously being generated on the opposite walls; however, the net circulation per unit length of the channel is zero, because vorticity of opposite signs diffuses from the two walls towards the channel centre plane, where it vanishes by cross-diffusive annihilation (Morton, 1984).

2.2 Wall-Issued Jets in a Cross-Flow

The majority of available literature on jets in cross-flows pertains to jets that issue within the boundary layer developing on a plane wall; these are commonly referred to as wall-issued jets. Though they differ from elevated jets in their overall structure, much learned from wall-issued jet studies was used to help the understanding of elevated jets. A partial list of publications that focused upon the vortex structures that exist in wall-issued jets in cross-flows is shown in Table 1.

Early work by Andreopoulos (1985) was performed on a wall-mounted jet with a relatively low momentum-flux ratio of $R = 0.25$ that was turbulent, not fully developed at the jet exit, and issued into a turbulent boundary layer. Andreopoulos introduced a small

temperature difference to distinguish the jet fluid from cross-flow fluid and provided a rough sketch of two types of vortical structures, a "horseshoe vortex" and vortex rings, whose characteristics he found to depend on the Reynolds number of the jet. The "horseshoe vortex" was a result of the adverse pressure gradient of the slowing cross-flow fluid when it reached the leading edge of the jet. The vortex wrapped around the leading edge of the jet exit and extended in a streamwise direction downstream on either side of the jet exit. The vortex rings were created in the shear layer between the cross-flow fluid and the jet fluid.

A mainly qualitative study of the structure of wall-issued jets with momentum-flux ratios in the range from 4 to 100 was performed by Fric and Roshko (1994). Work done by these researchers was carried out in an open-circuit wind tunnel, in which they performed flow visualization either by placing smoke wires on different planes at different orientations relative to the cross-flow, or by releasing smoke into the jet flow. Fric and Roshko identified four major types of structures and illustrated them in a schematic representation shown in Figure 1, which has been reproduced with various adaptations by many subsequent researchers. Though the presence of structures referred to as the *counter-rotating vortex pair*, *jet shear-layer vortices*, *horseshoe vortices*, and *wake vortices* has not been disputed by other researchers, the origin of these structures remains a topic of argument. There is universal agreement, however, that the *jet shear-layer vortices* are a result of the Kelvin-Helmholtz instability, with the vorticity being present in the jet fluid before it exits into the cross-flow. Fric and Roshko concluded from their study that the wake vortices were formed by the rolling-up of the vorticity present in the wall-induced boundary layer to connect with the vorticity in the counter-rotating vortex pair.

The majority of research on the structures of the wall-issued jet in a cross-flow pertains to the *counter-rotating vortex pair*. At lower momentum-flux ratios, this structure is not as prominent; it does not appear in the analysis of Andreopoulos (1985) nor in the subsequent low-momentum flux study by Gopalan et al. (2004). It is therefore not of particular concern in this study.

Moussa et al. (1977) and Smith et al. (1993) suggest that the *wake vortices* originate in the jet itself. The momentum-flux ratio used by Moussa et al. was approximately 12 and the ones used by Smith et al. were in the range from 36 to 196. Later, Smith and Mungal (1998) performed planar laser-induced fluorescence (PLIF) measurements and statistical analyses and agreed, but only partially, with the conclusion of Fric and Roshko that the vorticity of the wake vortices originates in the boundary layer. Smith and Mungal confirmed such agreement only for momentum-flux ratios less than 225. For momentum-flux ratios higher than this value, they concluded that the vorticity of the wake structures is shed from the jet. A PLIF image from their research showing the jet fluid in the wake structures is reproduced in Figure 2. These researchers refer to the *counter-rotating vortex pair* as developing within the near-field region, defined by $x < 0.2\, R{\cdot}d$, where x is the streamwise axis, R is the momentum-flux ratio, and d is the jet diameter. In the far field, the *counter-rotating vortex pair* is said to be developed.

Many other researchers have experimented with wall-issued jets in cross flows. Kelso et al. (1996; 1998), Sivadas et al. (1997), Camussi et al. (2002) and Gopalan et al. (2004) have further studied the characteristics of various structures detailed by Fric and Roshko, in terms of choice of relevant parameters, structure generation mechanisms and

structure evolution. Other researchers, including Hasselbrink and Mungal (2001), Su and Mungal (2004) and Yuan and Street (1998) have examined the shape of the centreline of the jet and the physical mechanism causing its bending and overall shape.

2.3 Finite Cylinders in a Cross-Flow

Studies of flow past finite cylinders are of interest to the present work because they describe the wake of the cylinder, and particularly the three-dimensional flow structure near the free end of the cylinder. An extensive review of flows past cylinders, including finite ones with a free-end in the flow, has been given by Zdravkovich (1997; 2003).

The distinct flow pattern near the free end of the cylinder is the formation of a streamwise trailing vortex pair, whose sense of rotation is such that it tends to move fluid on the centreplane towards the base of the cylinder. This vortex pair is generated by downwash, associated with the low pressure in the wake of the cylinder. The trailing vortices are illustrated in Figure 3, taken from the article by Kawamura et al. (1984). This pattern has been described by Kawamura et al. (1984), Park and Lee (2000; 2004), Roh and Park (2003), Sumner et al. (2004) and Fröhlich and Rodi (2004) among others.

The structure of a finite cylinder wake depends strongly upon the aspect ratio, defined as the ratio of the cylinder length and its diameter. For aspect ratios lower than a critical value, the wake does not contain a von Kármán vortex street. The critical aspect ratio depends weakly on the thickness of the boundary layer at the base of the cylinder, according to a relationship given by Kawamura et al. (1984). As can be seen in Figure 4, when the

ratio of boundary layer thickness to cylinder diameter is lower than 0.2, the critical aspect ratio is just below 7. For aspect ratios higher than the critical value, von Kármán vortices are present and are inclined away from the cylinder toward the free end due to the downwash; this can be seen in Figure 3.

2.4 Elevated Jets in a Cross-Flow

As previously mentioned, relatively little research has been conducted on elevated jets in cross-flows. Early research on this topic dealt chiefly with buoyant plumes released into stratified atmospheres with the objective to study pollution dispersion. These studies were primarily concerned with far field concentrations of effluent at various locations of the flow (Briggs, 1969; Overcamp and Ku, 1986; Tatom, 1986).

Moussa et al. (1977) performed a set of experiments in air using hot-wire anemometry. They performed basic structural studies of both wall-issued and elevated jets in cross-flows by sliding a "skirt" extending 2.5 pipe diameters upstream of the pipe axis either flush with the pipe tip or far away from the pipe tip. They alluded to the *counter-rotating vortex pair* and the *wake vortices* subsequently mentioned by Fric and Roshko (1994) and discussed previously, albeit for both wall-issued and elevated jets in cross-flows.

Eiff and Keffer (1997a; 1997b; 1999) and Eiff et al. (1995) performed a series of experiments and observed transient structures that existed seven pipe diameters downstream of the pipe axis. These experiments were performed in air, mainly at a momentum-flux ratio of 9 and a Reynolds number of the cross-flow of 22 000, although in some cases the

momentum-flux ratio dropped to values as low as 2.25. Velocity measurements were taken with hot-wire anemometers and the signals were analysed by computing the FSTIF (fine scale turbulence intensity factor) and identifying coherent structures using pattern recognition techniques. They identified, within their elevated jet set-up, the structures that had previously been identified in wall-issued jets. These included the *counter-rotating vortex pair*, which was present and acted as a centre for much of the vorticity of the flow pattern. *Jet-wake vortices* also appeared in this flow; however, they were clearly formed by a mechanism different from the one proposed by Fric and Roshko as there was no plane wall boundary layer present in the elevated jet arrangement. von Kármán vortices were also detected, shed from the pipe from which the jet was emanating. These authors found that a lock-in coupling existed between the stack-wake vortices (i.e., the von Kármán vortices) and the jet-wake vortices as shown in Figure 5. These authors also detected *shear-layer vortices* in the flow, which were similar to those found by Fric and Roshko (1994). It was discovered that a lock-in coupling also existed between these shear-layer vortices and the jet-wake vortices, as shown in Figure 6 in which the two vortex types are seen to connect to each other following their separate generations. Eiff and Keffer also pointed out that the ratio of the outer and inner diameters of the pipe was a critical parameter in determining the structure of the flow. For cases having values of this ratio lower than 0.6, the lock-in coupling between the jet-wake vortices and the von Kármán vortices no longer occurred.

Huang and Hsieh (2002; 2003) and Hsieh and Huang (2003) studied flows over a wider range of momentum-flux ratios than those examined by Eiff and Keffer. They also performed their experiments in air, but reported both flow visualization results and

simultaneous time-averaged laser Doppler velocimetry (LDV) measurements. They used a mineral oil vapour mist excited by a laser sheet for flow visualization and seeded both the cross-flow fluid and the jet fluid with particles for the LDV measurements. These authors identified four regimes of the jet in a cross-flow, which depended on the value of the momentum-flux ratio. In order of increasing momentum-flux ratio, these were the *downwash flow* for $R < 0.9$, the *crosswind-dominated flow* for $0.9 < R < 2$, the *transitional flow* for $2 < R < 6$, and the *jet-dominated flow* for $R > 6$.

Huang and Lan (2005) concentrated on transient structures, specifically those identified by Fric and Roshko (1994) as *jet shear-layer vortices*. They used the same experimental equipment as Huang and Hsieh and conducted tests for the range of momentum-flux ratios from 0.08 to 1.26. The Reynolds number of the cross-flow was generally kept at 2051, but ranged up to 3692 to allow comparisons of frequency data. Adjustment of the momentum-flux ratio was made by changing the jet Reynolds number. Huang and Lan used high-speed cameras to capture sharp images in fast succession. They observed different types of vortices which they categorized into five different regimes, referred to as *mixing-layer type vortices* for $0.08 < R < 0.15$, *backward-rolling vortices* for $0.15 < R < 0.3$, *forward-rolling vortices* for $0.3 < R < 0.5$, *swing-induced mushroom vortices* up to $0.5 < R < 1$, and *jet-type vortices* for $R > 1$. As shown in Figure 7, the mixing-layer type vortices are those that are typical of a Kelvin-Helmholtz instability occurring at a shear-layer between two fluids of different velocities. The vortices roll in a "forward" direction with their cross-flow sides moving faster than the jet-fluid sides. The backward-rolling vortices occur when the tips of the mixing-layer type vortices have a sufficiently high

velocity so that they move faster than the cross-flow and begin rolling in the opposite direction. The vortices from the forward-rolling regime begin rolling in the same direction as the mixing-layer type vortices at a higher momentum-flux ratio. The swing-induced mushroom vortices are produced by a peculiar swinging motion of the jet, whereby vortices with a mushroom-like cross-section are formed by a rapid, periodic swing of the jet within the plane of symmetry. Finally, jet-type vortices show the tendency of the flow towards the formation of the familiar free-jet vortices. The latter three vortex regimes discussed by Huang and Lan are not relevant to this thesis as they occur at momentum-flux ratios much higher than those in the present work.

A partial list of references that focused upon the structures that exist within elevated jets in a cross-flow is presented in Table 1.

2.5 Literature Survey Summary

Though many aspects of jets in a cross-flow have been studied, the specific characteristics of very low momentum elevated jets in a cross-flow have not yet been studied in any detail. No previous studies pertaining to elevated jets in cross-flows have examined the flow regime for momentum-flux ratios lower than 0.03. The majority of elevated jet in a cross-flow studies have focused on farther field aspects and few on the generation of coherent structures in the vicinity of the pipe. No studies have yet focused upon the evolution of structures in the near field within a few diameters downstream of the pipe.

Author(s)	Range of R	Range of Re_j	d/D	Medium	Structures studied	Other Structures mentioned	Technique used	Comments/Conclusions
Elevated jet in cross-flow: analyses of coherant structures								
Moussa, Trischka, Eskinazi (1977)	12.11	14 600	0.93	Air	Counter-rotating vortex pair, jet-wake vortices (not explicitly named)		Hot wire anemometry	Comparisons drawn between basic wall-issued and elevated jets in cross-flows
Eiff, Kawal, Keffer (1995)	9	22 000	0.63	Air	Jet-wake vortices von Kármán structures		Hot wire and pattern recognition technique	Lock-in between wake vortices and von Kármán structures
Eiff, Keffer (1996)	9	20 000	0.63	Air	Jet-wake vortices von Kármán structures	Counter-rotating vortex pair	Hot wire and pattern recognition technique	Mentions previous lock-in conclusion between jet wake structures and stack-wake structures, further discusses their interation with the CRVP
Eiff, Keffer (1997)	9	22 000	0.63	Air	Shear-layer vortices ("Ring vortices") Jet-wake vortices		Hot wire and pattern recognition technique	Lock-in between ring vortices and wake vortices
Eiff, Keffer (1999)	2.25 - 36	7500 - 60 000	0.50 - 0.63	Air	Jet-wake vortices von Kármán structures		Hot wire and pattern recognition technique	Confirming lock-in between stack-wake and jet-wake vortices over other parameters
Huang, Hsieh (2002)	0.015 - 25	2074	0.78	Air	Time-averaged LSV, time averaged overall flow		LDV and flow visualization	
Huang, Hsieh (2003)	0.015 - 25	2074	0.78	Air	Time-averaged LSV, time averaged overall flow		LDV and flow visualization	Refined study of evolution of regimes set out in previous paper
Hsieh, Huang (2003)	9.37	2074	0.78	Air	Time-averaged structure		LDV and flow visualization	
Canepa (2004)	-	-	-	-	-	Counter-rotating vortex pair	-	Lit survey talking about downwash velocity due to the CRVP
Huang, Lan (2005)	0.04 - 1.26	2051 - 4594	0.78	Air	Shear-layer vortices	"Horseshoe-like vortices" is used to describe shear-layer vortices (tendrils)	LDV and flow visualization	Sorted shear-layer structures into regimes
Wall-issued jet in cross-flow: analyses of coherant structures								
Andreopoulos (1985)	0.25 - 25	1400 -83 000	-	Air	Horseshoe, "bound vortex"		Hot wire and flow visualization	Exploration to structures' behaviour through ranges of R
Sivadas, Pani, Bütefisch, Meier (1997)	15.21 - 60.84	600 - 2300	-	Air			Flow visualization	Investigated hole shape effect on CRVP
Yuan, Street (1998)	4 - 10.89	1050 - 2100	-	CFD			LES	Entrainment of cross-flow fluid is jet turning mechanism
Kelso, Lim, Perry (1996)	25	750 - 1600	-	Air/ Water	Counter-rotating vortex pair		Flow visualization	Details on origin of CRVP
Yuan, Street, Ferziger (1999)	4 - 10.89	1050 - 2100	-	CFD	Near-field structures, counter-rotating vortex pair, Wake vortices	Horseshoe vortex	LES	Identified structures within the jet core before the formation of CRVP
Gopalan, Abraham, Katz (2004)	0.25 - 6.25	19 000	-	Air	Shear-layer		PIV	BL interation with shear-layer vortices, details on structure of flow
Su, Mungal (2004)	32.49	900	-	Air	Counter-rotating vortex pair, wake vortices, horseshoe structures, shear-layer structures		PIV and PLIF	Details on scaling of flow field (not focussed on structures)

Table 1 – Partial list of studies of coherent structures in elevated and wall-issued jets in cross-flows

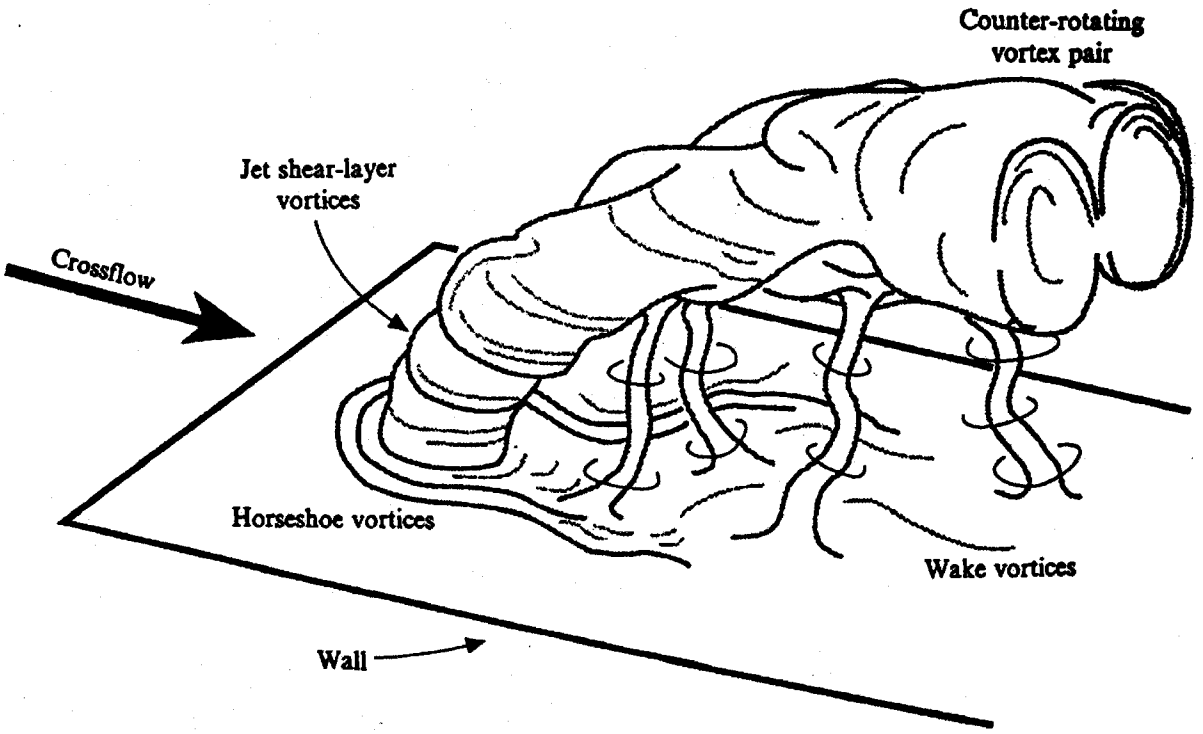

Figure 1 – Types of vortical structures in a wall-issued jet in a cross-flow (Fric and Roshko, 1994)

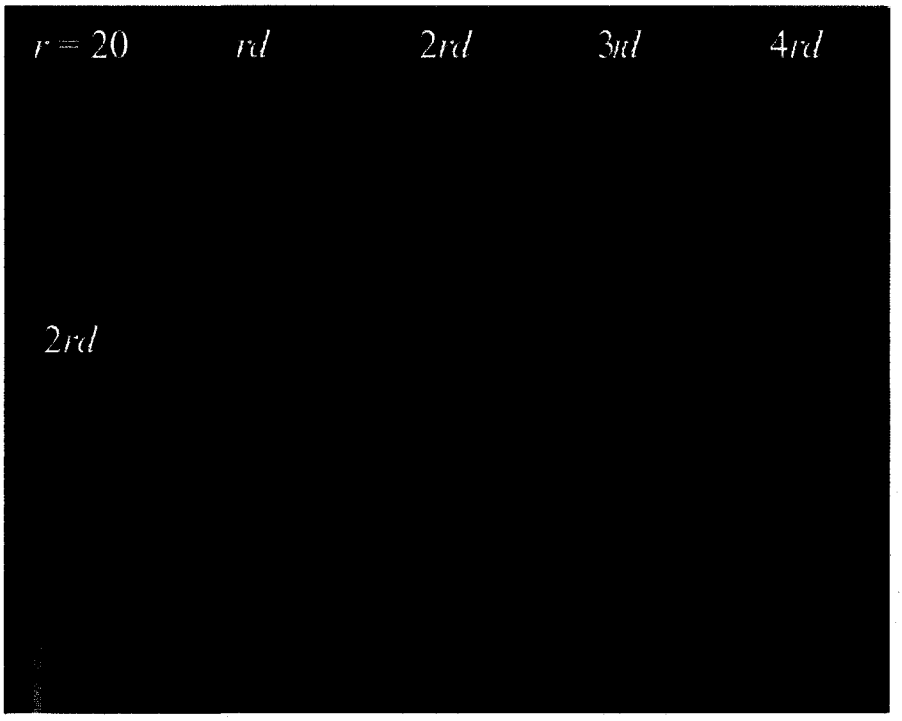

Figure 2 – Image displaying jet fluid in wake structures (Smith and Mungal, 1998) (d = 20 mm, R = 400, Re_j = 16 600)

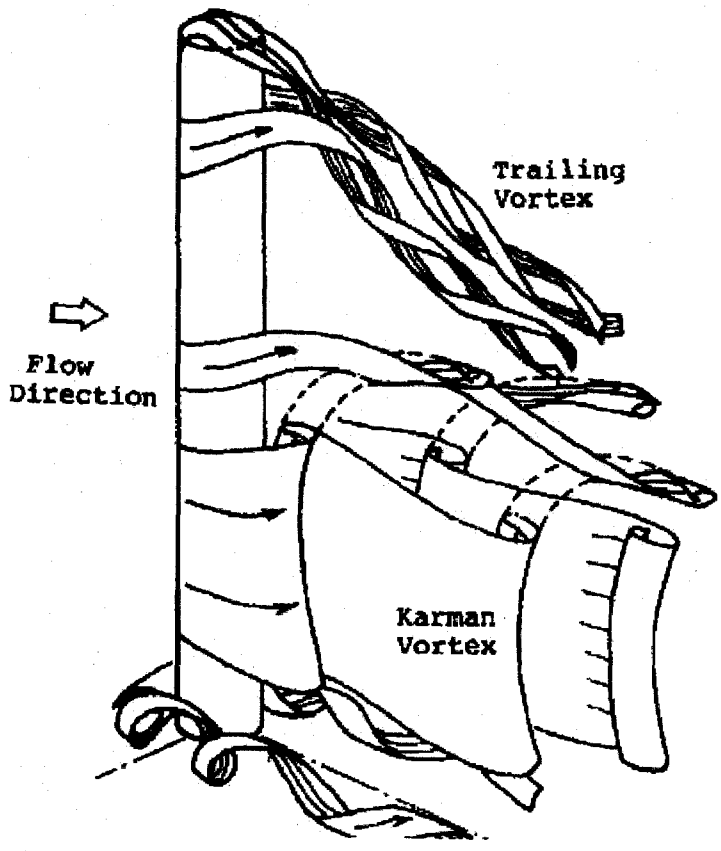

Figure 3 – Coherent structures behind a tall, slender finite cylinder (Kawamura et al., 1984)

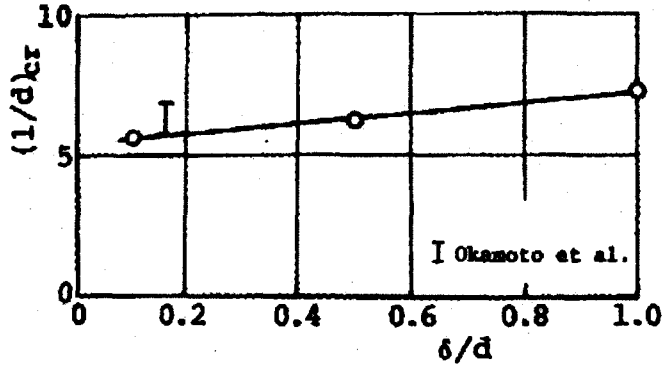

Figure 4 – Critical finite cylinder slenderness ratio (Kawamura et al., 1984)

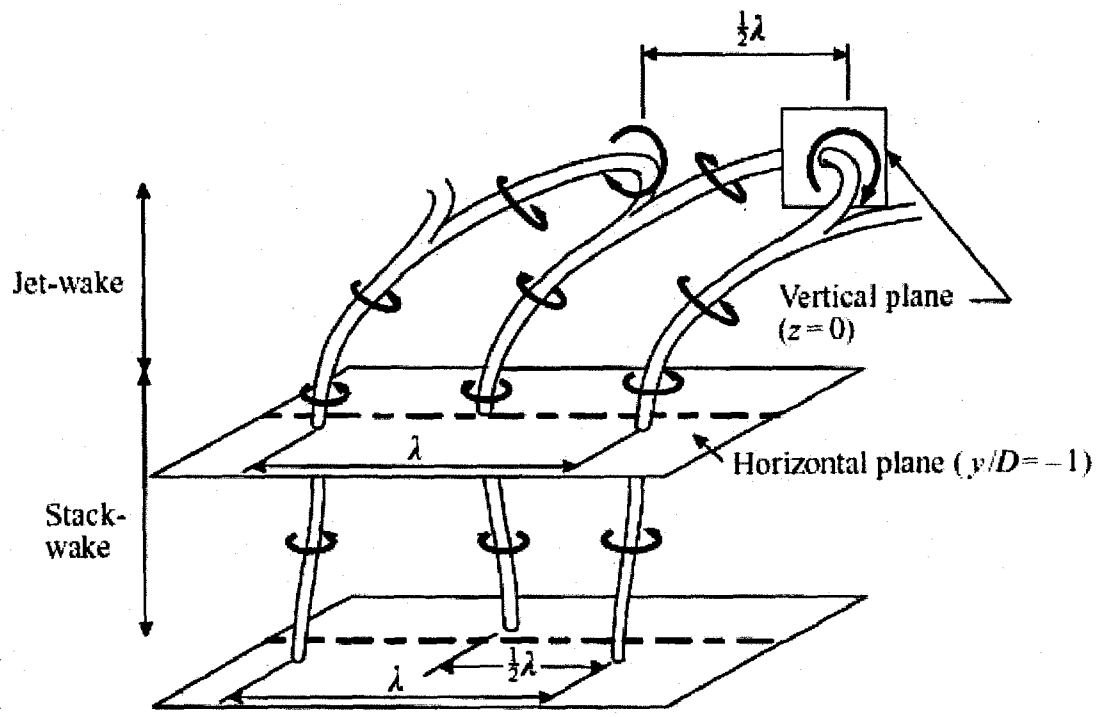

Figure 5 – Illustration of the lock-in coupling of the stack-wake and jet-wake structures (Eiff and Keffer, 1997a)

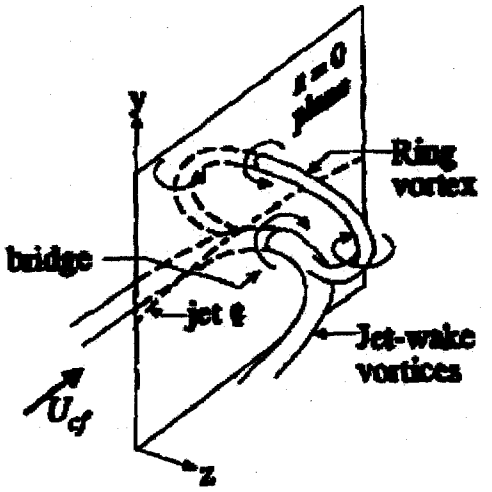

Figure 6 – Illustration of the lock-in coupling of the jet-wake and ring structures (Eiff and Keffer, 1997b)

a) mixing-layer type vortices

b) backward-rolling vortices

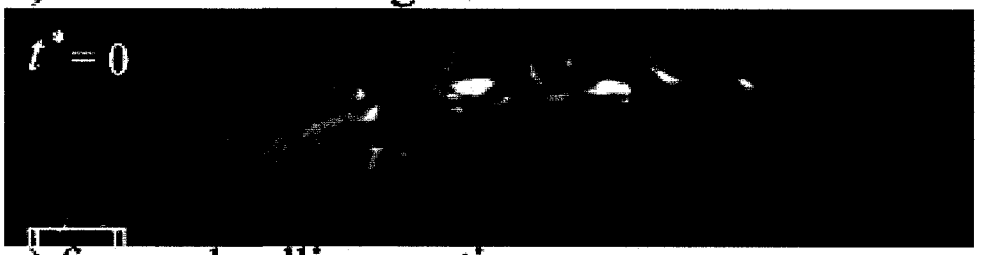

c) forward-rolling vortices

Figure 7 – Shear-layer vortex regimes (Huang and Lan, 2005)

Chapter 3 Experimental Facility, Instrumentation and Measurement Procedures

3.1 Water Channel

All experimental work was conducted in the recirculating, variable-speed water channel in the University of Ottawa Fluid Mechanics Laboratory. Details of the facility can be found in the theses by Dunn (1997) and Kislich-Lemyre (2002). The channel, shown in Figure 8, had a free surface in the test section that was approximately 4 m long and 0.50 m wide and had a maximum water depth of 0.75 m. The test section was kept with a water depth of 0.60 m throughout all experiments, giving the channel an approximate total water volume of 15 m^3. The flow was produced by an axial flow pump (Cascade Pump Company, Santa Fe Springs, California, USA) that was 0.30 m (12 in) in diameter. The pump was driven by an electric motor (General Electric) rated at 5.6 kW (7.5 hp). The motor speed was regulated by a frequency controller (Siemens Relcon Q2000), such that a steady flow velocity in the test section of the channel was able to be produced within the range from 0.03 m/s to 0.24 m/s.

The flow from the test section was collected into a recovery tank, from which it was returned to the pump through 0.30 m diameter piping, which was located underneath the

water channel. Fluid was discharged from the pump vertically upwards into the settling tank through a perforated pipe in an effort to maintain uniform discharge throughout the channel depth. An adjustable plunger capped this pipe at a level below the free surface of the tank, thus preventing a jet-type discharge and helping to reduce non-uniformity in the vertical velocity profile. The settling tank was 2.44 m wide, 1.52 m high and approximately 2.13 m long and contained five screens to condition the flow. The properties of these screens are provided in Table 2. The water went through a 9:1 contraction, having a 4.5:1 width ratio and a 2:1 height ratio. The contraction in the horizontal direction was plane-symmetric, whereas the contraction in the vertical direction only occurred on the bottom surface of the channel as the free surface was not interrupted from the settling tank to the test section. The walls of the settling tank were made of formed stainless steel sheets, which were supported by a steel frame.

The test section side walls and bottom were made of 9.5 mm thick glass, supported by a steel frame. The test section comprised three sections, joined by short, smooth-seamed plates made of acrylic material. The first and last sections were 1 m in length and the middle section was 2 m in length. All results reported here were collected in the first 1 m section, in which the velocity was fairly uniform across a large part of the cross-section.

Some experiments were better viewed with a white background. In these cases, a cardboard sheet covered with white paper was placed outside the test-section sidewall behind the most convenient viewing location. Other experiments required a black, non-reflective background. A black acrylic sheet with a matte finish was placed in contact with the interior of the channel vertical wall opposite the most convenient viewing side-wall. This provided

good contrast for a number of visualization techniques, provided a non-reflective surface to aid in image recording and enhanced laser radiation safety. Polyvinylchloride braces were made to keep this sheet against the wall as it had a tendency to bow out into the channel near the floor of the test section. The location of these braces is detailed in Figure 9. The support upstream of the experimental set-up was sunk into the channel floor to prevent it from disturbing the flow. The downstream support was of channel width, protruded 10 mm up into the channel and was placed 0.90 m downstream of the contraction and below the set-up, once more in an effort to prevent significant disturbance to the flow.

The water flowing at the end of the test section was collected in the recovery tank and was directed to two vertical perforated pipes, which had diameters of 0.30 m and led to the return pipe towards the pump. Adjustable plungers capped these vertical perforated pipes to prevent the entrainment of air into the piping system.

The channel was also fitted with a secondary water circuit providing chlorination and filtration. This secondary circuit drew water from an opening at the bottom of the recovery tank through a ball valve and into flexible tubing with a diameter of 38 mm. The secondary flow was produced by a radial pump (Grundfos UP-26-99BF) rated at 250 W (1/3 hp). This water was passed through a filter housing (Aqua Pure AP801) containing a filter with a maximum particle transmission size of 30 μm (Aqua Pure R-30-BB), then through a chlorinator (Olympic, Shakopee, Minnesota, USA) containing swimming pool grade chlorine pucks, which were replaced approximately on a two-week schedule. The pipe leaving the chlorinator had a diameter of 76 mm; it ran underneath the channel and discharged at the upstream end of the settling tank, approximately 1 m from the centreline of the channel. A

household electrical timer was used to operate the radial pump twice daily for 6 h at a time. To ensure that the flow was not disturbed during experimentation, the pump was kept off during these times.

It was discovered that the vertical velocity profile in the channel test section had a slight axial non-uniformity, with flow near the floor being approximately 10 mm/s faster than flow near the free surface when the average channel velocity was 90 mm/s. This difference was attributed to the fact that water was collected in the recovery tank mainly from its lower part (recall that plungers were lowered in the collection pipes to avoid air being trapped in the system by the sink-vortex mechanism). This was corrected quite effectively by placing a 0.33 m high plate of polyvinylchloride across the bottom of the test section immediately upstream of the recovery tank, about 3.5 m downstream of the main experimental location. This is shown in a schematic diagram for the flow set-up in Figure 10. An earlier attempt to correct this non-uniformity by using a similar plate that was only 0.21 m high reduced the velocity difference between the faster fluid near the bottom and the slower fluid on the free surface to approximately 2 mm/s. It was confirmed that the insertion of either plate did not introduce any unsteadiness or other disturbances in the flow near the experimental location. The turbulence intensity of the channel was less than 4.4% for flow velocities between 0.03 m/s and 0.06 m/s and less than 3% for flow velocities between 0.06 m/s and 0.24 m/s.

When the channel was left in a filled state overnight, the water level in the channel dropped by as much as 10 mm due to water leakage and evaporation. Considering that the flow velocity in the test section depended on the water level for a given pump motor

frequency, the water height in the test section was measured before each trial using a scale permanently affixed to the wall of the channel and was adjusted to 0.60 m, if required.

3.2 Pipe Location and Jet Supply System

A schematic diagram of the flow set-up is provided in Figure 10. A pipe was inserted vertically in the water, through its free surface, 0.6 m downstream of the contraction end. The pipe was oriented in this manner to avoid the presence of a large boundary layer at the base of the pipe, and also to avoid having to penetrate the glass bottom of the channel. A small boundary layer was present at the base of the pipe as an endplate was used as described later in this paragraph. The pipe was oriented in the vertical direction using a rod level (CST/Berger 06-750). The immersed pipe end was at a depth of 0.36 m, which was 0.24 m above the channel floor. An end plate was placed on each pipe at a depth of 0.02 m from the free surface to reduce interactions of the pipe wake and the free surface. The end plates were designed following suggestions by Cowdrey (1962), Szepessy and Bearman (1992), Szepessy (1993) and Dunn (2004). They were round plates constructed of clear, colourless glossy acrylic sheet. A 30° chamfer was machined all around the circumferences of the plates with the flat side of the plate facing the test section of the pipe. A sketch of a typical end plate and its position relative to the waterline is shown in Figure 11.

In order to establish well-defined exit conditions for the jet flow, it was decided to maintain a neutrally buoyant, steady, fully developed, laminar flow near the end of the pipe. To achieve neutral buoyancy with the surrounding cross-flow fluid, the fluid for the jet was drawn from the channel water, from a location that was 0.6 m downstream of the pipe near

the free surface at the sidewall and such that it did not interfere with the observations. Drawing the jet fluid from the channel also ensured that the water level of the channel did not vary during the experiments. This was not only for convenience, but also ensured that the channel velocity remained constant, as it was very sensitive to the water level.

This flow was then drawn through plastic tubing (I.P.L. Arianna T.A.) with an internal diameter of 13 mm and a length of 3 m to a radial flow pump (March Manufacturing 809HS, Glenview, Illinois, USA) rated at 30 W (1/25 hp), which was located below the test section of the channel to reduce the chance of cavitation. As shown in Figure 10, the water was pumped up to a height of 3 m above the free surface of the channel through a 5 m length of flexible tubing with a 25 mm inner diameter, into a head tank that was fitted with an overflow to ensure that a constant head was provided to the flow in the pipe. This arrangement was a substantial improvement over an earlier one, in which the pump was directly connected to the pipe, introducing some unsteadiness in the flow due to the passage of impeller blades, pump surging and electric power variation. The drain tube for the overflow of the head tank had a diameter of 10 mm. Its inflow entrained air from the free surface of the overflow tank, which caused the overflow water to be bubbly. To avoid any interference of the overflow fluid with the observations, the drain tube from the head tank discharged into the recovery tank of the water channel, as far downstream as possible from the experimental section.

The tubing for the pressure line from the head tank was inclined downward over its entire length such that any air that was possibly trapped in the line could escape back through the tubing to the free surface of the head tank. The pressure line from the head tank was led

back down to channel level to a Y-joint, where the main water flow was mixed with a flow of dyed water at proportions that depended on the experiment being performed. The flow rate of the mixture was controlled and measured by a jet-control rotameter, which ensured that, irrespectively of the proportion of dyed water, the flow rate of liquid forwarded towards the pipe was maintained at the desired value.

A home-made dye delivery system, driven by compressed air from the available supply of the building, was used to supply the various dyes to this experiment. The dyes, diluted in water, were contained in three separate canisters of radial water filters (Aqua Pure AP09T) from which the active filter cores were removed. Air at a gauge pressure of 48 kPa (7 psi), kept constant by a pressure regulator (Air Products E11-K-N515D) was connected to the "water in" connection (the outer portion) of the filter canister. This kept the air above the dye within the filter canister pressurized. A short length of tubing was connected to the interior side of the "water out" connection (the inner portion) and the other end of the tube was submerged below the surface of the dye. The exterior portion of the "water out" connection was then connected to a non-calibrated dye-control rotameter fitted with a needle valve such that the flow rate of the dye could be easily regulated and roughly monitored. The output of this dye-control rotameter was connected to the one leg of the Y-joint and water from the head tank mentioned previously was connected to the other leg. Thus, the concentrated dye was mixed with water and delivered to the experimental pipe through a calibrated jet-control rotameter controlling the flow rate.

The needle valve on the calibrated jet-control rotameter provided means of regulating the jet flow rate and hence the jet velocity. From the jet-control rotameter, the flow was led

directly to the pipe using flexible tubing with a variety of sizes to step the inner diameter up from the interface with the jet-control rotameter to the pipe connection. The variety of sizes also assisted in further mixing the water and diluted dye within the tubing. Close to the entrance of the pipe, a second Y-joint was inserted in the water/dye mix supply tube to assist in removing air that was possibly trapped in the system during filling or while changing the test pipe.

The jet-control rotameter was designed for nitrogen gas and hence required calibration to be used for the measurement of the flow rate of water. Calibration was done by setting the rotameter at a specific flow rate and recording the volume of water that exited the rotameter over a given time. This process was repeated ten times per rotameter setting – five times each on two different days – and the different volumetric flow rates were averaged. The rotameter contained two different "floats" to cover a relatively wide range of flow rates. Accordingly, two calibration curves were created, each fitted to the measurements for each indicator. Both sets of data were fitted well by straight lines. The uncertainty on these measurements was found to be at most 2.2% for flow rates higher than 2 mL/s and at most 6.4% for lower flow rates. The calibration results are shown in Figure 12.

3.3 Pipe Design

As mentioned in Chapter 2, Eiff and Keffer (1999) discovered that the structure of the flow depends on the ratio of the inner to outer diameter of the pipe. For this reason, and in order to maintain geometric similarity, the diameter ratios of all pipes were set to the same

value. To conform to the previous research by Johnson et al. (2001), the diameter ratio of 0.89 was used throughout all experiments. This value is also equal to the diameter ratio of Schedule 40 pipe with a nominal diameter of 4 inches, which is often used in oil-field flares.

A number of different designs were used for the test pipes before finalizing the choices. During a preliminary stage, a clear, colourless, acrylic pipe with a diameter of 13 mm was used to permit the development of effective dye injection techniques. For these tests, a solution of methyl violet dye was introduced immediately downstream of the water supply line for the pipe. This provided effective visualization of the basic overall structure of the flow, but also showed problems that needed to be addressed. The vortical structures were difficult to distinguish because of their small size; this suggested that the use of a larger pipe was necessary. Moreover, the acrylic pipe was found to bend due to the drag from the flow, which also suggested the need for larger diameter pipes as well as a stiffer wall material. Finally, the dye injection system used in these preliminary tests was found to produce inconsistent quality of flow visualization, which suggested the implementation of the dye mixing technique mentioned in the previous section. Another type of preliminary pipe design was non-electrically conductive pipes, which would permit the use of the electrolytic precipitate flow visualization technique (to be described in the following section). For these experiments, a polyvinylchloride pipe was used with an outer diameter of 21.7 mm and a diameter ratio of 0.88.

An initial set of four pipes of different sizes were machined from seamed stainless steel tubing stock. The sizes of these were 18.6 mm, 25.2 mm, 37.1 mm and 50.6 mm and, because of size limitations of the available lathe, they were all made to a length of 0.75 m.

This length was not sufficient for the flow to be fully developed at the pipe exit as discussed in the following paragraph. Consequently, these pipes were only used to explore scaling of the flow in a qualitative sense.

The test pipes used in the main experiments were all made of seamless stainless steel. Pipes with three different outer diameters, equal to 14.9, 21.5 and 38.1 mm were used to permit scaling of the flow. For uniformity of the jet starting conditions, it was desirable to have fully developed flows at the exits of all pipes, which required all pipes to be of sufficient length to ensure this condition. The entrance length L_e for laminar flow in a round pipe is given by $L_e/D = 0.06 \cdot \mathrm{Re}_d$, where d is the inner diameter of the pipe and Re_d is the Reynolds number based on the inner diameter (Munson et al., 2002). Expressing the Reynolds number in terms of volume flow rate Q instead of velocity, one may calculate the entrance length as

$$L_e = 0.06 \cdot \frac{4Q}{\pi \nu} \tag{11}$$

where ν is the kinematic viscosity of the water. Note that the pipe diameter does not enter explicitly in this expression for the entrance length. At the flow rate of 15 mL/s (which is the maximum possible flow rate in the system) and a somewhat higher than typical water temperature of 22°C, the entrance length was found to be 1.23 m. It was decided to make all pipes of equal length of 1.5 m to ensure that the internal flow was fully developed at the pipe exit. Nevertheless, due to a mix-up in the machine shop that was responsible for the machining of the pipes, the pipe with an external diameter of 38 mm was only 1.25 m in length. This is not a concern as this value is still larger than the estimated entrance length.

The dimensions of the three pipes used in the main tests are shown in Table 3. Note that all pipes had diameter ratios that were within 3% of the desired value of 0.89.

3.4 Flow Visualization Techniques

A note of explanation is necessary concerning orientation of the flow images. In previous studies of elevated jets in cross flows as well as in most applications of interest, the jet issued from the top of the pipe. In contrast, the present arrangement is such that the pipe discharged fluid from its lower end. For ease in comparison with results from the literature, all images have been inverted vertically and the associated discussion refers to the flow orientation as if the free surface were interchanged with the channel bottom. Because in all experiments the jet was neutrally buoyant, jet exit orientation would have no effect on the flow structure. In all present discussion, the terms "above" and "below" are used in conformity with the inverted images. Moreover, in all images presented, the flow direction is from left to right.

During the preliminary stages of the experiments, a variety of flow visualization techniques were used to provide an overall view of the flow structure. At first attempt, the entire jet fluid was coloured with methyl violet 2B (a purple, water-soluble dye) and the cross-flow was marked with a small stream of congo red (a red, water-soluble dye) released from an injection tube with a diameter of 1.67 mm. A typical image recorded using this arrangement is shown in Figure 13. The presence of the dye released upstream of the pipe did not add much information to the images, and so it was discontinued to avoid any unnecessary flow disturbance. To provide contrast and to give a sense of orientation, a white

background with a light green grid was placed outside the glass channel wall farthest from the viewing area. Achieving the correct lighting to best view and record the flow patterns was difficult. First, two 100 W standard household incandescent light bulbs with large parabolic reflectors were positioned under the channel, but it was found that these did not provide sufficient light. A 500 W, gently focused halogen utility lamp was placed facing towards the channel through the viewing side wall in addition to the two 100 W lamps and this seemed to provide sufficient lighting to properly view and record the structures. This lighting arrangement is sketched in Figure 14.

The electrolytic precipitation method using lead foil was also used to visualize the flow. The submerged outer diameter pipe was covered with 0.13 mm thick lead-foil tape, which was connected to the positive terminal (anode) of a DC power supply. The negative terminal (cathode) of the power supply was connected to a carbon rod which was submerged downstream of the intake tube for the jet fluid. As long as the pH of the water was nearly neutral (above approximately 7), the wire connecting the voltage source to the lead foil was above the surface of the water, the surface of the lead foil tape was free of scale, and the voltage was kept sufficiently high (above approximately 60 V), lead oxide particles were released from the foil and formed a colloidal suspension that was visible in the water. Once the cross-flow velocity exceeded 50 mm/s, the particles were less easily detected, even though at 60 mm/s, the particles remained sufficiently visible. The size of these particles was estimated to be of the order of 1 μm (Dunn and Tavoularis, 2006). In consideration of the small particle diameter and the higher viscosity of water, the particles were able to track the flow dynamics to a frequency many orders of magnitude higher than the analyzed frequencies (Tavoularis, 2005). The carbon rod was kept sufficiently downstream of the pipe

such that the hydrogen bubbles released on its surface did not interfere with the flow around the pipe. An example of an image obtained using this method can be seen in Figure 15. A black background provided good contrast for recording images of the white lead oxide particles. To best capture still and motion pictures of this visualization, it was found that a more focused light from below worked best. A Buhl Optical 750 W projector lamp was directed at two standard vanity mirrors placed beneath the channel and the light was reflected upwards, illuminating the particles released from the foil. The use of the two mirrors enabled an increase in the intensity of light as they could both direct light through the same space.

The methyl violet dye was also used simultaneously with the electrolytic precipitation visualization technique. This allowed one to distinguish the fluid that originated from the jet from the cross-flow fluid which passed through the boundary layer on the surface of the pipe. Varying the relative contrast of the two visualization techniques and observing them independently offered good qualitative information about the flow patterns. An example of this can be seen in Figure 16. Nevertheless, getting proper lighting for this technique was rather difficult to achieve. As can be observed in Figure 16, because of the orientation of the light source, the areas of concentrated dye added purple shadows to the white lead precipitate particles behind them. Observation of the flow using sequences of video images allowed for a better differentiation between purple shadows and coherent structures.

One problem with the water soluble dye was that it diffused quickly in the non-coloured stream. In certain areas of the flow, especially on the lee side of the pipe, strong

turbulent mixing took place, which enhanced the dye diffusion and resulted in a seemingly shapeless purple cloud where no structures were discernable.

A different dye used was dibromofluorescein, which is a fluorescent dye. Fluorescence is the ability of a molecule to emit a photon with a delay of the order of 10^{-10} to 10^{-5} s after absorbing one. The emitted light is randomly polarized and usually has a wavelength that is different from the incident light wavelength (Tavoularis, 2005). Dibromofluorescein has a peak absorption wavelength of 495 nm and a peak emission wavelength of 517 nm (ISS Inc., 2007). Moreover, as it was a suspension rather than a solution, it allowed the flow structures to be discernable for a much longer period of time than conventional dyes.

To excite the dye, a few different light sources were used. Firstly, the light from a 750 W projector lamp was directed upward through the bottom of the channel, which provided sufficient light to cause the dye to fluoresce. This offered a three-dimensional view of the flow, suitable for observing the overall shape of the various structures. Another light source used was an Ar-ion laser, which has an emission peak containing approximately 20% of its total power at 488 nm (OPTIKON Corp., 1996), which is sufficiently close to the excitation wavelength of dibromofluorescein. This allowed the use of a laser-light sheet from the Ar-ion laser to illuminate a two-dimensional plane of the flow. A beam splitter (Oz Optics ULBS-12P-3.5-125-SP-488-50/50-40-33-3-1, Ottawa, Ontario, Canada) was placed in the laser beam path close to the laser output. The splitter directed a portion (approximately half of the power) of the incident laser-light into a fibre optic cable and the remaining light carried on its undisturbed path. The fibre optic cable (Oz Optics QSMJ-33-488-3.5/125-3-

10, Ottawa, Ontario, Canada) was 10 m long and led the light to a Powell lens (Oz Optics, Ottawa, Ontario, Canada) which spread the light into a sheet with the thickness of approximately 2 mm and essentially uniform intensity. The maximum rated power for the fibre optic cable was 1 W; however this was never attained because the laser power was never set above 1 W and only a portion of it was being directed into the cable.

When the location and the global structure of a vortex were both known, the laser-light sheet allowed the observation of only a cross-section of the structure without the dye in the foreground or background obscuring the view. An example of this is shown in Figure 17. The disadvantage of this approach was that, because the light sheet was relatively thin, this technique did not consistently yield very useful results. Whenever the structure under observation wandered or possessed sufficient three-dimensionality, it could not be easily observed in a plane. The combination of the laser-light sheet and the 750 W projector lamp provided simultaneously a three-dimensional global view as well as a planar view. An example of such an image is shown in Figure 18.

Flow images were recorded using both a still camera and a video camera. The still pictures were recorded with a digital single-lens reflex camera (Nikon D70) with a standard lens (AF-S Nikkor, f= 18 to 70 mm, 1:3.5 to 4.5, G ED, Aspherical, 67 mm diameter). The challenge with most of the still pictures was to have sufficient lighting of the subject. The best images were obtained by maximizing the lighting using the techniques described previously and reducing the exposure time of the image to 1/10 s and the f-stop of the lens to F/4.5. This technique produced fairly dark images, which were brightened by post-processing using an automated image enhancing function found in Jasc Paint Shop Pro 8

software. This command within this image processing software package automatically adjusted the brightness, contrast and colour saturation of the image to quickly yield near optimal levels for these properties. This technique allowed the fastest possible shutter speed to be used to capture a sharp image while still offering visible results.

Motion pictures were captured using a digital video camera (Sony Digital Handycam DCR-VX1000) with a fixed lens (f = 5.9 to 59 mm, 1:1.6, 52 mm diameter). The camera was used at its maximum frame capture rate of 30 frames per second. The shutter speed for each frame was set to 1/60 s and the f-stop was set to F/1.6. This offered sufficiently sharp images with ample light to permit observation of flow features in detail. For these images, no image enhancement was deemed to be necessary.

When the flow was visualized using the fluorescent dye alone, it was desirable to prevent any light other than that at the fluorescent wavelength of the dibromofluorescein from entering the recording apparatus. Unwanted light appeared in the images in the form of reflections, glare and ambient light at various wavelengths. For this reason, a narrow-band interference filter was occasionally used in front of the camera lens whilst capturing images. The filter was a CVI Laser F10-520.0-4-M67 optical interference filter with a peak transmission wavelength at 520 nm, which corresponded to the peak emission wavelength of the dibromofluorescein. The transmission profile of the filter is shown in Figure 19. Note that the peak transmission is at 45% of the incident light power. The full-width half maximum (FWHM) for the filter was 10 nm. The peak of the Ar-ion laser at 514.5 nm was narrowly outside the half-maximum of the transmission profile of the filter, which means that the incident light from the laser was only partially attenuated before entering the camera.

3.5 Flow Measurement Techniques

Early estimates of the Strouhal number of the vortical structures were based on frequencies measured by observation of motion pictures. A marker was affixed to the screen that was showing the output of a motion picture and the number of frames between consecutive structures were tabulated and averaged. As the frame rate was held constant at 30 frames per second, the average frequency for the structure passage could be determined. Difficulties with this technique arose when the process of structure generation was irregular as well as when the quality of the video images was not sufficient to allow the identification of distinct structures. When structures were generated at an essentially constant frequency, the uncertainty of the measured frequency was calculated to be less than 13%. With variable structure frequencies, the uncertainty became significantly larger, averaging around 50%, and in some cases as high as 90%. As this was only a preliminary method, used only to estimate very roughly the range of Strouhal number, this was deemed to be tolerable. Uncertainty values were calculated according to the method set out in the text by Tavoularis (2005): the uncertainties of individual properties was estimated as twice the standard deviation of a set of repeat measurements and error propagation procedures were used to estimate the uncertainties of dependent properties.

A laser Doppler velocimetry (LDV) system by Dantec Dynamics Inc. (Skovlunde, Denmark) with a BSA F50 60N20 processor was used for measuring local flow velocity. The laser used was an argon-ion laser (Lexel Laser 95L-5, Fremont, California, USA) and the light was transmitted to the LDV components through fibre optic cables, which were rated for a maximum power of 1 W. The light sheet employed for the flow visualization

techniques used the same laser; however, it was never used simultaneously with the LDV system. The splitter block mentioned in section 3.4 was removed for LDV measurements such that the full power of the laser was available to the LDV system. The laser was aimed into a transmitter (Dantec 60X41), which split the beam into two parts: the first part was aimed into a Bragg cell, which shifted the light frequency by 40 MHz, and the second part passed through without frequency shift. Each part of these two beams was then separated into two others, each having a different wavelength: a 488 nm beam and a 514.5 nm beam. The four beams (488 nm unshifted, 488 nm shifted, 514.5 nm unshifted and 514.5 nm shifted) were transmitted through separate fibre optic cables, which were bundled together in a single 10 m long fibre optic cable that led to the LDV head. A beam expander (Dantec 55X12) was used along with a lens with a focal length of 310 mm to produce a sufficiently small measurement volume at the beam intersection, while also maintaining the measurement volume sufficiently away from the LDV head to allow measurements far enough into the water channel. Each time a particle passed through the measurement volume, it generated a burst of light, whose frequency was directly proportional to the particle velocity. Frequency shifting of one beam permitted the discrimination of velocity components in one direction from those in the opposite direction. With all beams intersecting in air, the LDV measurement volume in air would have been approximately an ellipsoid 649 μm long, 77 μm high and 78 μm thick with its thickness in the streamwise direction. Due to the refraction of the laser entering the water, the measurement volume length expanded to 865 μm and had little change in its other dimensions. Bursts of light scattered by particles passing through the measurement volume were collected in backscatter mode. Using backscatter mode simplified the experimental set-up, as the transmitting and

collecting lens coincided, thus eliminating the need for alignment of two sets of optical components after each traverse. The light from the bursts was transmitted back through a single fibre optic cable connecting to the LDV head, through the distribution box and through another fibre optic cable leading to another colour separator. This colour separator was connected to two photomultiplier tubes (PMTs), one for each wavelength. These PMTs were connected to the Dantec processor which provided appropriate high-voltage power to the PMTs and also forwarded the information to a personal computer for further processing. Additional information on the operation principles of LDV systems has been provided by Tavoularis (2005).

The water in the channel contained naturally introduced solid particles with sufficient concentration and size distribution to provide adequate LDV signals. Particles larger than approximately 30 μm were removed as water passed through the filter fitted in the filtration system of the channel.

A full listing of the settings used in the LDV system is given in Appendix B; only the pertinent ones are listed here. The Ar-ion laser beam contained 43% of its total power at 514.5 nm and only 20% of it at 488 nm. Consequently, the signal from the 514.5 nm beams contained many more detectable bursts than the signal from the 488 nm beams. Careful alignment of the entire system ensured that the amount of light lost in transmission in and out of the various fibre optic cables was as low as possible. This ensured good data rates for both velocity components. To ensure a maximum possible data rate, the LDV measurements were run in a non-coincident fashion, such that each component was measured independently of the other. Often, only information from a single component of the LDV was used;

therefore there was no advantage to couple the two components with coincident readings. The high voltage sent to the photomultiplier tubes was also increased to 1600 V, rather than using the default value of 1000 V. This increased the signal strength received from the tubes, but still kept the current coming from the PMTs below the recommended maximum of 1500 μA to avoid tube damage.

A particle image velocimetry (PIV) system by LaVision GmbH (Goettingen, Germany) was used to measure the velocity and vorticity fields in the flow. The laser used was a Neodymium: YAG dual cavity pulsed laser (New Wave Research Solo PIV 120XT, Fremont, California, USA), in which two lasers were contained, sharing the same optical components as in typical PIV arrangements. Each laser was capable producing pulses with an energy up to 120 mJ per pulse at a wavelength of 532 nm. One of the two available cylindrical lenses with focal lengths of -10 mm and -20 mm was used to fan the laser beams out into a laser sheet (LaVision 1108405). The resulting light intensity of the sheet was not uniform, but this was not of concern as PIV measurements are not sensitive to light intensity variation.

A digital camera capable of storing two successive images on a photodiode array of 2112 x 2072 pixels per frame (LaVision Imager Pro X 4M) was set-up with its lens axis oriented as normal to the plane of the laser sheet. The camera was fitted with a Nikon 50 mm focal length, F/1.8 lens, but a variety of other interchangeable lenses were also available. The camera was controlled by a camera controller and was synchronized with the laser through a programmable timing unit (LaVision 1108058). Background light noise was reduced by placing an interference filter on the camera tuned to the 532 nm wavelength of

the laser (LaVision 1108501) and also by switching off the room lights during testing. Limited by the maximum capability of the on-board memory of the camera (512 Mb), a maximum of 35 pairs of images could be acquired at a maximum frame rate of 7.284 Hz, therefore spanning 4.805 s. In the present study, no pre-processing was performed on the images produced by the PIV measurements. The processing of the images was performed differently depending on the flow case.

The seeding used was the same as that used for the LDV testing. A calibration tool was created to aid in the accurate calibration of the PIV system for each case. A ruler scale was placed perpendicular to the pipe axis, pointing downstream as shown in Figure 20. This allowed the measurement of the spanwise location of the laser sheet and the positioning of the laser sheet in relation to the pipe, as well as providing a length scale for the PIV images. During testing, the calibration device was removed from the pipe and it was confirmed that the camera was focussed on the plane of the laser sheet.

Table 2 – Information about flow conditioning screens present in water channel (Dunn, 2004)

Screen	Material	Hole Shape	Hole Size	Screen Thickness	Solidity
1	natural fibre sheet	N/A	N/A	75 mm	N/A
2	stainless steel	circular	2.3 mm	0.79 mm	0.63
3	natural fibre sheet	N/A	N/A	75 mm	N/A
4	aluminum	circular	4.8 mm	1.60 mm	0.42
5	nylon	square	1.6 mm	0.25 mm	0.4

Table 3 – Dimensions of pipes used in the main tests of the present study

Outer Diameter (mm)	Inner Diameter (mm)	Pipe Length (mm)	Diameter Ratio
14.9	13.0	1500	0.87
21.5	19.4	1500	0.90
38.1	33.7	1250	0.89

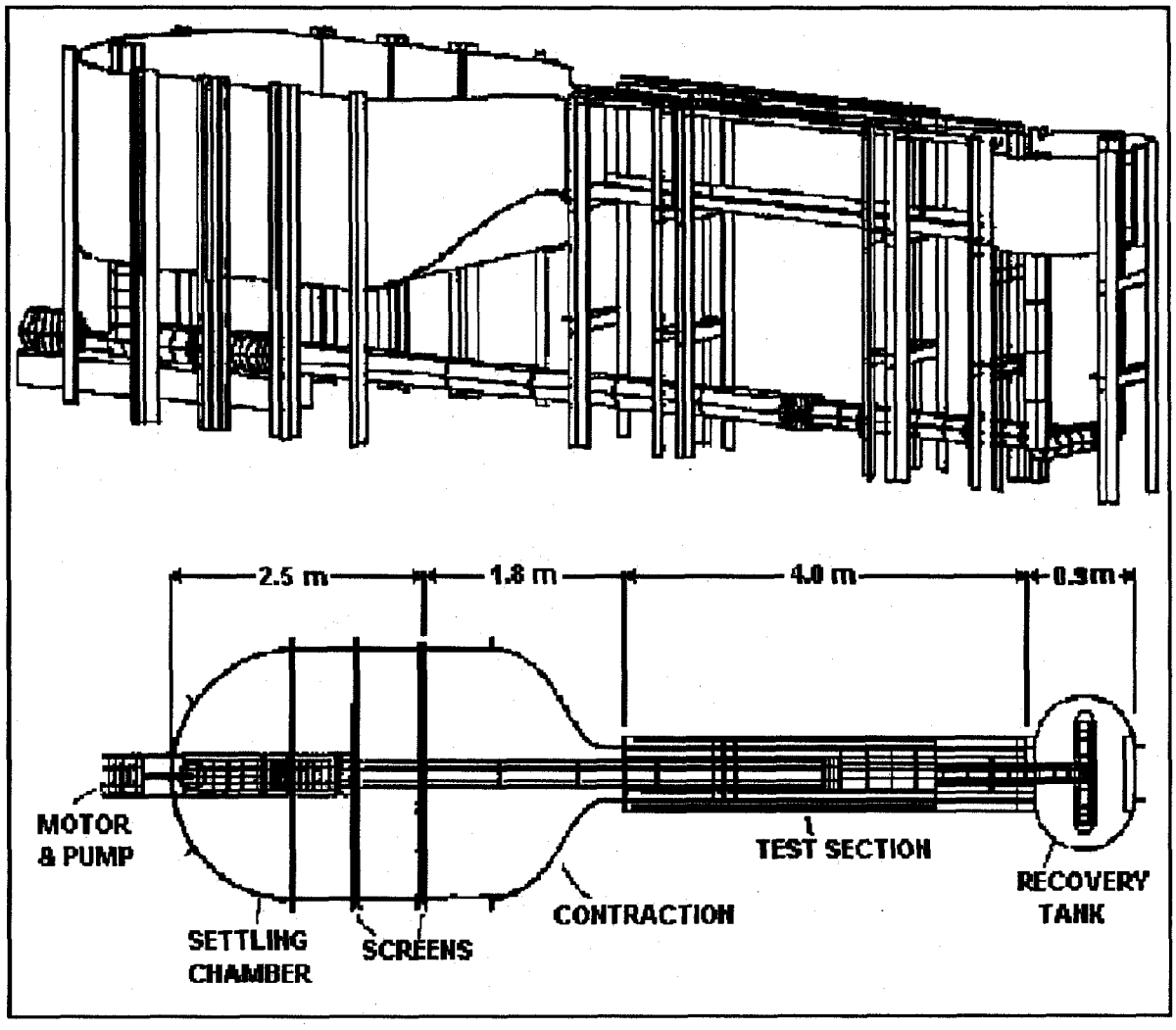

Figure 8 – Illustration of recirculating water channel (Dunn, 2004)

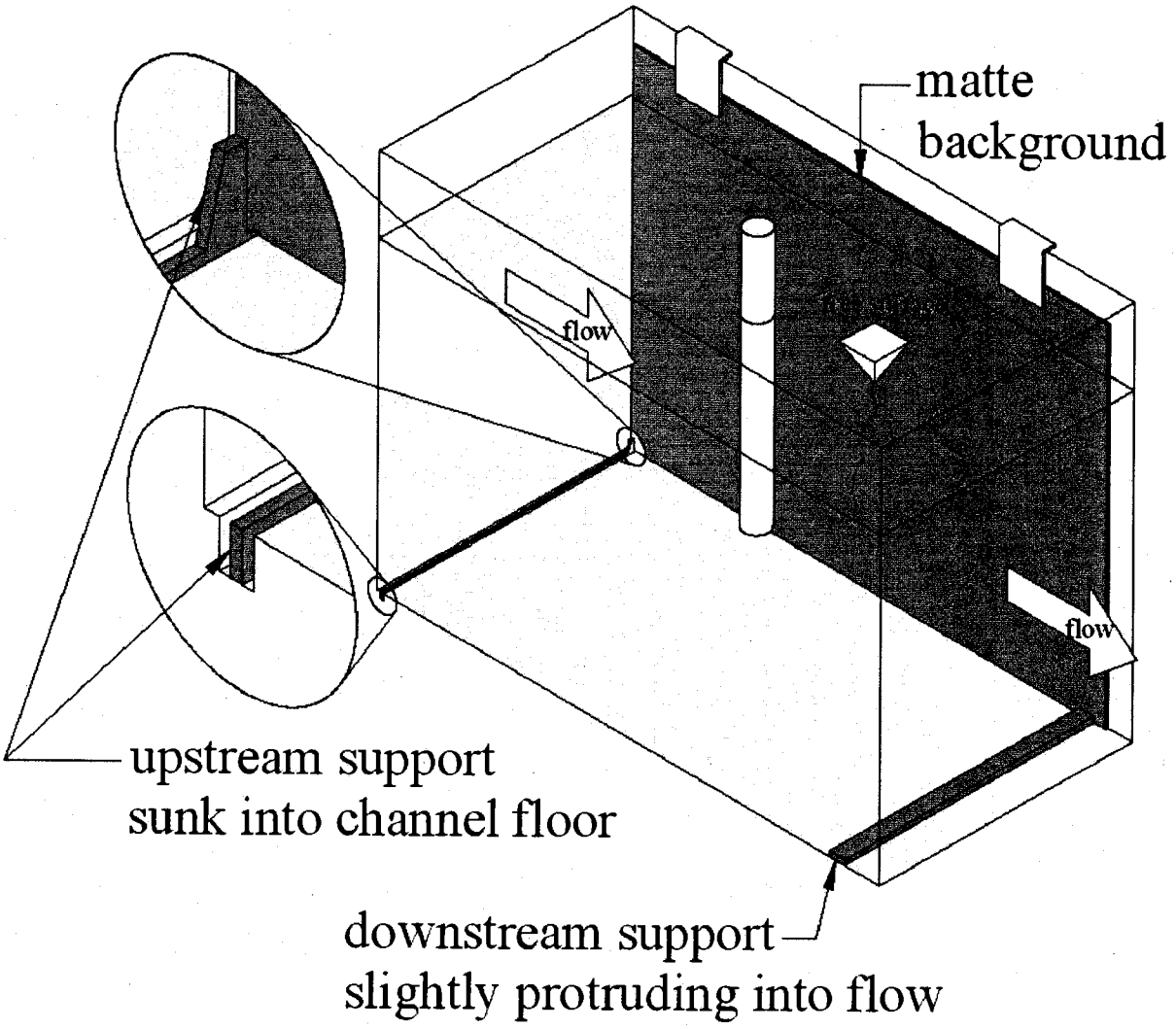

Figure 9 – Detail of supports for matte optical background

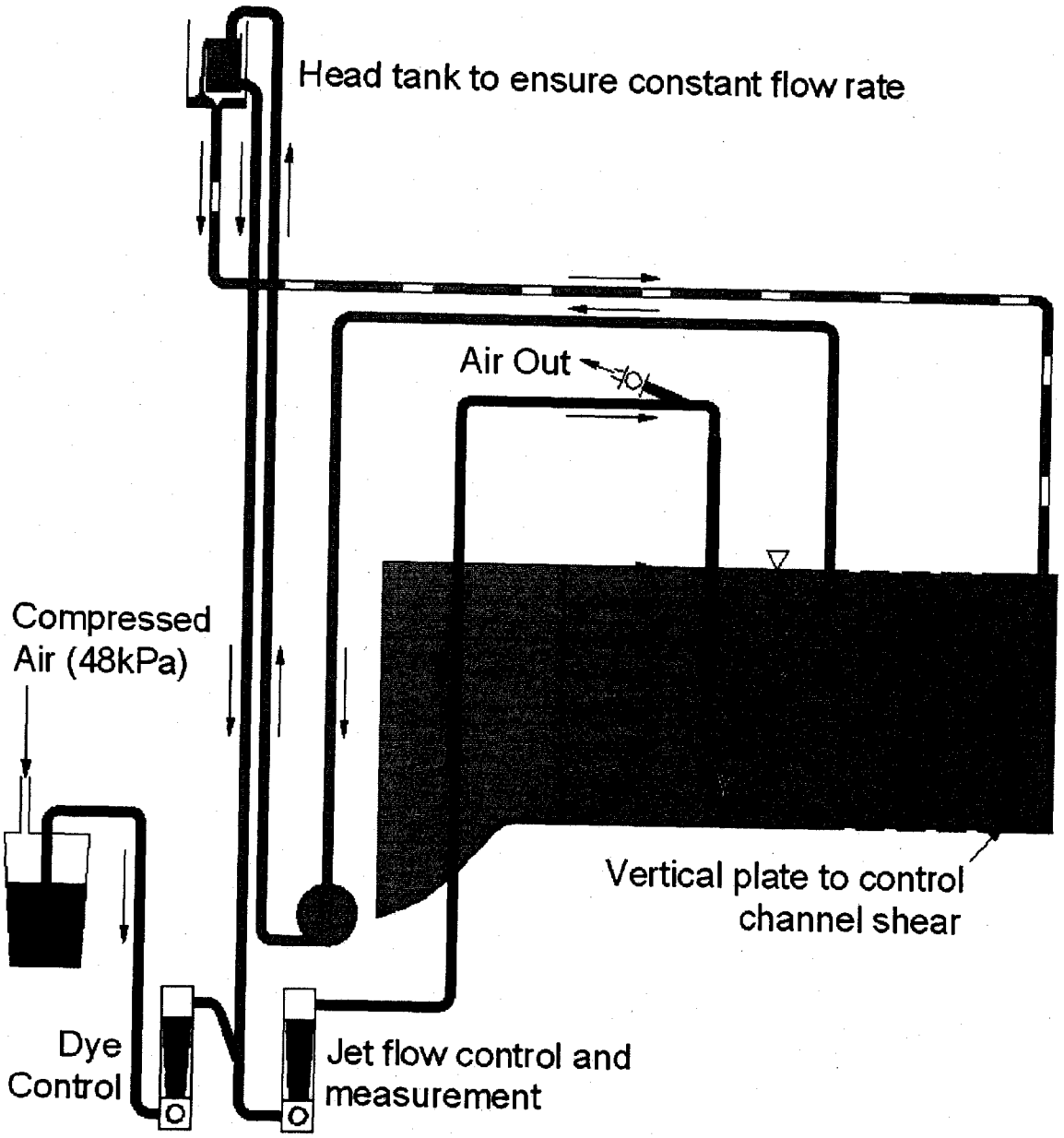

Figure 10 – Schematic diagram of flow system

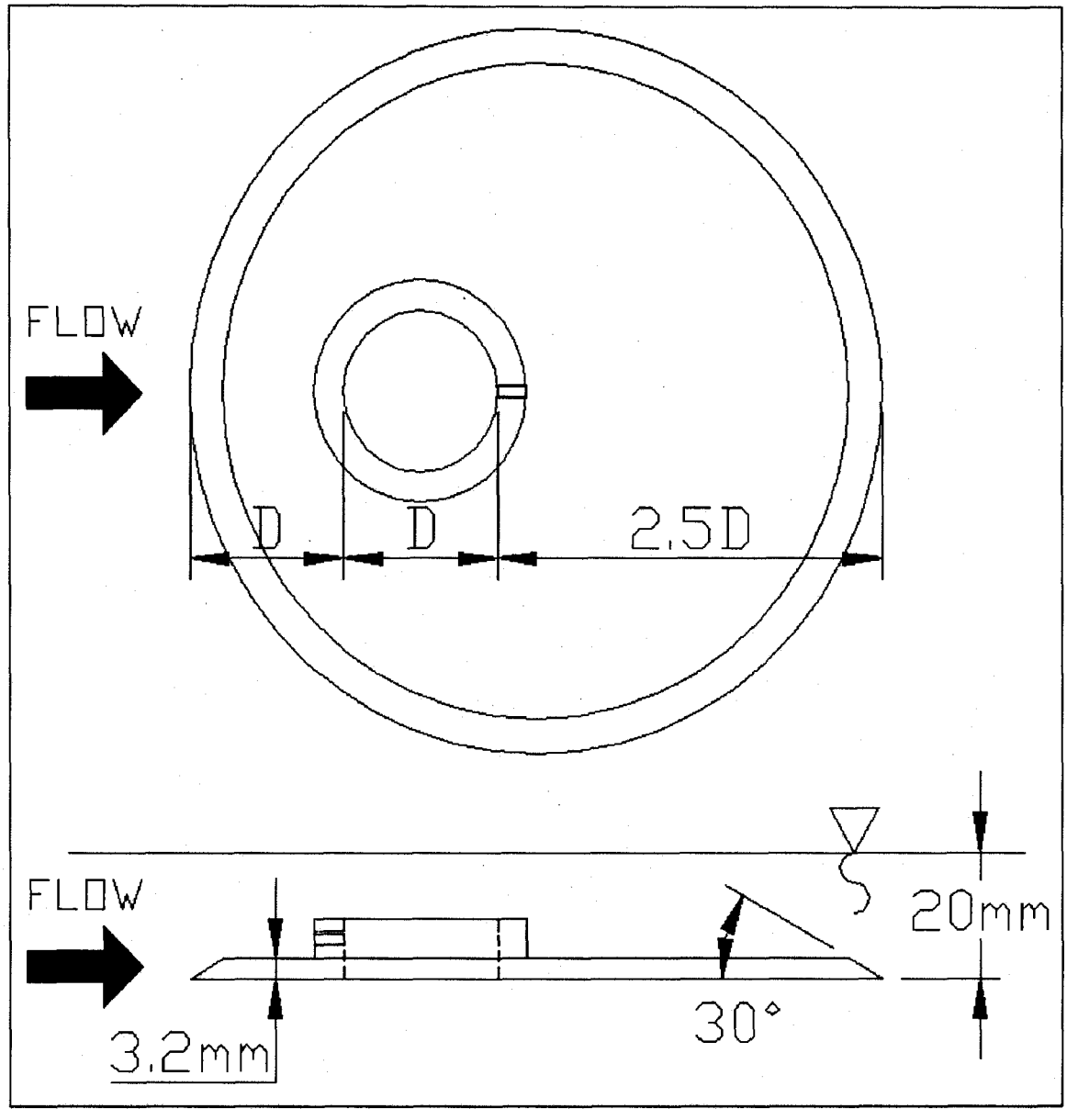

Figure 11 – Sketch of a typical endplate

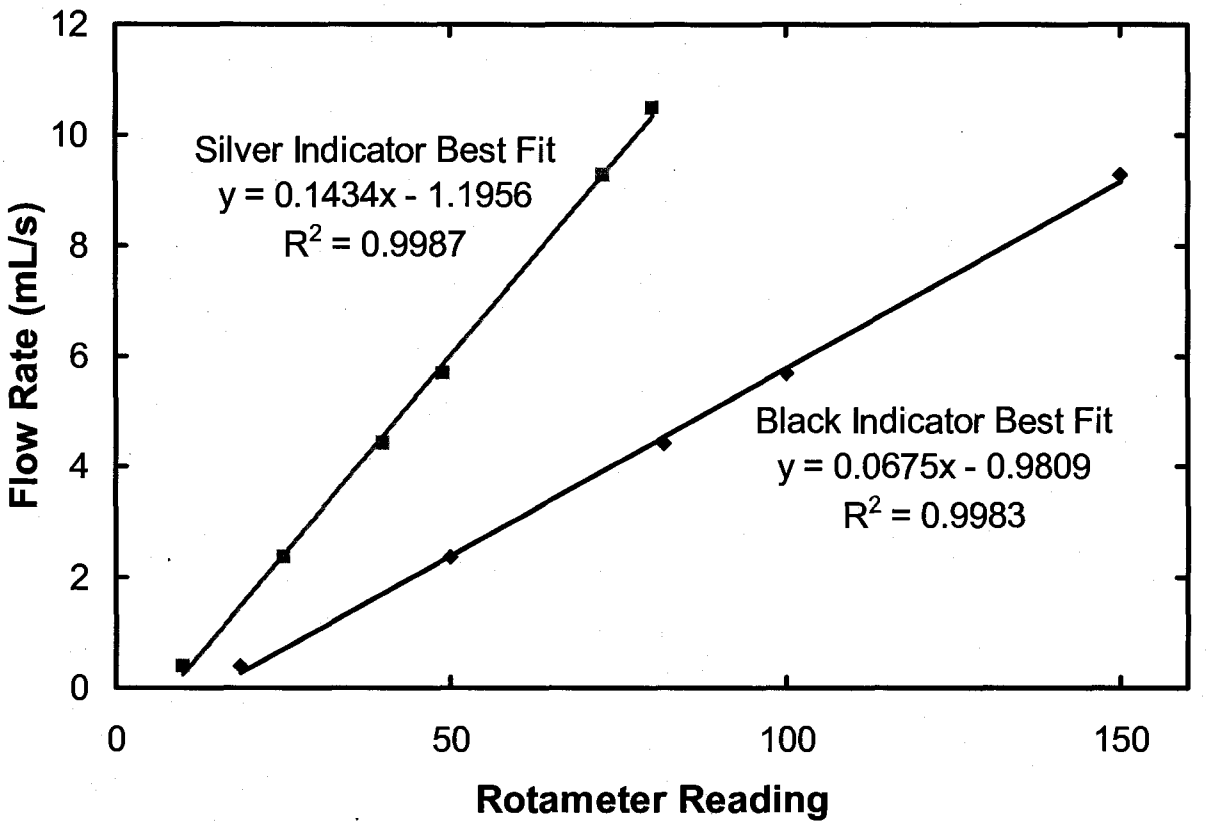

Figure 12 – Rotameter calibration results

Figure 13 – Flow visualization using methyl violet in the jet and congo red in the cross-flow (d = 18.79 mm, R = 0.076, Re_j = 327, Re_∞ = 1330)

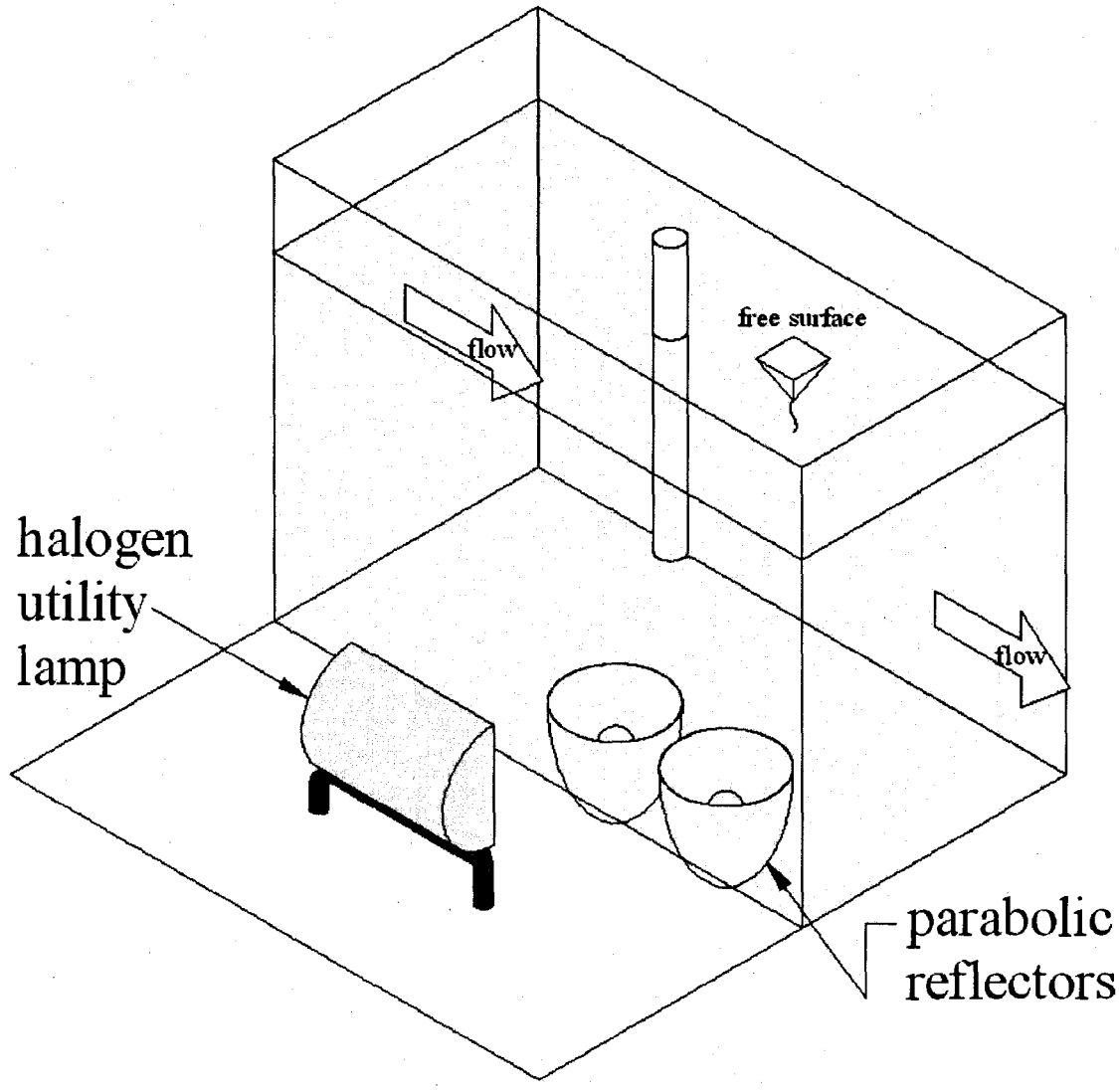

Figure 14 – Lighting arrangement detail for flow visualization using methyl violet dye

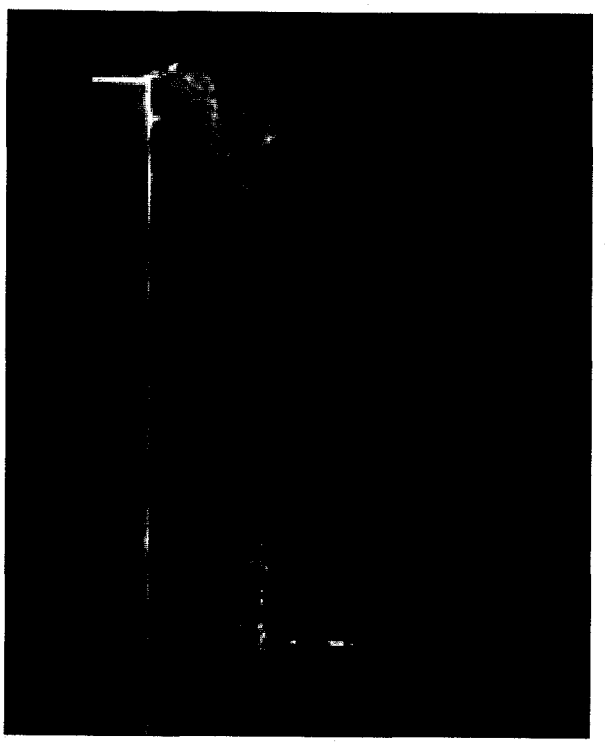

Figure 15 – Example image of flow visualization using electrolytic precipitation (d = 18.79 mm, R = 0.076, Re_j = 327, Re_∞ = 1330)

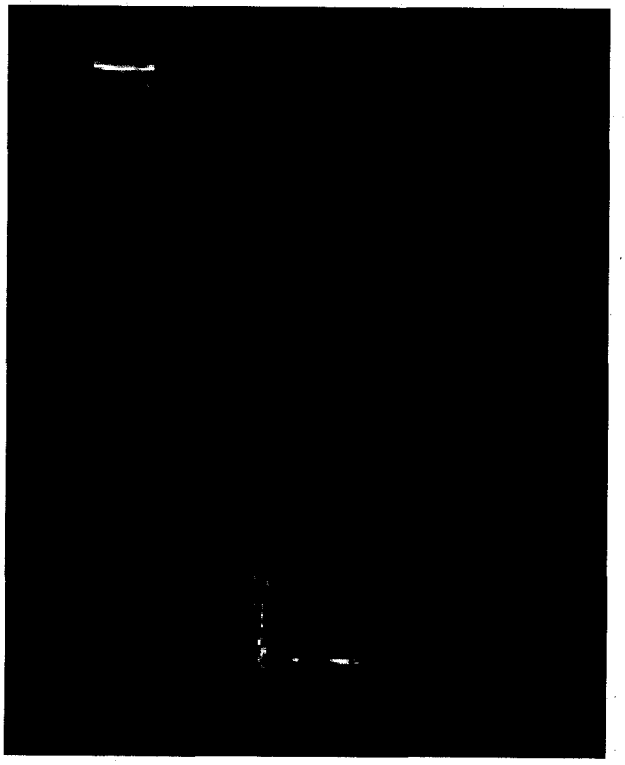

Figure 16 – Example image of simultaneous lead precipitation and dye injection (d = 18.79 mm, R = 0.076, Re_j = 327, Re_∞ = 1330)

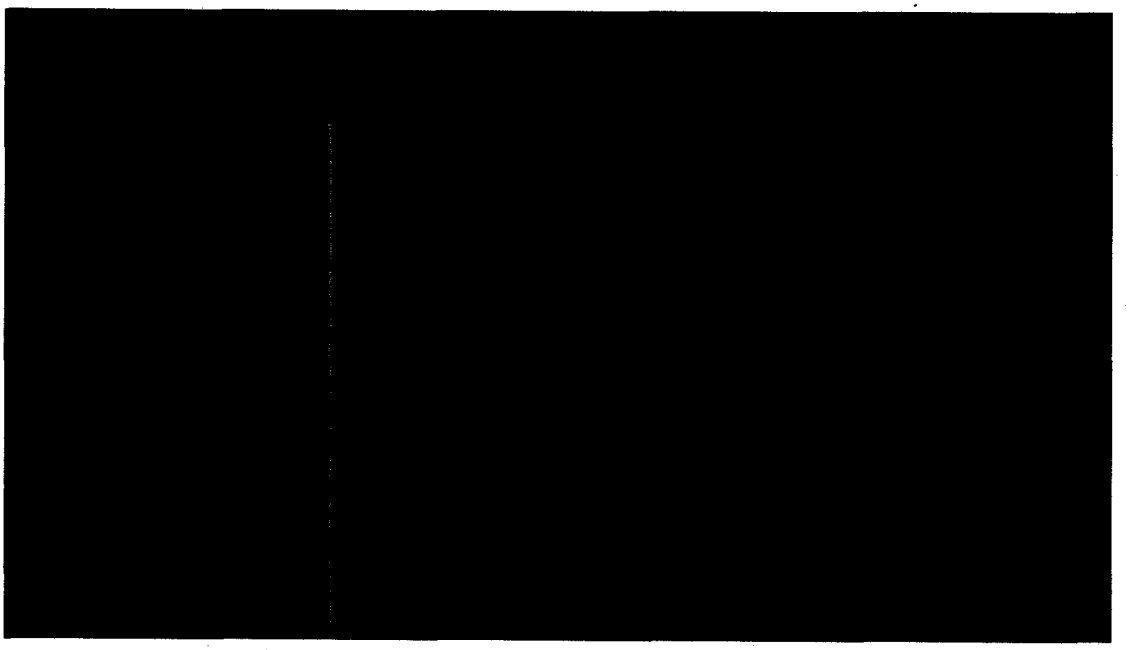

Figure 17 – Example image of fluorescent dye excited by a laser sheet (d = 18.79 mm, R = 0.076, Re_j = 327, Re_∞ = 1330)

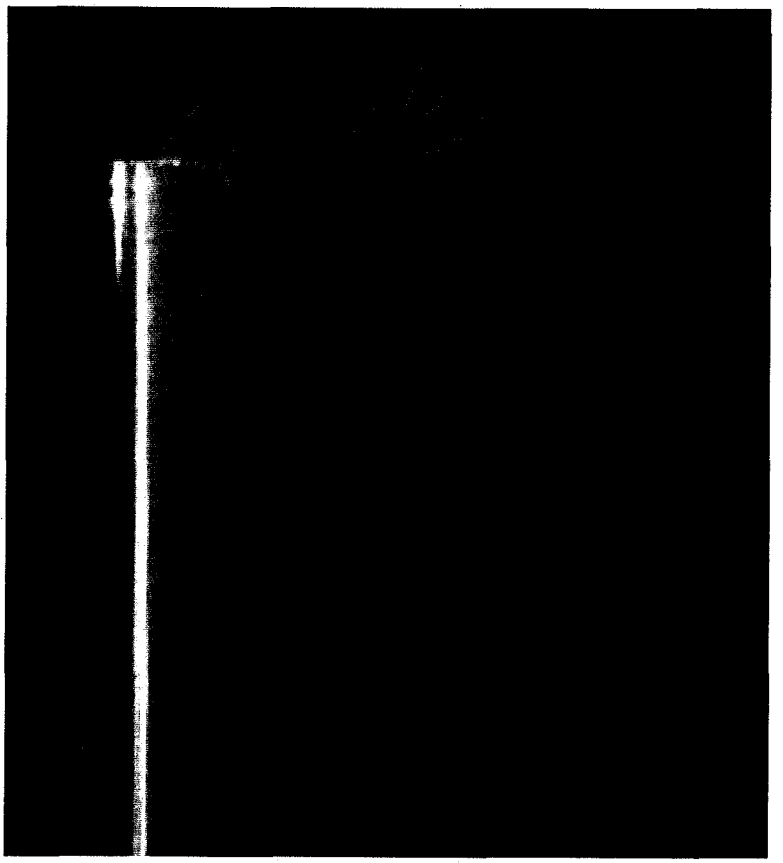

Figure 18 – Example image of visualization using fluorescent dye with simultaneous flood light and laser sheet (d = 45.27 mm, R = 0.0082, Re_j = 259, Re_∞ = 3204)

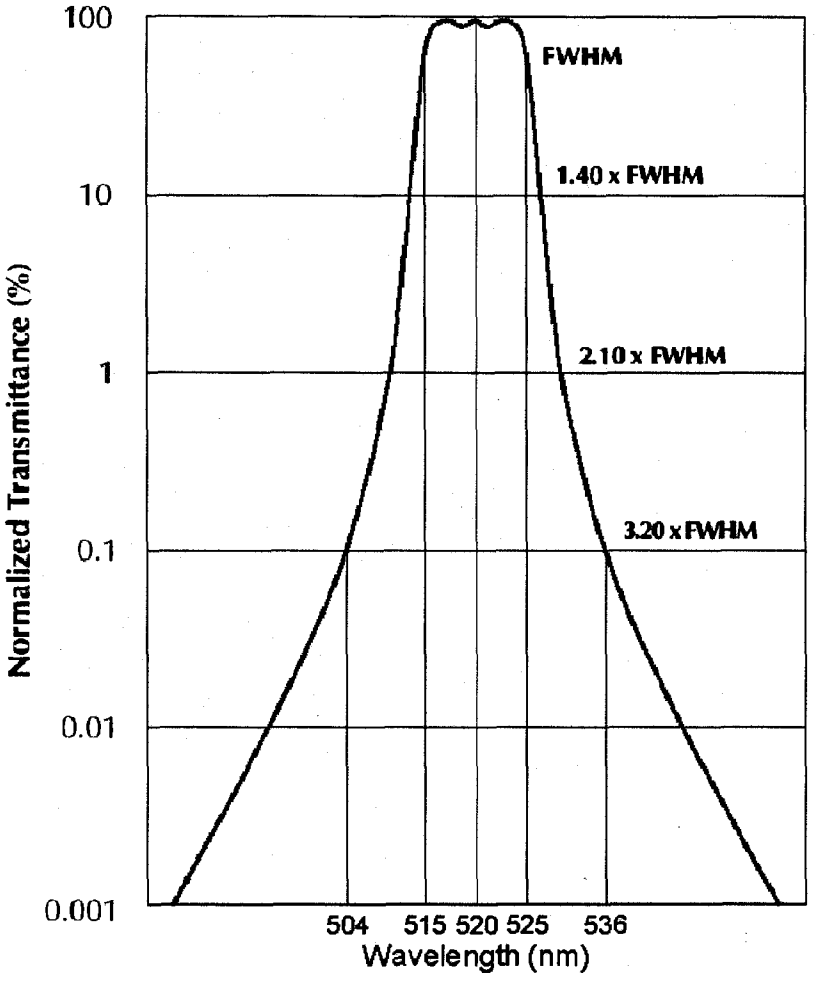

Figure 19 – Narrow-band interference filter transmission profile (peak transmission = 45%) (CVI Laser Optics LLC., 2007)

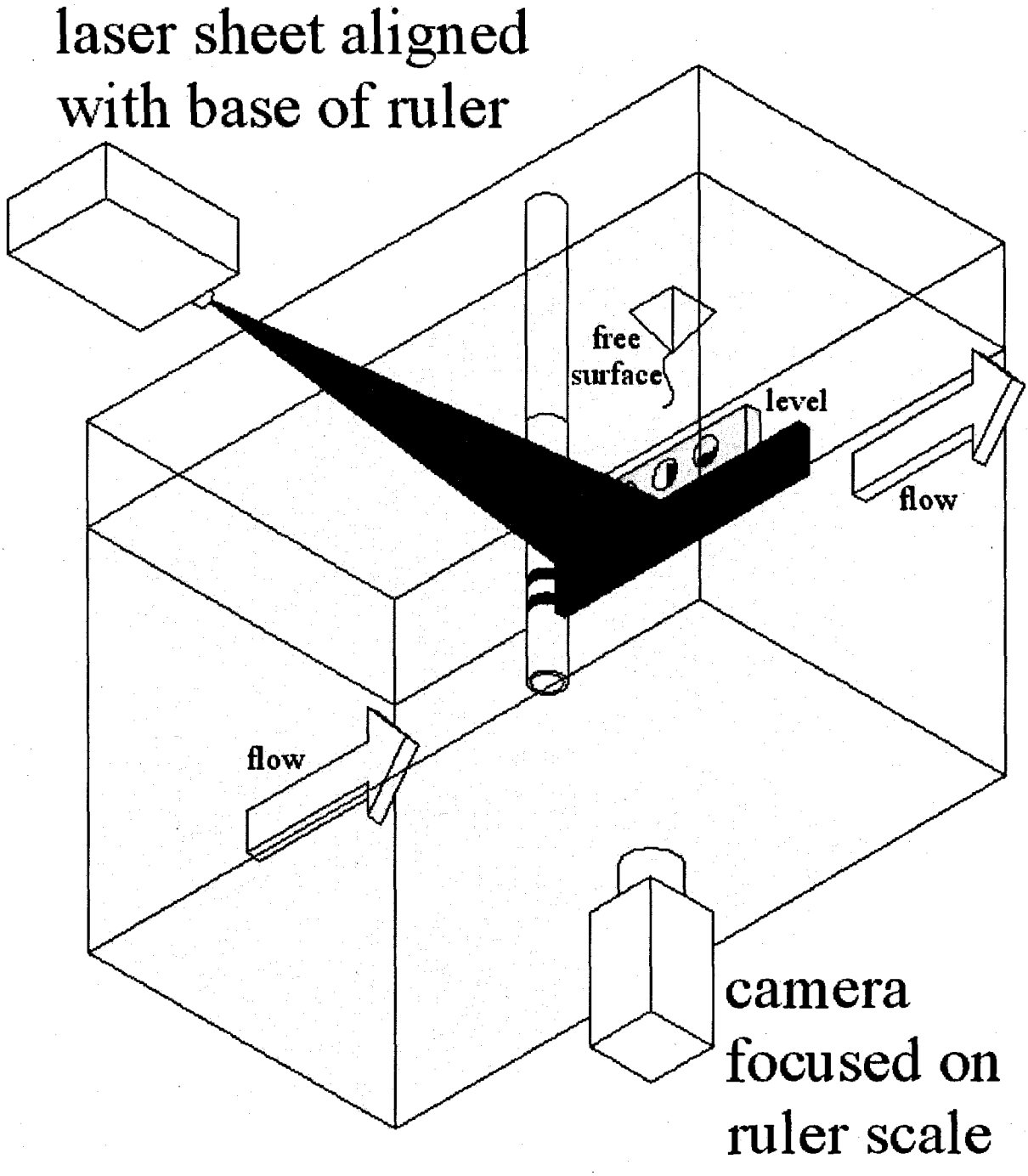

Figure 20 – Detail of PIV calibration procedure

Chapter 4 Preliminary Measurements

4.1 Water Channel Flow Quality

LDV measurements were used to determine the relationship between the frequency of the drive motor for the channel main pump and the nominal velocity in the test section of the channel. At a channel height of 0.60 m, 39 measurements were taken at the locations specified in Table 4, in which the origin of the y-axis coincides with the location of the pipe tip when the pipe was introduced in the flow. The downstream location of the plane of measurements in the unobstructed flow coincided with the location at which the axis of the pipe was to be located. Measurements were taken for 20 different values of the motor frequency, such that one measurement was taken per motor frequency in the ascending direction and another in the descending direction and allowing 300 s (5 minutes) for the channel flow to settle between measurements. The results are shown in Figure 21. Linear least squares fitting to the measurements gave the following relationship between the motor frequency f and the test section speed q_∞ with a coefficient of determination $r^2 = 0.9998$

$$q_\infty = 0.0063 f + 0.0006. \tag{12}$$

It has been observed that the channel could operate in a stable fashion in the range of motor frequencies between 5 and 40 Hz, which corresponds to test section velocities between 0.03

and 0.24 m/s.

The degree of uniformity of the velocity profile of the channel test section was measured using the LDV system. Measurements were taken every 15 mm at a location just downstream of the contraction end and along a vertical line on the centre plane of the channel from the lowest to the highest point at which the LDV measurement volume could be inserted in the channel. The lowest measurement point was limited by the silicone sealant between the glass wall of the channel and the steel frame, and the highest measurement point was limited by the free surface. By comparison to the pair of LDV beams that were located on a horizontal plane, the pair of beams on the vertical plane introduced more strict limits on the test section volume that was reachable by the LDV system. Though only the horizontal beams were used for these measurements, it was ensured that all beams could reach the measurement volume to maintain experimental consistency.

4.2 Velocity Profile at the Exit of the Pipe

The LDV was used to measure the velocity profile at the pipe exit. By integrating this velocity, it was possible to check the accuracy of the jet-flow rotameter calibration. Moreover, the shape of the velocity profile was observed to confirm that the flow was laminar and fully developed at the exit of the pipe. The measurements were taken by moving the LDV measurement volume along the x-axis on a plane that was 0.17 diameters (6 mm) away from the pipe exit plane. Movement in this axis also moved the LDV head toward and away from the refraction interfaces between the air, glass and water. In turn, the distances

moved by the LDV head and the measurement volume were different. The optical distortion due to diffraction was corrected for using the analysis shown in Appendix A. The flow rate calculated from the measured velocity profile had a 1.5% difference from the value indicated by the rotameter. The velocity profile, shown in Figure 22, was indistinguishable from the Poiseuille velocity profile with the exception of values near the edges.

4.3 Velocity in the Channel Surrounding the Pipe

For each test case, two vertical traverses were made with the LDV measurement volume located 0.20 m upstream of the axis of each pipe and 3 diameters downstream of the axis of each pipe, respectively. The measurements were made every 15 mm away from the pipe tip and at a tighter spacing near the tip, as detailed in Table 4. Both the upstream and downstream traverses were first done with the jet off, then with the jet on at the appropriate flow rate. These initial measurements provided a base line measurement to obtain the actual channel bulk velocity such that it was not necessary to rely solely upon the motor frequency calibration curve. Moving the downstream measurement location slightly away from the centreline enabled better recording of the vortex shedding from the pipe and traverses were offset from the centreline in the spanwise direction by 0.39 d. The upstream measurements were taken at the same spanwise location for consistency. LDV signals were recorded for 60 s at each position. A typical example of such results can be found in Figure 23.

A number of LDV measurements were taken with the measurement volume located on the vertical centreplane of the channel ($x/D = 0$) and near the average position of the

interface between the jet and the cross-flow. An illustration of typical flow measurement locations is shown in Figure 24. Such measurements were taken at the upstream edge of the jet at its exit point ($z/D = -0.5$), at the mid-point of the pipe ($z/D = 0$) and at the downstream edge of the pipe ($z/D = 0.5$). In most cases, additional measurements were taken at selected positions below the stack tip and at the level of the tendril structures, which are further described below.

To find the location of the interface between the jet fluid and the cross-flow fluid, dibromofluorescein was injected in the jet fluid and it was excited with the 750 W projector lamp as described in the previous Chapter. The LDV measurement volume was placed near the tips of the observed vortices, where velocity differences from the cross-flow would take relatively large values. The Ar-ion laser beams used by the LDV system excited the dye in their paths and generated fluorescent emissions at a wavelength of approximately 517 nm. This emission did not significantly interfere with the photomultiplier tube operation.

To complement the velocity measurements in the shear-layer, the flow appearance was recorded using the video camera simultaneously with the LDV signal recording. The optical interference filter was placed in front of the camera in order to prevent the fluorescent light emitted by dye along the LDV beams from saturating the video images. The frequency of the structures was determined by timing their passage on the video. Unfortunately, this frame counting technique was not successful for all videos. Typically, the videos taken at the upstream tip of the pipe did not show sufficient variation for any potential structures, should they be present, to be identified. In some cases, the frequency of the structures was close to or exceeded the frame rate of the camera, in which case this method could not be

used. The frequency measurement uncertainty varied from case to case, but they were combined with an analytical technique explained below in section 4.4.

4.4 Frequency Determination Techniques

To determine the Strouhal number for different types of vortices, different techniques were used. In some cases, both flow visualization videos and simultaneous LDV measurements were available, whereas in others only videos were at hand. For those cases without LDV measurements, the technique described previously in section 4.3 was used: the frequency of vortex generation was computed by counting the number of frames between the passage of consecutive vortices through a point fixed on the video screen. This frequency was used to estimate very roughly the Strouhal number, but because of its relatively large uncertainty, it was not used for quantitative comparisons.

For those cases for which both LDV measurements and videos were simultaneously taken, frequencies were estimated using two different techniques: the first technique was similar to that just mentioned with the difference that, instead of an arbitrary point on the screen, the location of the LDV measurement volume was used as the fixed point; the second technique provided the frequency from spectral peaks of the LDV signal.

One is reminded that LDV signals are discrete, with each value corresponding to a light burst created by the passing of a particle through the measurement volume. Consequently, the sampling rate is not uniform. To enable the implementation of a Fourier transform, the acquired LDV time history was resampled at a constant rate using a custom-

written MATLAB program, which was a modified version from one composed by Dunn (2004). The average sampling rate of data acquisition was calculated for each measurement point and the fixed rate at which the data were to be resampled was set to this average rate. To acquire "signal" values at evenly spaced time points, the "sample and hold" technique was used. Each resampled value was set to be equal to the value of the original time history acquired immediately before the specific resampling time. The resampled time histories were high-pass filtered using a fourth-order Butterworth filter, comprising two second-order filters, one of which was applied in the forward direction and the other one in the backward direction, such as to ensure zero phase shift of all data. The cutoff frequency used was 0.1 Hz to correspond to the known long-wave motion of the water channel. The mean of the signal was then subtracted from the resampled and filtered signal as the interest in this analysis was only to determine the frequency. Finally, fast Fourier transforms (FFT) of records of 2^{14} (= 16 384) points each were computed. The FFT magnitude, computed by multiplying each value by its complex conjugate, is proportional to the frequency spectrum of the streamwise velocity. Spectra were plotted versus frequency as well as, in non-dimensional form, versus the Strouhal number. An example of a spectrum versus Strouhal number is shown in Figure 25. As only the frequencies and the relative magnitudes of the peaks within one plot were of concern, the spectral axis was not labelled.

The values of frequency computed from the spectral peaks were compared with the results from the video-review study. Results of both types were not available for all methods. As previously mentioned, the video method did not yield results when the frequency of the passing vortices approached the recording frame rate of 30Hz. Moreover,

measurements could not be taken when the LDV measurement volume, which was used as the fixed point for vortex counting, was in the boundary region between different types of vortices, so that different mechanisms were interfering with counting vortices of a particular type. Finally, in some cases, adjacent vortices were too small to be distinguished from each other on the video. With the LDV measurements, difficulties arose when the vortex frequency was low enough for its peak location to be indistinguishable from low frequency fluctuations of the channel speed, when the velocity differences between the passing vortex and the free stream were not sufficiently high to register passing vortices, or when vortices wandered sideways such that not every vortex crossed the measurement volume.

Each video was reviewed and classified in one of three categories, depending on the location of the measurement volume: it was said to be either a good representation of one type of vortex, a good representation of another type of vortex or of no quantitative value.

Once the values for the Strouhal number were computed for the various cases, comparisons between the values obtained from the LDV signals and the videos were made. In the majority of cases, the difference between the two results was less than 4%. In a few cases, however, such differences were higher if one considered the frequency of the highest spectral peak. The spectra obtained in such cases had an additional peak that was only slightly lower than the highest peak and this secondary peak matched within 4% the frequency estimated from the video. In these cases, the results from the video-review study were used.

4.5 Experimental Conditions

To explore the appearance of the flow structure at various momentum-flux ratios, an initial set of tests were performed where the cross-flow velocity was kept constant at 61 mm/s while the jet velocity and pipe size were varied independently. The set of four 0.75 m long pipes (sizes 18.6 mm, 25.2 mm, 37.1 mm and 50.6 mm) were each placed in the channel and the jet flow rate was varied from 0.7 mL/s to 13.0 mL/s in steps of approximately 0.7 mL/s. Due to the variation of pipe diameters, this caused the jet velocity to vary from approximately 1 mm/s to 60 mm/s, giving a momentum-flux ratio range from 0.0002 to 0.99. Fluorescent dye was injected into the jet flow and flood lighting was used as well as the two-dimensional laser sheet aligned with the y-z plane. After 120 s of settling time between each case, a 60 s video was taken of the flow.

From the results of the above trials, three momentum-flux ratios were chosen (approximately 0.0009, 0.01 and 0.2) for further exploration. The principle test pipes described in Chapter 3 were used. For each of the three momentum-flux ratio values, three cross-flow Reynolds numbers were chosen that were equally spaced and spanned the operable range of the equipment. For the highest momentum-flux ratio of 0.2, the equipment was not able to supply the desired Reynolds number, and therefore, lower Reynolds numbers were used. The final values used for testing are shown in Table 5.

Table 4 – Values for y-coordinates for LDV measurements

Pos#	y(mm)	Pos#	y(mm)	Pos#	y(mm)	Pos#	y(mm)	Pos#	y(mm)
1	165	10	30	19	-2	28	-90	37	-225
2	150	11	15	20	-3	29	-105	38	-240
3	135	12	10	21	-4	30	-120	39	-255
4	120	13	7.5	22	-10	31	-135	40	-270
5	105	14	5	23	-15	32	-150	41	-285
6	90	15	2	24	-30	33	-165	42	-300
7	75	16	1	25	-45	34	-180	43	-315
8	60	17	0	26	-60	35	-195		
9	45	18	-1	27	-75	36	-210		

Table 5 – Flow conditions for measurements made in the final stage of testing

	D (mm)	R	Re_j	Re_x		
Low R	14.94	0.00146	70	2124	Med Re_∞	
	14.94	0.00097	100	3722	High Re_∞	
	21.54	0.00091	42	1533	Low Re_∞	Re_∞ higher than desired due to calibration error
	21.54	0.00087	72	2717	Med Re_∞	
	21.54	0.00081	99	3896	High Re_∞	
Medium R	14.94	0.0083	40	505	Low Re_∞	
	14.94	0.0091	176	2124	Med Re_∞	
	14.94	0.0079	287	3731	High Re_∞	
	21.54	0.0076	40	506	Low Re_∞	
	21.54	0.0077	174	2197	Med Re_∞	
	21.54	0.0072	297	3892	High Re_∞	
High R	14.94	0.24	218	510	Low Re_∞	
	14.94	0.22	387	948	Med Re_∞	
	14.94	0.21	554	1397	High Re_∞	
	21.54	0.20	206	510	Low Re_∞	Re_∞ lower than desired due to equipment limitations
	21.54	0.21	382	928	Med Re_∞	
	21.54	0.21	546	1324	High Re_∞	

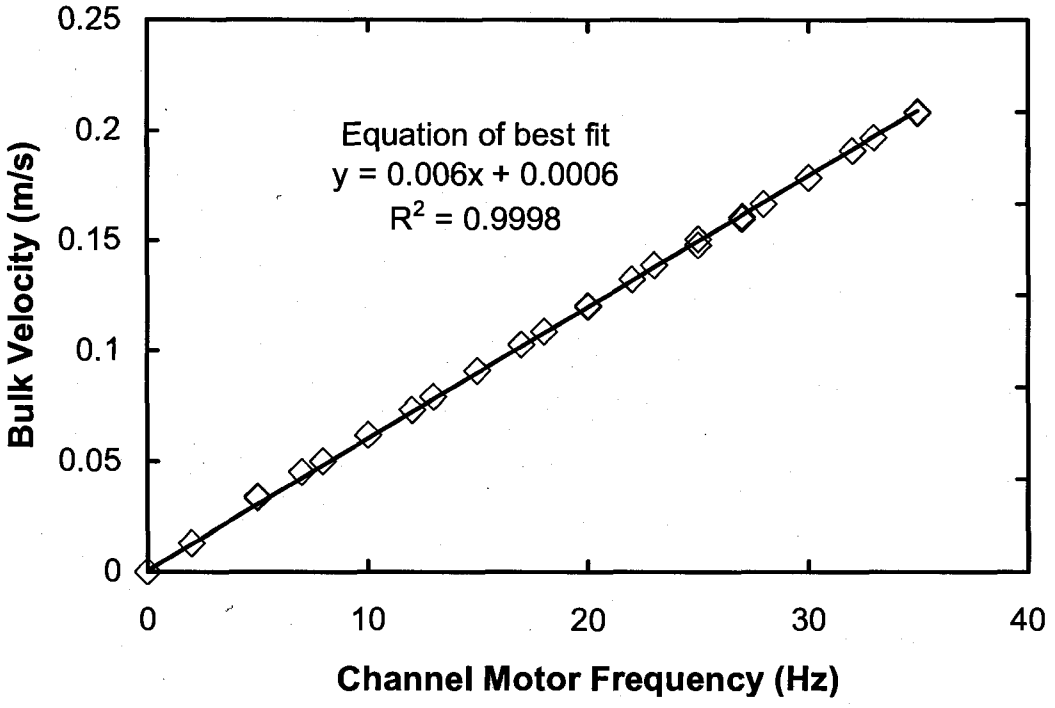

Figure 21 – Channel velocity relationship with motor frequency at a water height of 0.60 m

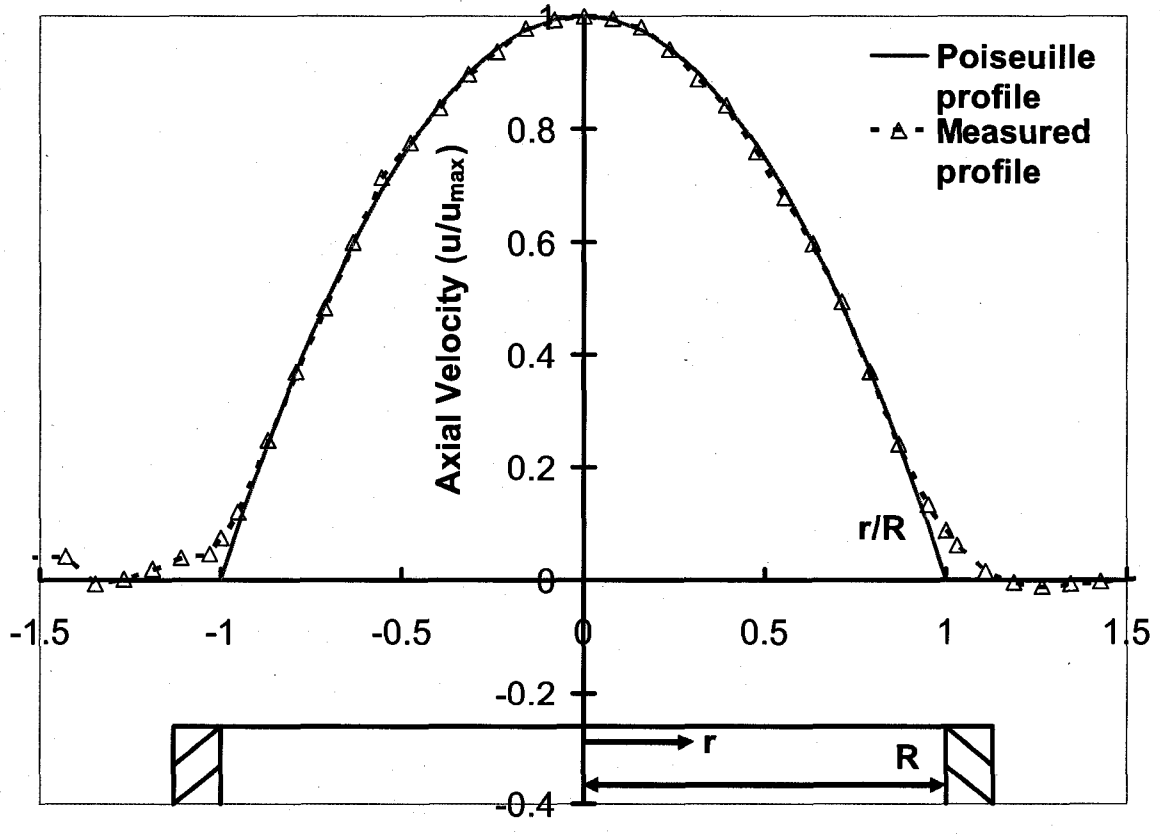

Figure 22 – Jet velocity profile (d = 33.73 mm, Re_j = 518, Re_∞ = 0)

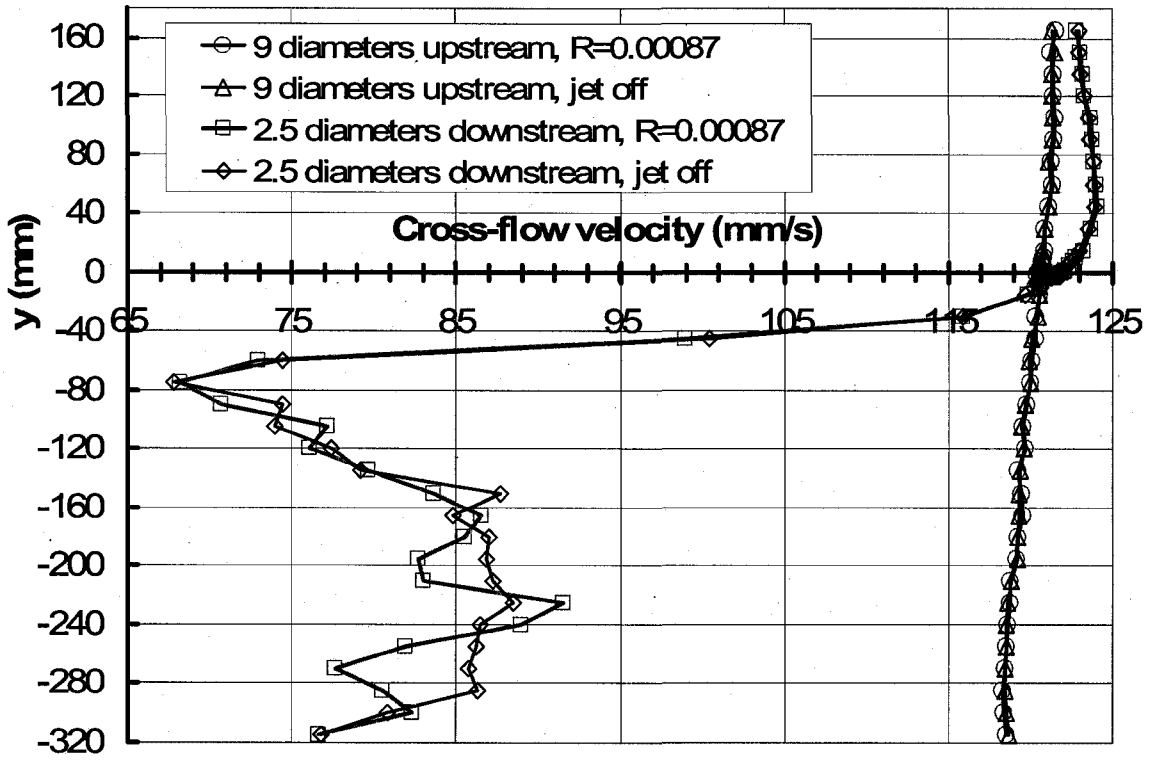

Figure 23 – Profiles of the cross-flow velocity at $Re_\infty = 2717$

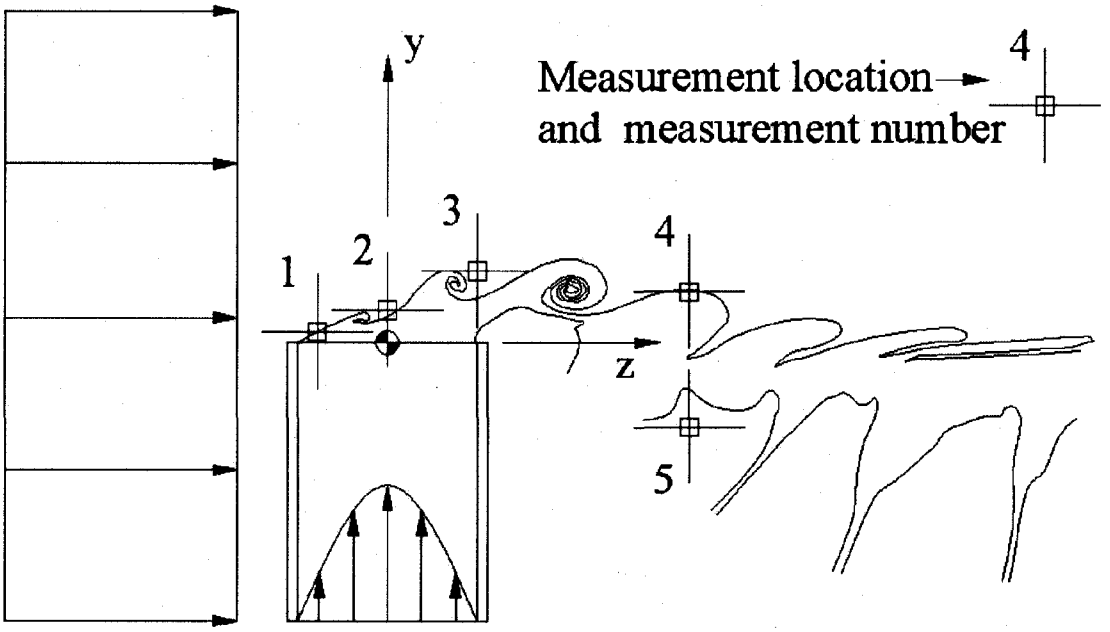

Figure 24 – Typical supplemental measurement locations

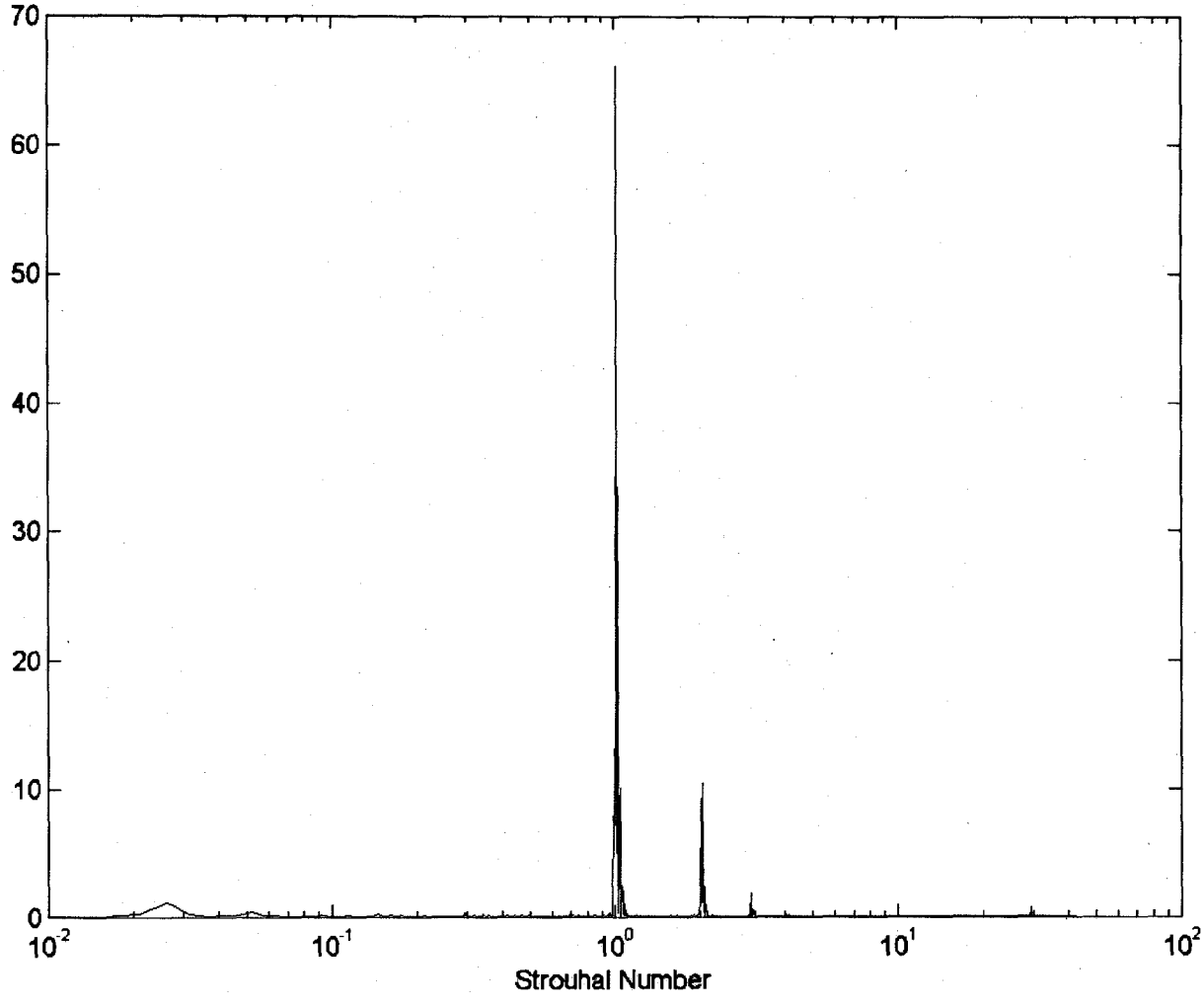

Figure 25 – Example of spectral plot (in arbitrary units) versus Strouhal number (d = 14.94 mm, R = 0.22, Re_j = 387, Re_∞ = 952)

Chapter 5 Overview of Flow Structure

As previously mentioned, extensive qualitative experiments were conducted during the early stages of this research, whose goal was to gain insight into the various types of coherent large-scale structures appearing in the flow field of the elevated jet in a cross-flow. To allow comparison of the results using different flow visualization techniques, all flow conditions were kept constant during this exploration phase such that the structures would have the same form in different trials. Unless otherwise specified, a pipe with an inner diameter of 18.79 mm and flows with a momentum-flux ratio of 0.076 and a cross-flow Reynolds number of 1330, giving a jet Reynolds number of 327, were used.

The following four types of coherent structures, identified in Figure 26 for a typical set of experimental conditions, were of interest in the present study:

- von Kármán vortices (a standard term in fluid mechanics literature)
- the *pipe-end vortex* (referred to as the "jet-wake vortex" by Huang and Hsieh (2002))
- *shear-layer vortices* (referred to as "jet shear-layer vortices" by Fric and Roshko (1994))

- *tendrils* (an evolution of the "horseshoelike structures" in the mixing-layer regime of Huang and Lan (2005)).

5.1 von Kármán Vortices

5.1.1 Overview

A conventional type of coherent structure in this flow was the von Kármán vortices, which contain rotational fluid originating in the boundary layers forming on the sides of the pipe and shed periodically into the cross-flow. These well-studied spanwise vortices are found in the wake of an infinite cylinder for Reynolds numbers higher than approximately 50. They are staggered and rotate in alternating directions, creating the von Kármán vortex street (Panton, 2005). von Kármán vortices are also shed from finite cylinders with a free end in the fluid when the aspect ratio is higher than a critical value (Kawamura et al., 1984), but their boundaries become complex towards the free end. Based on previous literature, it was anticipated that a von Kármán vortex street would form in the present experiments, as the aspect ratios of the present pipes and the cross-flow Reynolds numbers used presently were higher than the critical values.

5.1.2 Visual Experimental Results

When the jet was marked with either water soluble or fluorescent dye, the pipe-end vortex pulled the dye into the low-pressure wake of the pipe, from where it mixed into the von Kármán vortices, making them visible as they were shed and convected downstream. Water soluble dye became quite faded by the time it was shed with the von Kármán vortices

due to its high molecular diffusivity. Dibromofluorescein was much more clearly visible due to its less diffusive nature as discussed in section 3.4. Even so, von Kármán vortices always appeared with lower visibility than other structures.

When using the electrolytic precipitation visualization technique, precipitate particles were released from the pipe wall into the boundary layers that rolled-up into von Kármán vortices. As the lead precipitate particles were heavier than water, they were centrifuged away from the axes of the vortices, giving a "shell-like" appearance to the vortices, rather than being uniformly distributed.

When observed in still images, the boundaries of these vortices were not defined very clearly; they were more easily observed in motion pictures. Examples of still images in which von Kármán vortices were visible are shown in Figure 15 and Figure 26. A frame-by-frame view of a video using a larger amount of methyl violet dye for visualization showing a top view of the von Kármán street is shown in Figure 27. Another frame-by-frame view from the side using the electrolytic precipitation visualization technique is shown in Figure 28.

The complex three-dimensionality of the von Kármán vortices is easily observed in Figure 29. Though sufficiently away from the pipe-end, the vortices can be approximated in two-dimensions, Figure 29 shows small streamwise vortices and interactions between the vortices making the von Kármán vortices three-dimensional.

5.1.3 Origin

As mentioned previously, von Kármán vortices derive their vorticity from the

pressure gradient that exists around the exterior surface of the pipe as shown by the boundary layers forming in this location, and the von Kármán vortices are shed alternately from the two sides of the pipe forming a "street" of counter-rotating vortices, as shown in Figure 27. The exact ways by which the circulation of these vortices is preserved beyond their visible spanwise ends have not been examined in detail in the present study. In the near field, these vortices terminated at the end-plate on the lower end and tended to extend upstream towards the pipe near its free end.

5.1.4 Evolution

Unlike the infinitely-long vortices that would ideally be shed from an infinite cylinder, the vortices in the present experiments were of finite spanwise extent. In the near field, the vortex axes were approximately vertical away from the pipe tip, but they became inclined toward the pipe tip at their upper extremities. In contrast, Kawamura et al. (1984) found that von Kármán vortices were inclined away from the free end of their finite cylinder (this work was at the higher Reynolds number of 32 000). A rough explanation for the difference in inclinations is provided schematically in Figure 30. For the finite cylinder case, the inclination of the von Kármán vortices can be attributed to the upwash that occurs on the downstream side of the cylinder, as documented by Kawamura et al. In contrast, in the present flow, there was a downwash that occurred along a large part of the lee-side of the pipe, as documented by Huang and Hsieh (2002) for comparable momentum-flux ratios as those considered presently. As illustrated in Figure 30, the resulting streamwise fluid velocity at the level of the tops of the von Kármán vortices would be higher than that in their main spans for the free-end cylinder case, whereas the opposite would happen in the present

case. This difference in convection velocities of the upper portions of the vortices would likely be responsible for the difference in their inclinations.

In the far field, it was not completely clear how the upper parts of the von Kármán vortices evolved as their visibility was hindered by further dye diffusion. It was also hindered due to their interactions with other types of coherent structures. Past research on finite cylinders (Dunn, 2004; Kawamura et al., 1984) has demonstrated that, near their free ends, von Kármán vortices have cells of slightly lower frequency than the frequency in their main spans. However, as the visualizations used in the present experiment were not optimized for showing the von Kármán vortices, such cellularity was not apparent. Moreover, the flow field near the end of a finite cylinder is quite different from the one near the end of the pipe in the present work and it is difficult to speculate whether any similarity in cellular patterns for the two cases would exist.

5.2 Pipe-End Vortex

5.2.1 Overview

When observed on the centreplane of the flow field, this vortex appeared to rotate about an axis normal to both the pipe axis and the cross-flow direction. It was a standing vortex, as it did not become detached and transported downstream at either regular or irregular time intervals. Its extent was confined to the wake of the pipe from immediately below the free end to a location that was a few pipe diameters below the free end. This vortex was driven by the jet fluid as it was forced downstream in the cross-flow direction.

Under certain flow conditions, it entrained a significant part, or even most, of the jet fluid.

5.2.2 Visual Experimental Results

Injection of methyl violet dye in the jet fluid made the overall shape of the pipe-end vortex quite visible, in the form of a purple, rotating cloud. The fluorescent dye excited by a laser-light sheet successfully revealed the internal complexity of this vortex, as shown in Figure 17. This vortex was also visible when using the electrolytic precipitation visualization technique, as seen in the images extracted from a motion picture in Figure 28.

Beyond the downstream end of the pipe-end vortex, the jet fluid was visible only within a path that was much narrower than the pipe inner diameter, as can be seen in Figure 31 as well as in Figure 32. It can also be noted that on the plane of symmetry, downstream of the pipe-end vortex, the upper boundary of the jet fluid drops back down to approximately the horizontal level of the pipe end. This is shown in Figure 26 as well as in Figure 16 and Figure 17. At sufficiently low momentum-flux ratios, all of the jet fluid appeared to be pulled downward on the lee-side of the pipe. At higher momentum-flux ratios, some or all of the jet fluid was convected downstream at elevations higher than the level of the pipe end.

Away from the plane of symmetry, the jet fluid spilled over the edge of the downstream half of the pipe away from the plane of symmetry. Evidence of this can be seen near the downstream pipe tip in the image shown in Figure 26; for clarity, this is also illustrated, in an exaggerated fashion, in the sketch included in the same figure.

5.2.3 Origin and Evolution

The axis of this vortex is likely in the form of two partial rings, the ends of which presumably terminate on either side of the pipe, at two locations somewhere below the free end. These axes must allow for the previously discussed rotation in the plane of symmetry as well as for movement within a plane perpendicular to the axis of the pipe. Thus, one may speculate that the pipe-end vortex has circulation patterns similar to those in the cross-section of Hill's spherical vortex, shown in Figure 33 (Panton, 2005). A secondary axis of this vortex could be another partial loop terminating on either side of the pipe at the pipe tip, which would account for jet fluid spilling over the sides of the downstream edge of the pipe as discussed in 5.2.2. Figure 34 illustrates a possible shape of the axis of the pipe-end vortex which is compatible with the observed flow patterns. The time-averaged structure of this vortex on the vertical cross-section of the flow has been documented in detail by Huang and Hsieh (2002; 2003) for a range of momentum-flux ratios from 0.015 to 25 with a constant pipe size and a constant cross-flow Reynolds number of 2074. They found that, for momentum flux ratios less than approximately 0.9, at least part of the jet fluid is entrained downward in the wake of the pipe as illustrated by comparison of the images in Figure 35.

As mentioned previously, the energy input that maintained this vortex came from the jet and cross-flow fluid flowing over and around the top of the pipe, then being subsequently entrained into the low pressure region on the lee side of the pipe. The flow structure within the pipe-end vortex was complex, as revealed by the laser sheet highlighting the cross-section of the vortex when fluorescent dye was used, as shown in Figure 17. This complex structure within the vortex has not yet been investigated in great detail, as it was not a

primary objective of this study.

In the present study, when the momentum-flux ratios exceeded approximately 0.002 within the range of tested Reynolds numbers, the pipe-end vortex extended upward beyond the stack tip, displacing the upper interface between the jet fluid and the cross-flow fluid. This flow case was within the downwash regime of Huang and Hsieh (2002). The primary jet flow tracked around the edge of the pipe-end vortex as it exited from the stack. At the downstream end of the vortex, the jet-fluid that was not entrained by the pipe-end vortex convected downstream at a spanwise level at which it would have been had it not been initially deflected upward by the raised pipe-end vortex.

The previously mentioned narrowing of the transverse projection of visible jet fluid at the downstream end of the pipe-end vortex can be explained by the fact that, for the previously mentioned typical flow conditions, a good deal of the jet fluid was entrained downward. Additionally, some of the remaining jet fluid was stretched spanwise into tendrils, as pointed out in section 5.3.4. The high rate of stretching in the symmetry plane of the flow, in combination with the reduced amount of jet fluid being convected downstream, leads to a reduction in the width of the jet as evidenced by the significant narrowing of the transverse footprint of the dyed fluid.

5.3 Shear-Layer Vortices

5.3.1 Overview

Shear-layer vortices formed at different downstream locations and had different

structures depending on the flow conditions. The vorticity contained in these vortices includes vorticity generated within the pipe-flow (Andreopoulos, 1985; Eiff et al., 1995; Fric and Roshko, 1994) as well as some of the vorticity generated along the pipe external wall as the cross-flow fluid flowed up and over the upstream tip of the pipe similar to that witnessed by Kelso et al. (1996) in their wall-issued flow. Although the vorticity vectors in the pipe flow lie on planes perpendicular to the pipe axis, their directions change continually off such planes as the shear-layer vortices form and evolve downstream.

5.3.2 Visual Experimental Results

As the cross-flow fluid that was entrained into these vortices did not flow past the outer diameter of the pipe where the lead foil was located, the electrolytic precipitation technique did not offer any additional information about these vortices. As these vortices formed in the near-field, where dye diffusion was not excessive, their overall structure did not appear to be significantly different when viewed either using the water-soluble dye or the fluorescent dye. Even so, illumination of the fluorescent dye with the laser sheet resulted in a sharper view of the cross-section of these vortices. An overall view of shear-layer vortices can be seen above the pipe exit at the interface between the jet fluid and the cross-flow fluid in Figure 26. A cross-section of these vortices can be seen in the same location in Figure 17. The evolution of these vortices is depicted in Figure 36, in which overlaid ellipses mark a single vortex moving downstream. The ellipse highlights the single vortex from shortly after its generation to after it has been stretched out into a tendril pair. As the cross-flow fluid that was entrained into these vortices did not flow past the outer diameter of the pipe where the lead-foil was located, the electrolytic precipitation technique was not useful for the

visualization of the shear-layer vortices.

5.3.3 Origin

Because the pipes used were non-transparent, it was not possible in the present experiments to provide direct evidence for the connection of the vorticity of the shear-layer vortices and the vorticity within the pipe. However, as cited in section 5.3.1, this is generally accepted to be the case. As the cross-flow fluid was not marked upstream of the pipe, the generation of vorticity at the upstream pipe tip was also not witnessed. These two sources of vorticity are in opposing directions.

The Kelvin-Helmholtz instability is observed when one layer of fluid moves at a speed different from that of an adjacent layer (Lindsay, 1984). The most common example of this flow is the two-dimensional mixing layer between two adjacent parallel streams, each of which has a uniform velocity of different magnitude and which are initially separated by a splitter plate. Under these conditions, a perturbation in the flow will evolve into a sequence of two-dimensional vortices. Although far from being two-dimensional, the present flow contains a shear-layer between the jet fluid and the cross-flow, which is subject to a Kelvin-Helmholtz instability mechanism and generates shear-layer type vortices (Fric and Roshko, 1994; Huang and Lan, 2005). The initiation of the shear-layer vortices was most easily noticeable on the plane of symmetry of the flow, but they are also visible in views looking down upon the pipe as in the frames extracted from a video in Figure 36. For the previously mentioned typical conditions, the vortex lines have horseshoe-like initial shapes connecting into opposing sides of the pipe.

5.3.4 Evolution

Following their generation, these vortices evolved in ways that depended strongly upon the momentum-flux ratio and, possibly, on other flow conditions. In general, at a constant cross-flow Reynolds number, at momentum-flux ratios lower than $R = 0.1$, the frequency of the vortices was relatively higher and they rolled in a direction of rotation such that their tops travelled downstream. Huang and Lan (2005) referred to these vortices as mixing-layer type vortices. A sketch of a cross-section of shear-layer vortices in this regime is shown in Figure 37.

The vortices in Figure 36 were within the mixing-layer type regime, as defined by Huang and Lan. The fluid at the uppermost extreme of the shear-layer vortices in Figure 36 was observed to be moving more slowly than the cross-flow fluid. Considering that, in this regime, the heads of shear-layer vortices rotate clockwise, one would infer that their cores would move with an even lower velocity in the z- direction. The convection velocity of the axes of the shear-layer vortices while they were above the pipe-end vortex was calculated from rough measurements of their streamwise displacements using the image sequence in Figure 36. In this region, the axes of these vortices were convected downstream at approximately 48 mm/s, which was roughly 0.8 times the upstream cross-flow velocity of 60.6 mm/s and approximately 2.9 times the jet-fluid initial velocity of 16.7 mm/s. This is consistent with the fact that the convection velocity of vortices within a two-dimensional mixing layer is intermediate between the velocities of the two streams.

Holding the cross-flow Reynolds number constant and increasing the jet Reynolds number (hence increasing the momentum-flux ratio above the initial test value of 0.076), the

fluid velocity of the tops of the vortices began to exceed the local cross-flow velocity, as evidenced by the fact that the tops of the vortices showed signs of rotation in the opposite direction. As the jet Reynolds number further increased, further increasing the momentum-flux ratio, the passing frequency of the vortices continued decreasing and this counter rotation became stronger and larger in size until the structure appeared to have a cross-section with a mushroom-like appearance. At higher momentum-flux ratios, the mixing-layer type vortex portion was overcome by the backward rolling vortex and a portion of the mixing-layer type vortex was essentially "swallowed" into the larger and stronger backward rolling vortex. A sketch of this is shown in Figure 38.

Shear-layer vortices had complex interactions with other coherent structures in their vicinity as they were convected downstream. The details of such interactions depended upon the values of the momentum-flux ratio and the cross-flow Reynolds number. Previous researchers have observed that shear-layer vortices in higher momentum-flux ratio jet flows ($R > 9$ (Eiff and Keffer, 1997b)) form closed rings, similar to those observed in common free jets. Although it is possible that, even at low momentum-flux ratios, shear-layer vortices also evolved to closed loops, no direct evidence to support this possibility has been found either in the present or in earlier studies.

Regardless of whether the shear-layer vortices closed or not, for certain flow conditions the lower portion of the vortex was entrained into the low-pressure region on the lee side of the pipe while the upper portion of the vortex moved downstream with the cross-flow. The side portions of the vortices that were stretched have been identified as tendrils, which are discussed in the following section.

5.4 Tendrils

5.4.1 Overview

Tendrils were evident as thin filaments, resembling tornados and attached in pairs at their upper extreme by the "heads" of the shear-layer vortices. As subsequently discussed in more detail, they are believed to exist in counter-rotating pairs. The tendrils only existed for a certain range of flow conditions described in Chapter 6. If the momentum-flux ratio was lower than a certain level, these structures did not exist, as all of the fluid from the jet and the entire shear-layer vortices were entrained into the pipe-end vortex forming behind the tip of the pipe. At momentum-flux ratios sufficiently high, the momentum of the jet was able to overcome the suction force of the low-pressure region behind the pipe, preventing the lower half of the shear-layer vortices from being entrained downward. Observations of the present flow show that the tendrils were parts of evolving shear-layer vortices, and so it is the shear-layer vortices that were the source of vorticity for the tendrils.

5.4.2 Visual Experimental Results

Like the shear-layer vortices, the tendrils were visible with the use of both water soluble dye as well as fluorescent dye. As these structures were primarily comprised of jet fluid, they were not visible when only the electrolytic precipitation technique was employed. Dyes entrapped in the tendrils seemed to remain at high concentrations as the tendrils were convected downstream. Due to their extremely narrow cross-sections as well as their tendency to wander transversely, the tendrils were not easily seen when vertical laser sheets were used. A clear side-view of these structures can be found in Figure 26 and a top-view of

the evolution of these structures from the shear-layer vortices is shown in Figure 36.

5.4.3 Origin

As mentioned previously, the tendrils must have received their vorticity from the shear-layer vortices. As the shear-layer vortices were convected downstream from the pipe-end vortex, they were further stretched spanwise as their bottoms were pulled downwards. Therefore, tendrils are the stretched sides of the shear-layer vortices. They appeared in counter-rotating pairs, which became staggered in a sequence reminiscent of the von Kármán vortex street. The bottoms of the tendrils were initially inclined toward the pipe at the bottom of the pipe-end vortex. Figure 39 shows a sequence of images obtained while all flow conditions were maintained unchanged and dye was slowly introduced to the jet. Image a) shows only a thread of the shear-layer vortices. Image b) shows the bottoms of the shear-layer vortices being entrained down behind the pipe while their top portions were pulled downstream. The links between the two extremes – the tendrils – can be barely seen. Images c) and d) show the same features as image b), but containing more dye, which makes their features more visible.

5.4.4 Evolution

As the tendrils moved downstream, their initial inclination toward the base of the pipe-end vortex was reversed and they slowly rotated toward a vertical orientation and beyond. This change in inclination can be also explained by the same rationale that was presented for the von Kármán vortices in section 5.1.4. To explain their interactions with other coherent structures, one needs to discuss a number of possible mechanisms.

One possibility is that these tendrils linked up with the von Kármán vortices. Because they originated from ring-like vortices, each member of a pair of tendrils was rotating in the opposite direction from the other member, in a fashion similar to that of pairs of consecutive von Kármán vortices. In general, the tendrils were generated at a higher frequency than the von Kármán vortices; however, this does not necessarily prevent members of the two sets from connecting to each other, as in the case of von Kármán vortices of different frequencies linking up on opposing ends of cellular boundaries (Dunn and Tavoularis, 2006). Eiff and Keffer documented this process at a significantly higher momentum-flux ratio as well as Reynolds number ($R = 9$, Re = 22 000) than were attained in these experiments. In their results, they proposed that a lock-in existed, as described in section 2.4, between what they referred to as jet-wake vortices (potentially analogous to the tendrils) and the shear-layer vortices and they further proved that a lock-in existed also between the jet-wake vortices and the von Kármán vortices. It is therefore conceivable that, at a low momentum-flux ratio, a similar set of lock-ins exist. Zdravkovich (2003) pointed out that the vortex "braiding" (by which long, narrow vortices twist about themselves in a nearly regular pattern) that tends to occur in the far field of the vortical structure behind finite cylinders is the interaction of the tops of von Kármán vortices. Similar braiding was witnessed presently in the far field of the tendrils, as can be seen in the side views of Figure 40 as well as in Figure 26, or downstream in the top views shown in Figure 27. This further supports the possibility of a link between the tendrils and the von Kármán vortices.

Another possibility is that the tendrils all tied into two streamwise vortices not shown by any visualization method used in this study. Streamwise vortices have been noted by

many finite cylinder researchers and are shown in Figure 3 above in the sketch by Kawamura et al. (1984). Though this possibility is less likely as both jet and cross-flow fluids were marked and no such vortices were noted, it is still conceivable that this was occurring.

Figure 26 – Overview of main coherent structures of interest ($d = 18.79$ mm, $R = 0.076$, $Re_j = 327$, $Re_\infty = 1330$)

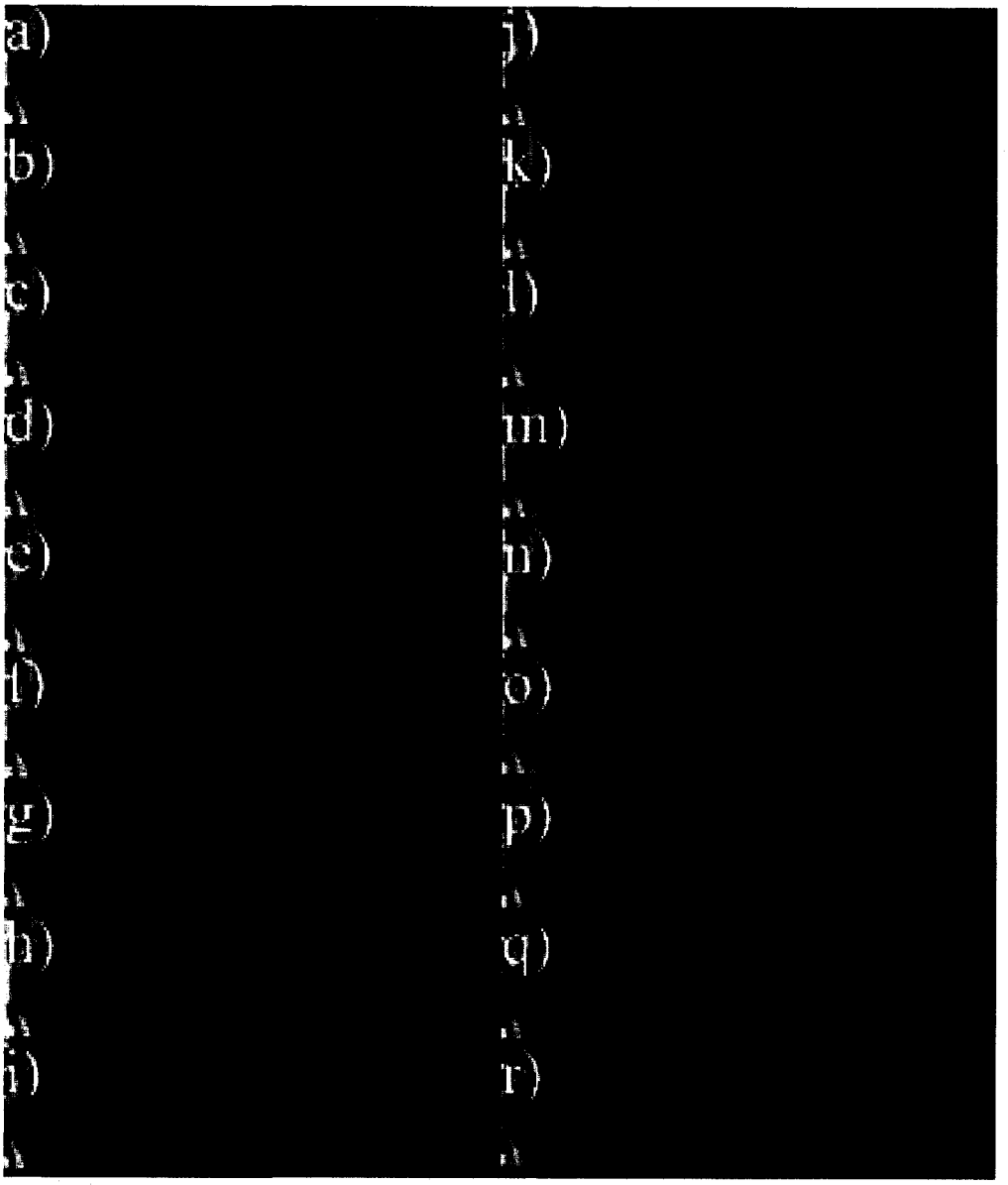

Figure 27 – Frame-by-frame top view of flow structure (Δt = 1/30 s, d = 18.79 mm, R = 0.076, Re_j = 327, Re_∞ = 1330)

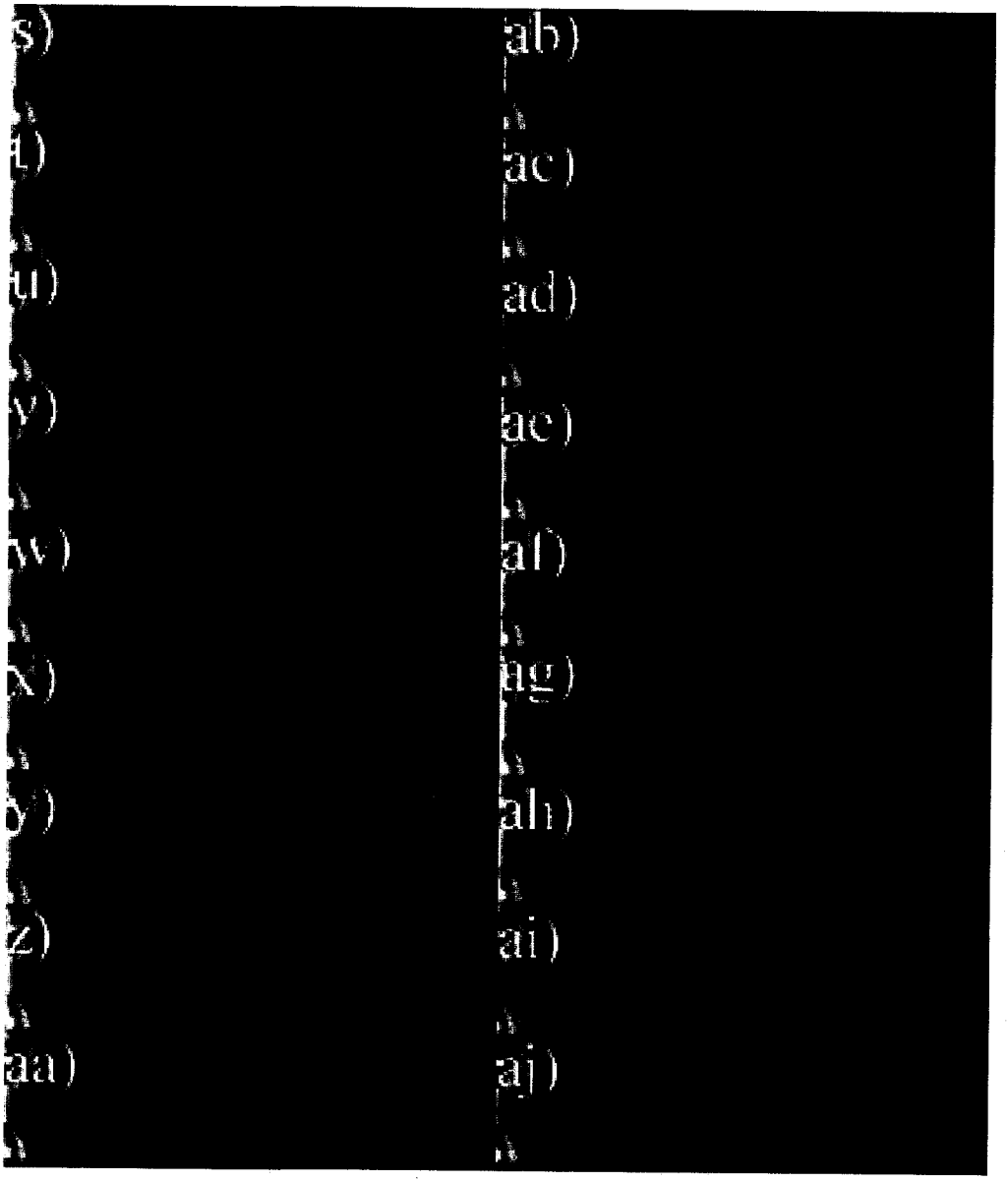

Figure 27 (continued)

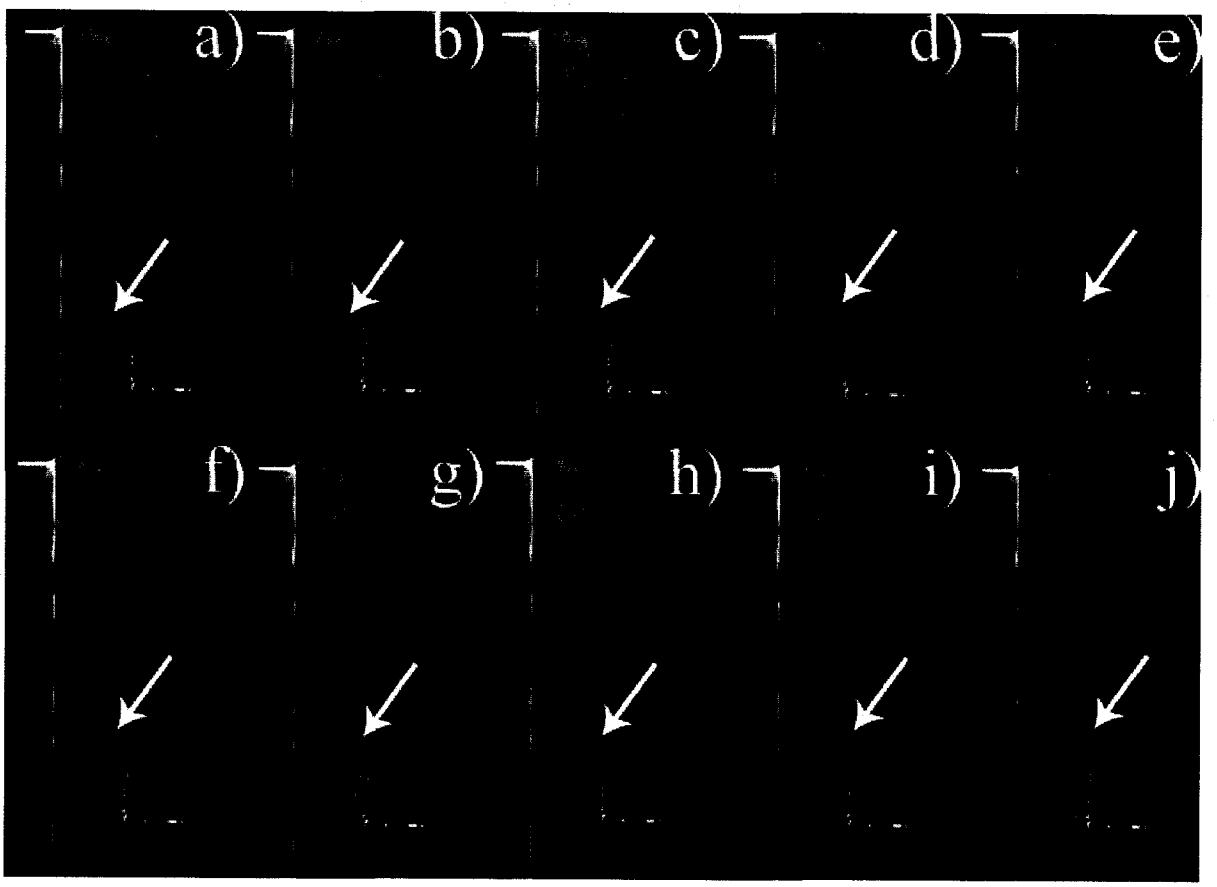

Figure 28 – Frames of a video showing von Kármán vortices using the electrolytic precipitation visualization technique. The arrow follows a single von Kármán vortex (Δt = 1/30 s, d = 18.79 mm, R = 0.076, Re_j = 327, Re_∞ = 1330)

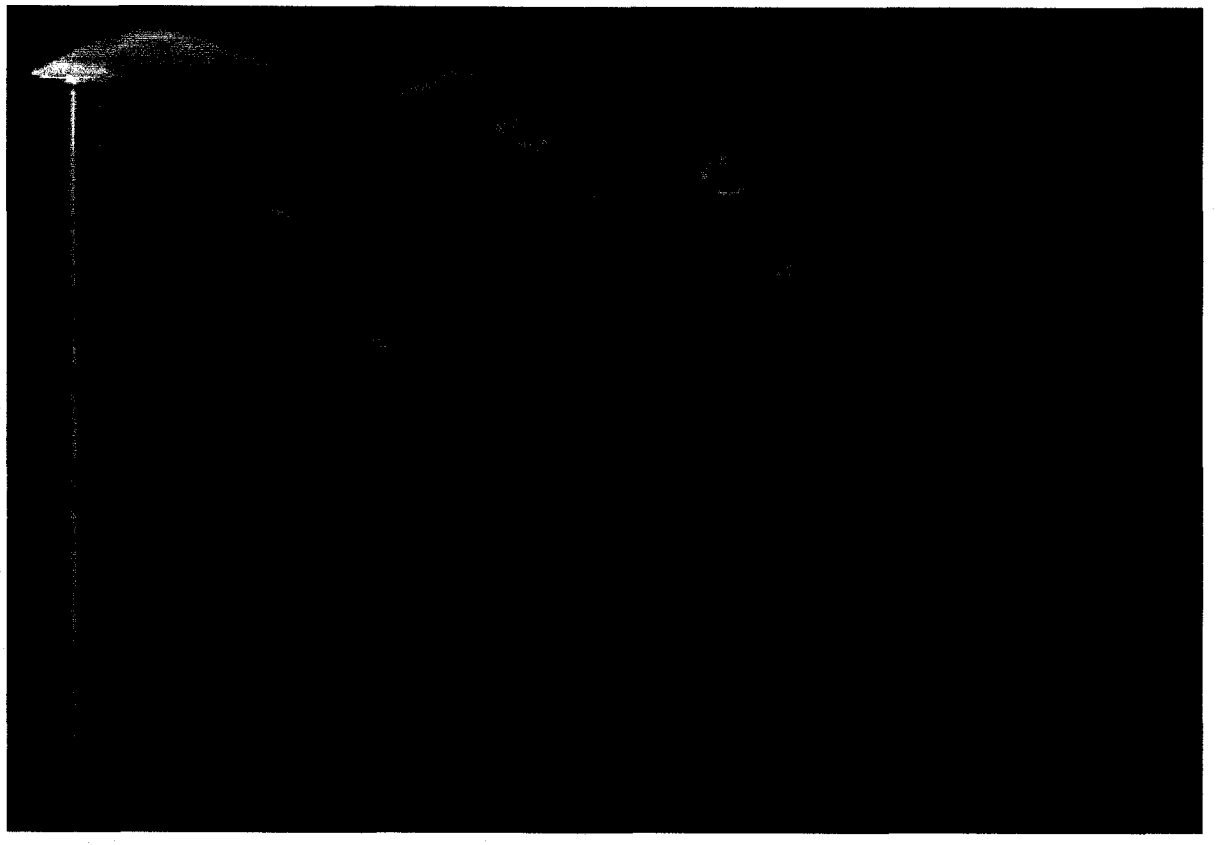

Figure 29 – Flow visualization image with fluorescent dye showing three dimensionality of the von Kármán vortices (d = 19.38 mm, R = 0.21, Re_j = 206, Re_∞ = 502)

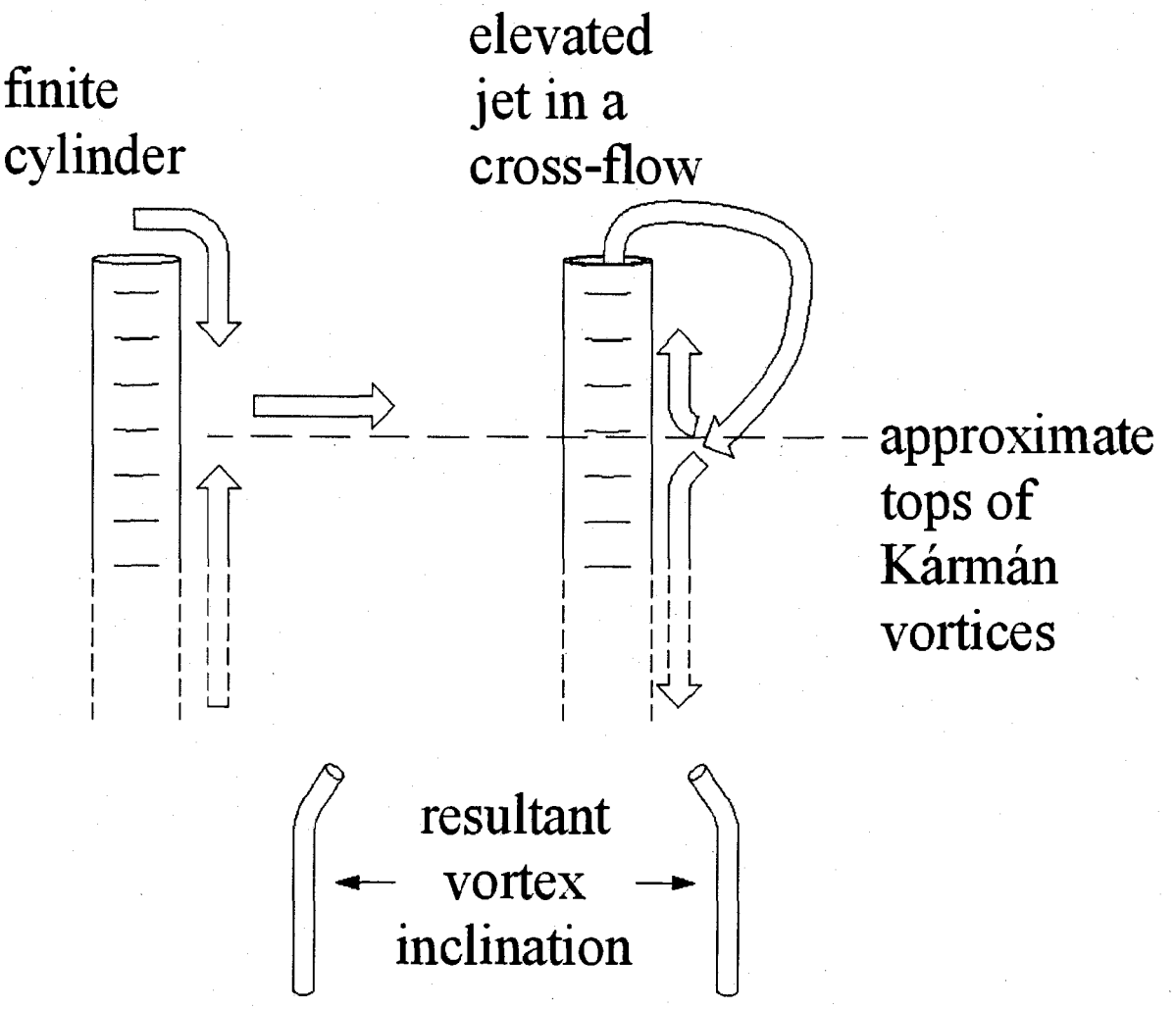

Figure 30 – Flow structure comparison of finite cylinder versus low-momentum elevated jet in a cross-flow

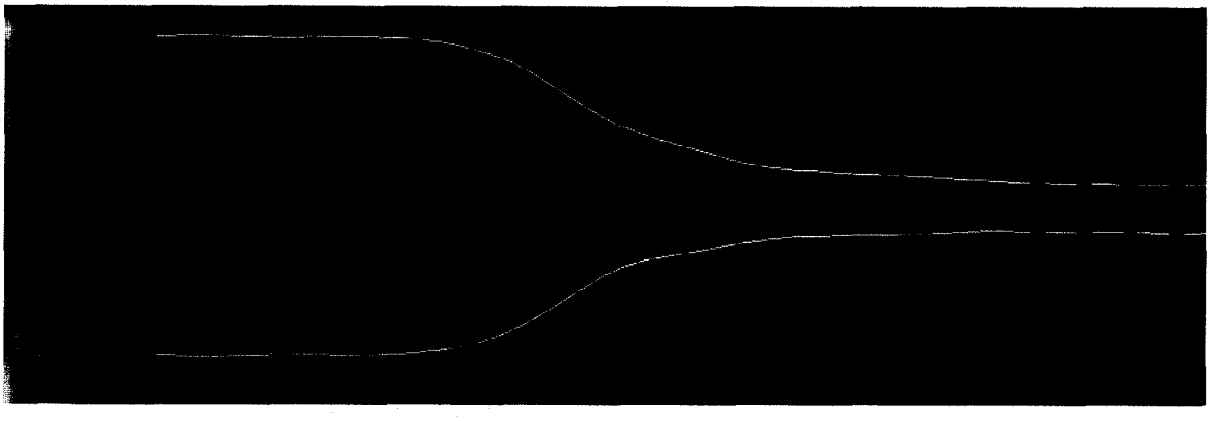

Figure 31 – Transverse boundaries of the pipe-end vortex ($d = 18.79$ mm, $R = 0.076$, $Re_j = 327$, $Re_\infty = 1330$)

Figure 32 – Cross-section of flow in x-z plane, $0.5d$ below pipe tip. The pipe-end vortex is visible immediately downstream of the pipe at the left of image and a cross-section of tendrils is visible at the right (d = 18.79 mm, R = 0.076, Re_j = 327, Re_∞ = 1330)

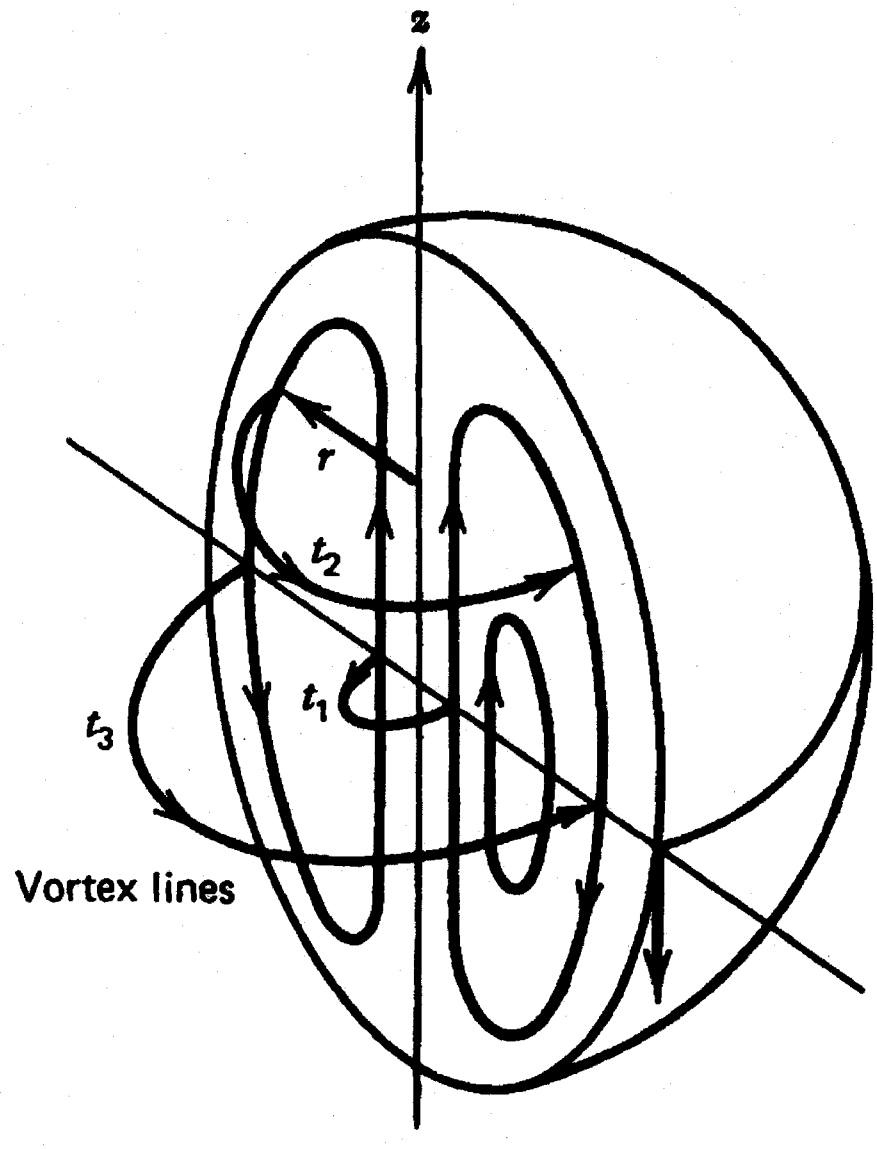

Figure 33 – Hill's spherical vortex (Panton, 2005)

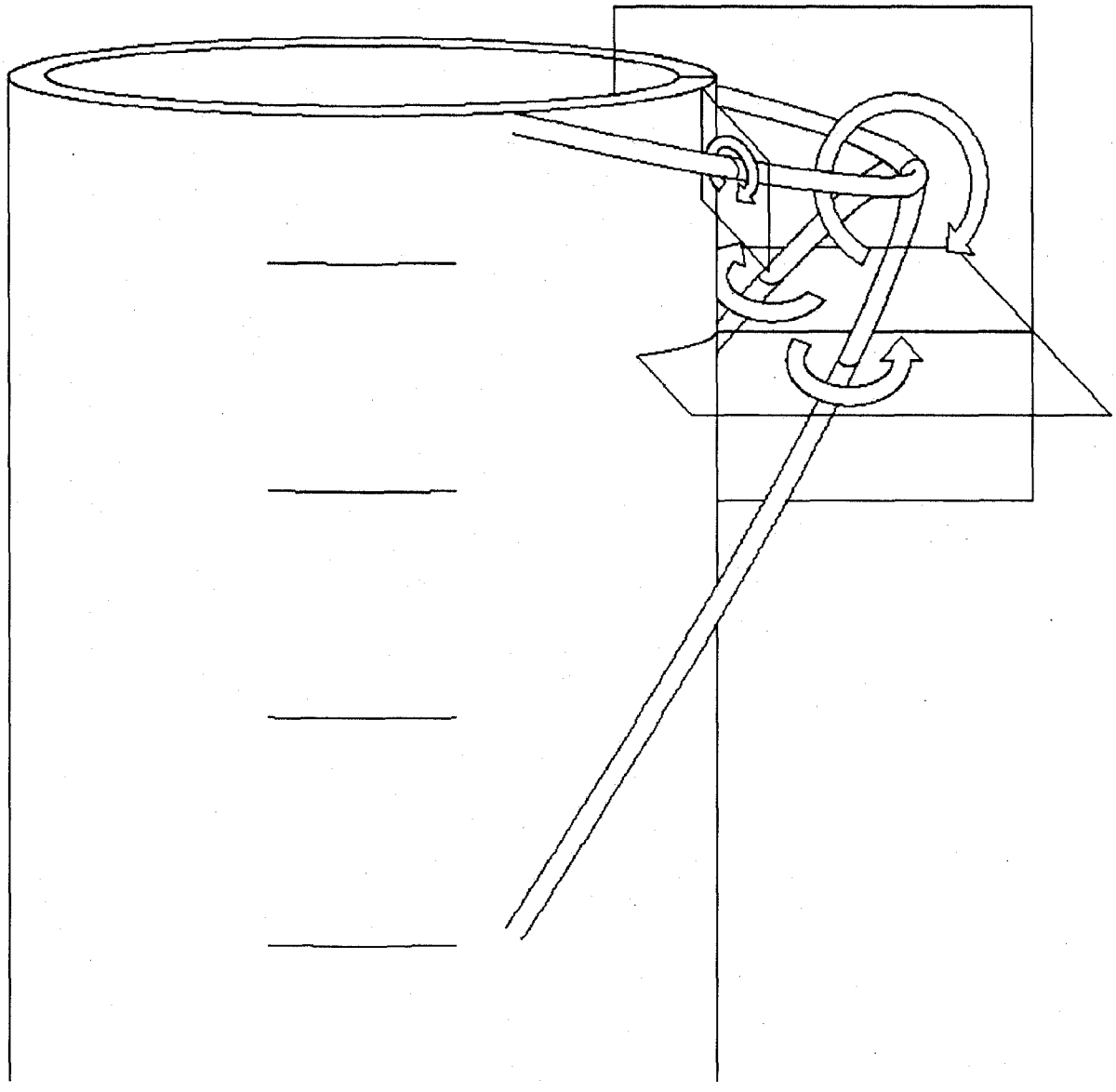

Figure 34 – Proposed axes for pipe-end vortex

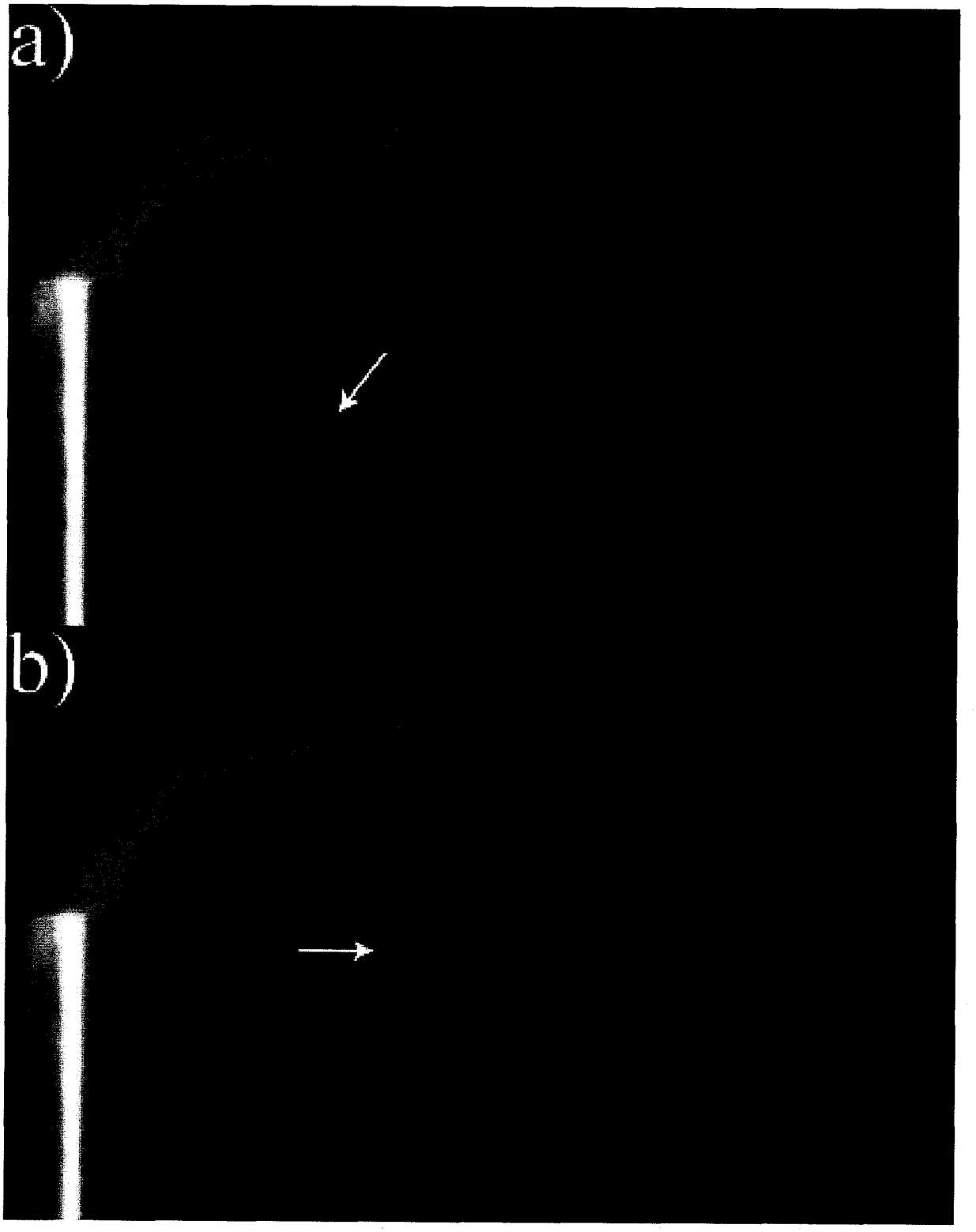

Figure 35 – Images showing presence of jet fluid behind pipe (d = 16.6 mm, Re_∞ = 1178) a) jet fluid being entrained behind pipe at R = 0.79 (Re_j = 936) b) no jet fluid being entrained behind pipe at R = 0.99 (Re_j = 1051)

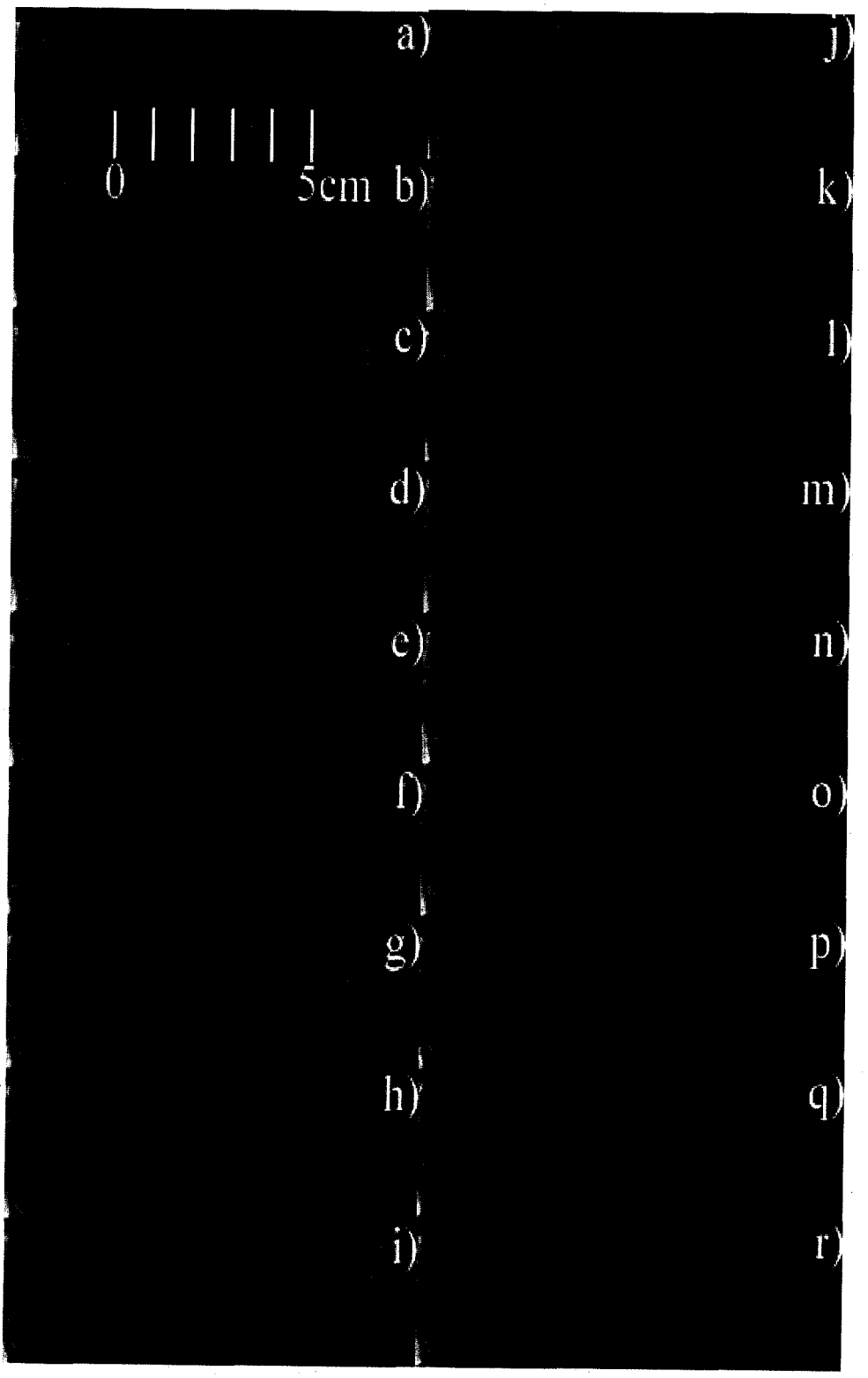

Figure 36 – Frames of a video showing a top view of the evolution of shear-layer vortices. An ellipse follows a single vortex as it is generated and evolves into a pair of tendrils (Δt = 1/30 s, d = 18.79 mm, R = 0.076, Re_j = 327, Re_∞ = 1330, v_∞ = 60.6 mm/s)

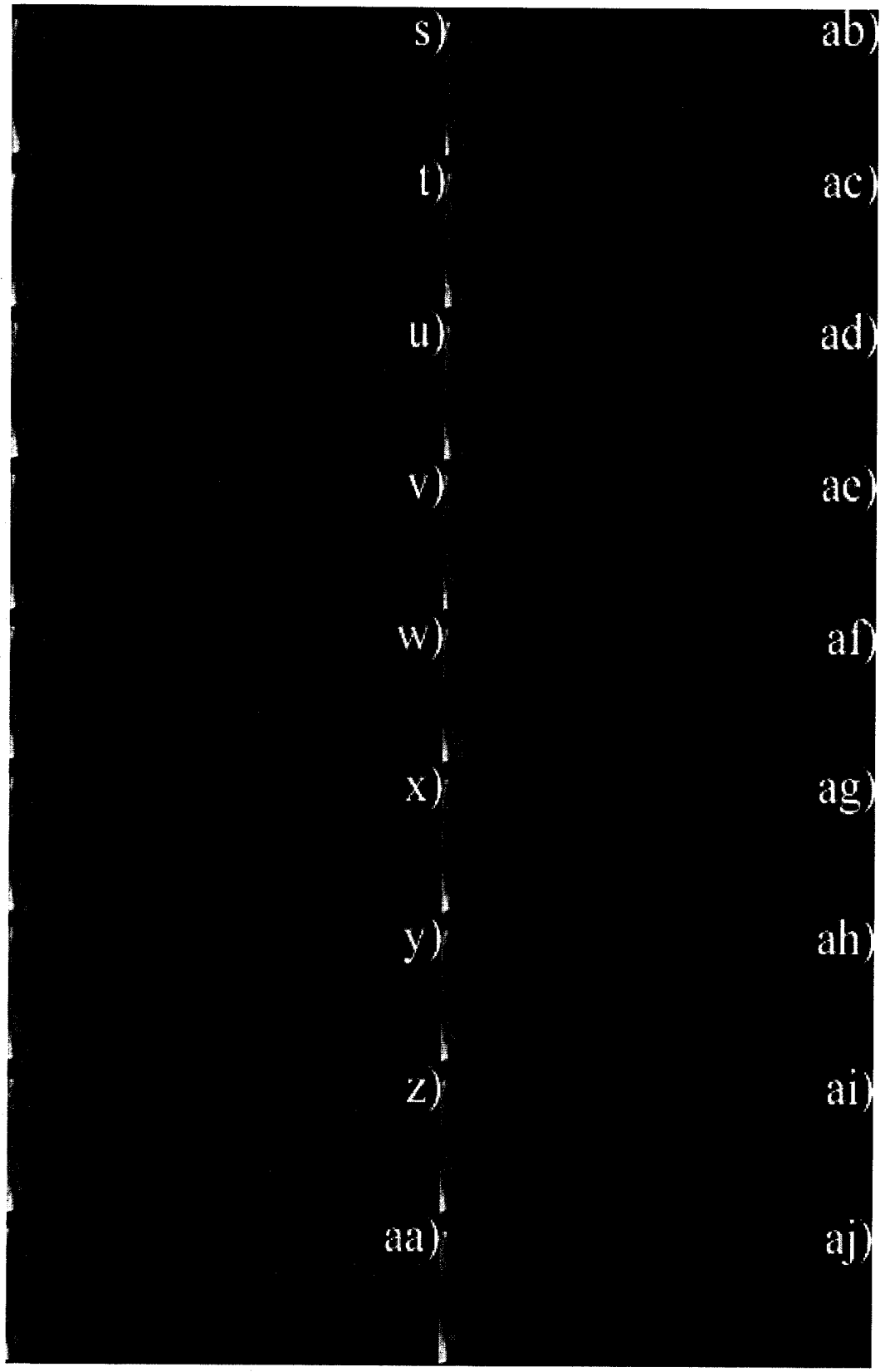

Figure 36 (continued)

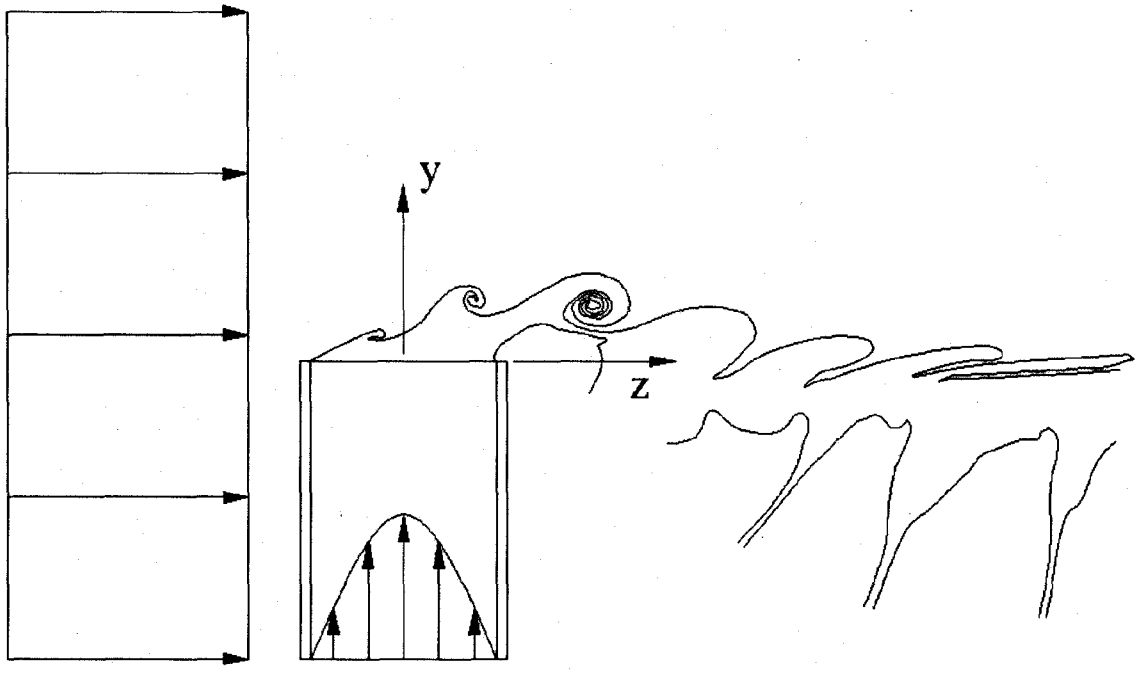

Figure 37 – Sketch of cross-section of typical mixing layer vortices (d = 18.79 mm, R = 0.076, Re_j = 327, Re_∞ = 1330)

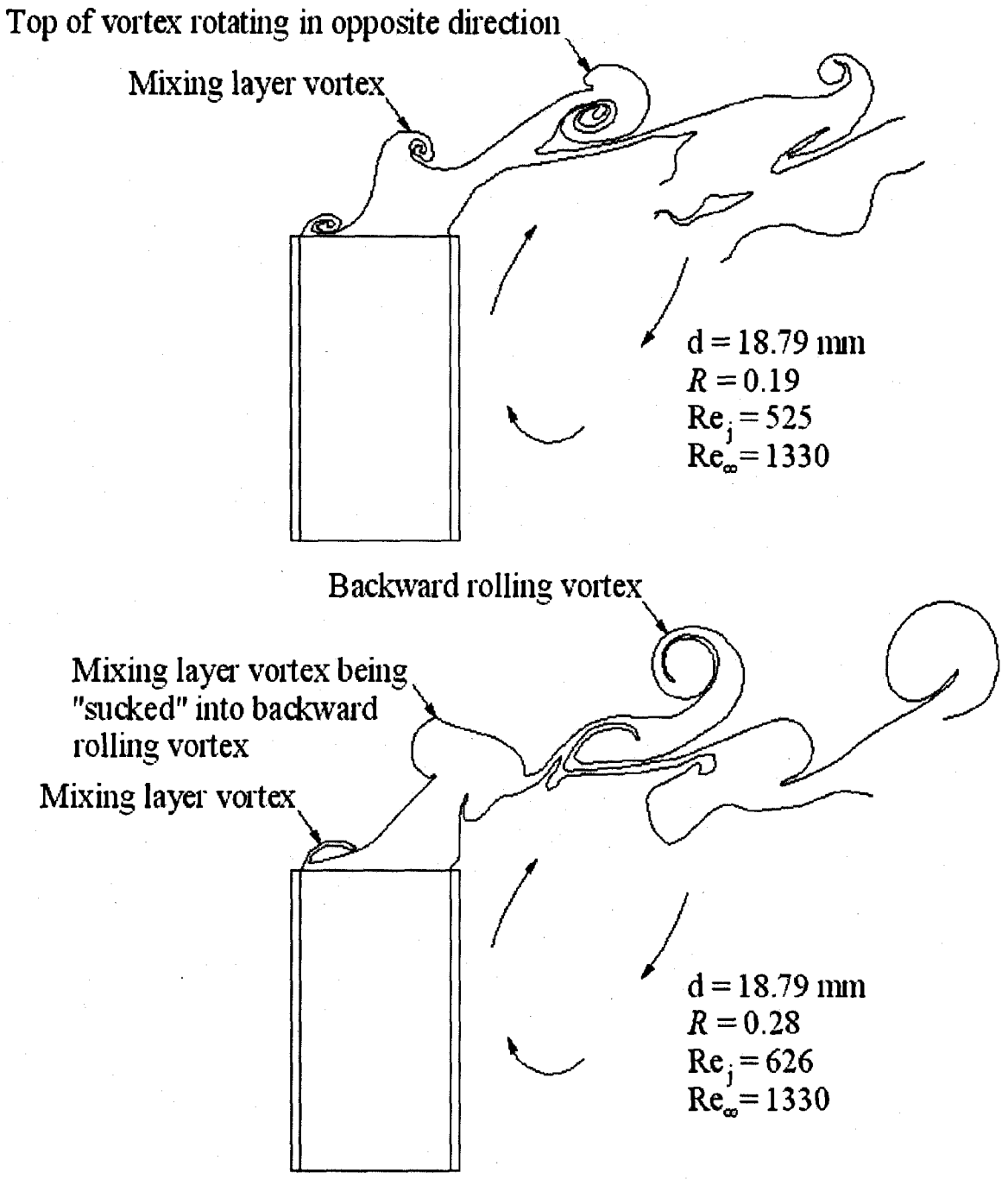

Figure 38 – Sketch of a cross-section of the onset of backward rolling vortices as momentum-flux ratio is increased

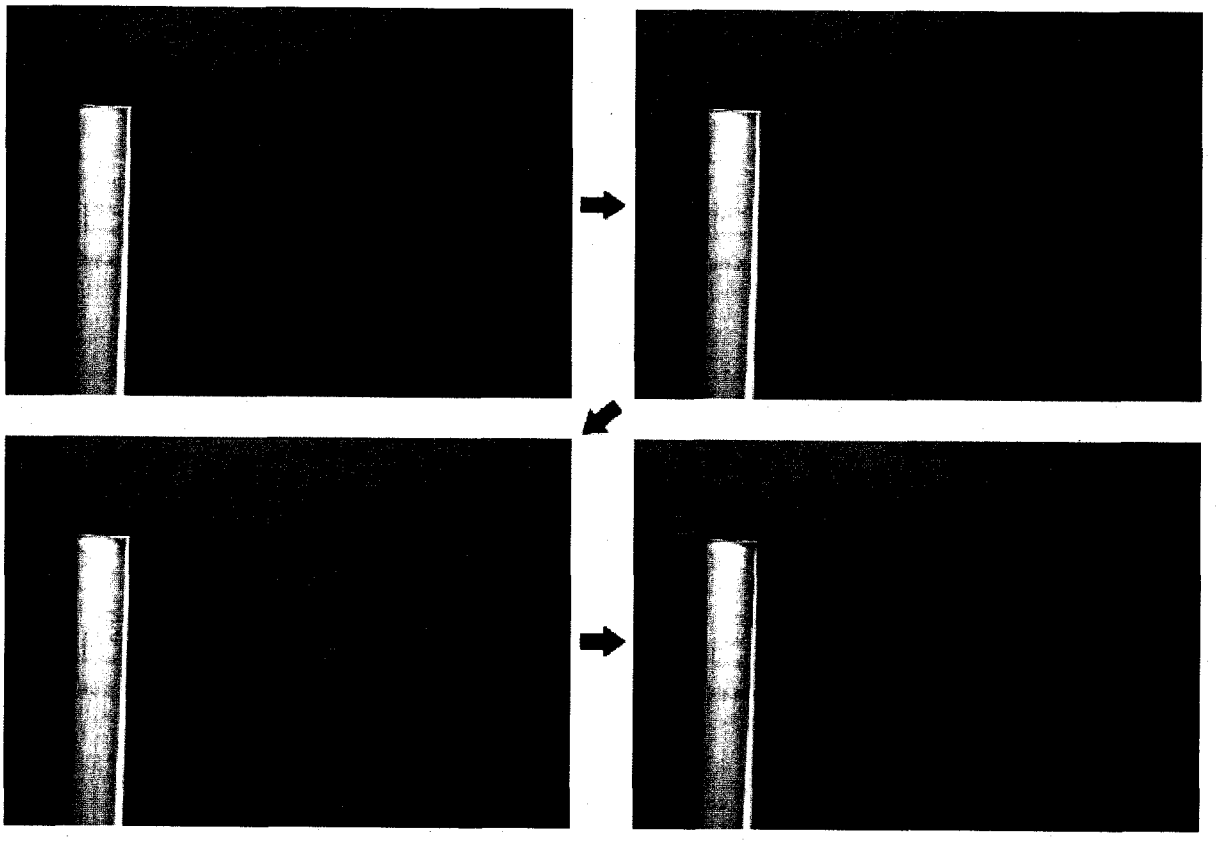

Figure 39 – Visualization showing the origin of tendrils by adding dye to jet fluid in otherwise constant flow conditions (d = 18.79 mm, R = 0.076, Re_j = 327, Re_∞ = 1330)

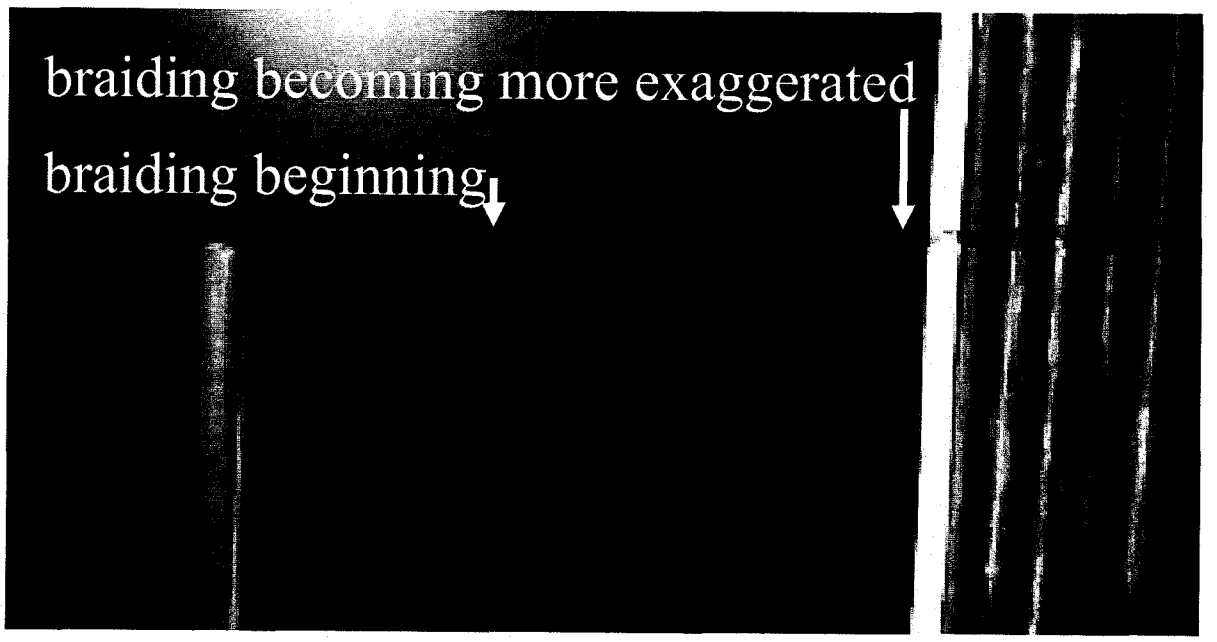

Figure 40 – Flow visualization image showing downstream braiding of tendrils (d = 18.79 mm, R = 0.076, Re_j = 327, Re_∞ = 1330)

Chapter 6 Quantitative Results

6.1 von Kármán Vortices

These vortices have been analyzed extensively in studies of flows past finite cylinders with a free end and were not an object of detailed measurement in the present experiments. Considering the relatively large aspect ratios of the pipes used here, it was expected that, away from the pipe end, the von Kármán vortices in the present flows would have the same properties as those shed by finite cylinders of comparable aspect ratios. This hypothesis was verified for a representative set of conditions: at a cross-flow Reynolds number of 510, the Strouhal number (estimated using the video analysis technique described in section 4.4) was 0.20, which is essentially equal to the value given by Zdravkovich (2003) for the same Reynolds number.

6.2 Pipe-End Vortex

Though the detailed structure of the pipe-end vortex was not an object of investigation in the present study, measurements were made of the overall size of this vortex. For all tested flow conditions, three dimensions of the vortex on its geometrical plane of symmetry, as sketched in Figure 41, were determined from the videos. It was not possible to measure the transverse width of the vortex, as top views of this vortex were obscured by

shear-layer vortices from above and von Kármán vortices from below. The three measured dimensions were plotted in Figure 41 normalized by the outer diameter of the pipe behind which the vortex formed. Though there was a good deal of scatter in parts of the plots, general trends were extracted from this figure. An additional observation that is not evident in this figure is that the size of the pipe-end vortex within the tested flow conditions seemed to depend mainly on the momentum-flux ratio and to be insensitive to the Reynolds number.

Dimension *a*, which represents the streamwise length of the vortex, did not vary greatly over a wide range of momentum-flux ratios tested in the present study. Only once the momentum-flux ratio exceeded approximately 0.1 did this dimension tend to increase. Similarly, for momentum-flux ratios lower than approximately 0.002, dimension *b*, representing the height of the vortex above the pipe tip, remained at zero. For higher values, the pipe-end vortex began moving upward, which is demonstrated by an increase of dimension *b*. Though the measurements of dimension *c*, representing the spanwise extent of the vortex below the pipe tip, displayed a lot of scatter, this dimension seemed to follow the opposite trend as dimension *b*. It remained nearly constant as R increased, until R reached a critical value near $R = 0.1$, above which dimension *c* began to drop off. The data in the range $0.0002 < R < 0.5$ have been fitted with exponential functions, which are merely meant to aid the eye in following the trends. These functions were as follows:

$$\frac{a}{D} = 2.08 - e^{-2.03 \cdot R}, \tag{13}$$

$$\frac{b}{D} = 1 - e^{-3.57 \cdot R} \text{ and} \tag{14}$$

$$\frac{c}{D} = 4.16 - e^{-0.6 \cdot R}. \quad (15)$$

6.3 Shear-Layer Vortices

6.3.1 Regime Categorization

The videos showing the shear-layer vortices were reviewed and were categorized into regimes in each of which these vortices had a distinct physical appearance and/or generation and evolution pattern. These regimes were marked in chart form in Figure 42, in which the two axes are the cross-flow Reynolds number and the jet Reynolds number. Other combinations of parameters were used as axes as well, but this choice gave the most clear distinction of the regimes. In this figure, different symbols are used to represent experimental points (i.e., combinations of values of the two Reynolds numbers) assessed to be in different regimes and shading of different colours is used to distinguish the ranges of these regimes. Lines of constant momentum-flux ratio were also drawn in solid black lines on the chart to illustrate a possible relationship between regime type and *R*-range. In total, nine regimes were identified, as follows:

- *vortex-free* regime
- *delayed-irregular-mixing-layer-type* regime,
- *delayed-regular-mixing-layer-type* regime,
- *irregular-mixing-layer-type* regime,

- *regular-mixing-layer-type* regime,
- *mushroom-like* regime,
- *backward-rolling* regime,
- *swing-induced* regime and
- *jet-type* regime.

The last two of these regimes (the swing-induced and the jet-type vortex regimes) were previously discussed by Huang and Lan (2005) and were not investigated in depth in the present study. Their presence was merely identified by a single flow case for each regime. The backward-rolling vortex regime was also previously noted by Huang and Lan and was confirmed in the present study. The mushroom-like vortex regime was not specifically identified by this name by Huang and Lan; however, they did observe this phenomenon and categorized it under the backward-rolling vortex regime. The mushroom-like vortex regime marked the boundary region between the lower momentum-flux ratio regimes and the backward-rolling vortex regime. It was sufficiently distinct in appearance to qualify as a separate regime. The regular-mixing-layer-type regime matched qualitatively the mixing-layer type vortex regime of Huang and Lan, but was renamed in the present study to be consistent with the regime names of the lower momentum-flux ratio flows observed in the present study. The vortex-free, delayed-irregular-mixing-layer-type, delayed-regular-mixing-layer-type, and irregular-mixing-layer-type regimes were all at either lower Reynolds numbers or lower momentum-flux ratios than those tested by Huang and Lan.

Only a small number of experimental results were available to document the vortex-free regime, however, the evidence was sufficient to identify this as a distinct regime. An example image is shown in Figure 43. No shear-layer vortices were observed in this regime. The exit from the pipe was smooth and the jet fluid was entirely entrained by the pipe-end vortex into the low-pressure region on the lee side of the pipe. The experiments that belonged to this regime had a low cross-flow Reynolds number, of the order of 500, as well as at low momentum-flux ratios, of around 0.01. The absence of the Kelvin-Helmholtz instability, which would have led to vortex generation, seems to be associated with the low Reynolds number rather than a low momentum-flux ratio, because vortices were generated at higher Reynolds numbers, even if the momentum-flux ratio was measurably lower than 0.01 as shown in Figure 42. One may speculate that there is a critical Reynolds number below which there is no Kelvin-Helmholtz instability, although it is possible that the value of this number depends on the momentum-flux ratio.

In the delayed-irregular-mixing-layer-type regime, shear-layer vortices were generated downstream of the leading edge of the pipe, albeit at an irregular rate. The vortices were then entrained into the low-pressure region behind the pipe. This regime can be seen in Figure 44 and was found at low jet Reynolds numbers below approximately 250 and at cross-flow Reynolds numbers in the range of 600 to 2000 giving a momentum-flux ratio below 0.08. This regime is speculated to continue to lower momentum-flux ratios as this would imply that the velocity difference across the interface between the jet-fluid and cross-flow fluid would increase, thus tending to make the mixing layer more unstable.

In the delayed-regular-mixing-layer-type regime, an example of which is shown in

Figure 45, the interface between the jet fluid and cross-flow fluid near the leading edge of the pipe was wavy but seemed to contain no vortices. Perturbations necessary for the Kelvin-Helmholtz instability were present in the fluid; however, they did not grow into vortices upon exit of the jet fluid into the cross-stream, but further downstream, at locations between the centreline of the pipe and one pipe diameter downstream of the trailing edge of the pipe. This regime existed at cross-flow Reynolds numbers higher than approximately 2000 up to the maximum tested value of 4000. This regime also existed at lower cross-flow Reynolds numbers; however, the boundaries separating it from neighbouring regimes had rather peculiar shapes. Below a jet Reynolds number of approximately 250, but above a cross-flow Reynolds number of approximately 600, the delayed-irregular-mixing-layer-type regime prevailed. At higher jet Reynolds numbers, up to at least 500 and above a cross-flow Reynolds number of approximately 1400, there was a border with the regular-mixing-layer-type regime at a momentum-flux ratio of 0.08. However, with the cross-flow Reynolds number in the range from 600 to 1400, the border was at a jet Reynolds number of approximately 360. This regime seemed to represent a transition between the delayed-irregular-mixing-layer-type regime and the regular-mixing-layer-type regime, and it appeared as a narrow band between the two regimes. One may speculate that this regime extends to lower cross-flow Reynolds numbers between the delayed-irregular-mixing-layer-type regime and the regular-mixing-layer-type regime, as it appeared to be a transition between these two regimes, at least at higher Reynolds numbers for which observations are available. Moreover, one may also speculate that this regime would not extend to higher jet Reynolds numbers when the cross-flow Reynolds number exceeds 2300, as Huang and Lan investigated flows in this Reynolds number range and did not explicitly mention any

significant delay in the roll-up of the shear-layer vortices.

The irregular-mixing-layer-type regime is similar to the delayed-irregular-mixing-layer-type regime, with the difference that the vortices are generated at the leading edge of the pipe rather than being delayed. This regime was observed within the momentum-flux ratio range of approximately $0.08 < R < 0.70$ and for cross-flow Reynolds numbers approximately between 600 and 850.

The regular-mixing-layer-type regime was described by Huang and Lan as the mixing-layer type vortex regime. It was this type of shear-layer vortices that was present in the typical conditions of Chapter 5 and is shown in Figure 13, Figure 17, and Figure 26. The vortices were generated very close to the leading edge of the pipe and their rates and sizes were consistent within a range of flow conditions. This regime existed for jet Reynolds numbers higher than about 360 and momentum-flux ratios between 0.08 and 0.22 up to a cross-flow Reynolds number of approximately 1600.

The mushroom-like vortex regime, illustrated in Figure 46, was at a higher momentum-flux ratio than the regular-mixing-layer-type regime and was the onset of the backward-rolling vortex regime. The vortices formed at the pipe exit as they did in the regular-mixing-layer-type regime; however, as they developed, the fluid velocity at the tops of the vortices began to exceed the cross-flow velocity and began rolling in the opposite direction. This backward-rolling vortex slowly gained strength until it was approximately even with that of the original forward-rolling vortex, creating a mushroom-like cross-section. Huang and Lan noticed the formation of mushroom-like vortices, but lumped their regime together with the backward-rolling vortex regime. In the present study, the mushroom-like

vortex regime existed for momentum-flux ratios between 0.22 and 0.35 for cross-flow Reynolds numbers between approximately 1100 and 1600.

As the momentum-flux ratio increased to take values in the range between 0.35 and 0.70, backward-rolling vortices became stronger than the original shear-layer vortices and appeared in the form shown in Figure 47. This type of pattern is classified within the backward-rolling vortex regime, following the regime classification by Huang and Lan.

The swing-induced vortex regime is shown in Figure 48 and, like the jet-type vortex regime shown in Figure 49, it is described by Huang and Lan (2005). The swing-induced vortex regime existed for momentum-flux ratios in the range from 0.70 to approximately unity. At higher values, the jet-type vortex regime prevailed, as Huang and Lan observed in their study and as was observed in the present study.

Figure 42 demonstrates that there is a difference in momentum-flux ratios between the regimes described by Huang and Lan and those identified in the present study. The boundary between the mixing-layer type vortex regime and the backward-rolling vortex regime of Huang and Lan appears at a slightly lower momentum-flux ratio. More peculiar is that the presently observed backward-rolling vortex regime overlaps with the forward-rolling vortex regime of Huang and Lan. The forward-rolling vortex regime, as described by Huang and Lan, was not observed at all in the present set of experiments. The range of momentum-flux ratios at which Huang and Lan observed backward-rolling vortices, $0.34 < R < 0.47$, was reproduced in the present study, but at lower Reynolds numbers ($1178 < Re_{\infty} < 1596$ versus $Re_{\infty} = 2051$ in the experiments by Huang and Lan). This difference supports the possibility

that the presence of the forward-rolling vortex regime is Reynolds number dependent.

6.3.2 Frequency Variation

The Strouhal number of the shear-layer vortices decreased with increasing momentum-flux ratio, as shown in Figure 50. The measurements in the range $0.0007 < R < 0.22$ could be fitted well by the power law

$$St_d = 0.77 \cdot R^{-0.65}. \tag{16}$$

The present results are in excellent agreement with those by Huang and Lan (2005) in the overlapping R-range of the two experiments. Huang and Lan focused on higher momentum-flux ratios, in the range $0.03 < R < 1.26$, and suggested the relationship

$$St_d = 9.14 \cdot e^{-27.98 \cdot R} + 4.88 \cdot e^{-6.57 \cdot R} + 0.61 \tag{17}$$

as representing their data.

Huang and Lan used a single pipe and varied the cross-flow velocity and jet velocity to achieve the desired cross-flow Reynolds numbers, jet Reynolds number and momentum-flux ratios. They varied their cross-flow Reynolds number from 2000 to 5000 and their jet Reynolds number from approximately 600 to 3000, concentrating on momentum-flux ratios between 0.03 and 1.4. In the present study, through varying the pipe size as well as the jet and cross-flow velocities, the cross-flow Reynolds number was varied from 450 to 4000 and the jet Reynolds number from 30 to 1000, giving momentum-flux ratios between 0.0002 and 1. A good deal of scatter is present in Figure 50 as the highest value for the coefficient of determination for the 43 data points used was 0.9587. The Reynolds number seemed to have

no apparent effect on the Strouhal number, as shown in Figure 51. It was also found that changes in the pipe diameter did not significantly influence the Strouhal number of the shear-layer vortices.

6.3.3 Velocity Development

In all regimes, the shear-layer vortices did not travel with a constant velocity along their paths. The convection velocity of the shear-layer vortices was measured roughly for a representative case with $R = 0.069$ and $\mathrm{Re_j} = 312$, for which the conditions are near the typical flow conditions mentioned in Chapter 5, which were $R = 0.076$ and $\mathrm{Re_j} = 327$. The location of the perceived axis of a single vortex was recorded in each frame of a video record as the vortex moved across the field of view. An example frame of this video is shown in Figure 52. Two sets of data for the vortex location were generated; the first set used all even-numbered frames, whereas the second set used all odd-numbered frames. This was done to reduce a possible bias in the perception of the exact location of the vortex axis in the images. These data sets were labelled as set 1 and set 2, respectively.

The two sets of locations of the vortex as it moved downstream are plotted in Figure 53, in which the origin was placed on the axis of the pipe. The results of the two sets essentially described the same smooth vortex trajectory. This figure confirms the previous observation made in section 5.2.2 that the interface between the jet and cross-flow fluid initially rose vertically and then dropped further downstream. The following expression was fitted well to the data for $0.25 < z/d < 6$

$$2\frac{z}{d}e^{-(\frac{z}{d}+0.8)}+0.17 \tag{18}$$

The displacements in the y and z directions were calculated for each pair of frames and the corresponding velocity components were calculated by adding two consecutive displacements within a set and dividing by two times the time difference between frames (i.e., four times the video frame rate). These velocity components were non-dimensionalized by the free-stream velocity and plotted versus downstream location in Figure 54. The following exponential expressions, fitted to the measurements of the two components of the vortex velocity over the range $1 < z/d < 6$, were found to represent the measurements fairly well

$$\frac{v_v}{q_\infty} = 0.6\left(1.25+\frac{z}{d}\right)e^{-0.85\cdot\frac{z}{d}} \tag{19}$$

$$\frac{w_v}{q_\infty} = 1-0.35\left(0.67+\frac{z}{d}\right)e^{-0.6\cdot\frac{z}{d}} \tag{20}$$

where v_v and w_v refer to the y- (vertical) and z- (streamwise) components of the vortex, respectively.

The variation of the vertical component of velocity conforms to the qualitative observations made in Chapter 5. The vortex initially moved upward as it was convected downstream, until it reached a maximum roughly equal to the jet bulk velocity at a location above the mid-point of the pipe-end vortex $\left(z/d \approx 1.25\right)$, after which it moved downwards again. Based on Figure 53 and Figure 54, the vortex appears to settle at a constant elevation,

approximately equal to the elevation of the pipe tip, near $z/d = 6$. The streamwise component of velocity of the vortex immediately following its generation increases steeply and seems to reach a local maximum when the vortex is above the downstream edge of the pipe. This velocity then drops slightly and then it increases steadily, to approaching the velocity of the cross-flow. Throughout the observed travel of the vortex, its convection velocity remained intermediate between the jet and cross-flow velocities, which is consistent with the qualitative observations discussed in Chapter 5. With the exception of the region over the pipe, the streamwise velocity of the vortex was much larger than the vertical one, showing that the jet is approximately aligned with the free stream. This is quite different from high momentum-flux ratio cases, in which the jet travels over a considerably longer distance before it approaches a streamwise orientation. Smith and Mungal (1998) documented the path of a wall-issued jet in a cross-flow for higher momentum-flux ratios. Their results, shown here as Figure 55, demonstrate that, for their case with the lowest documented momentum-flux ratio of 25, the centreline of the jet bent towards the streamwise direction rather gradually; when it reached one diameter downstream of the jet-exit axis, it had already risen to $3 \cdot d$ and was still rising. In contrast, in the present study, the axes of the shear-layer vortices only reached a maximum height of $0.5 \cdot d$ at the peaks of their upward travel.

6.4 Tendrils

6.4.1 PIV Results

Measurements were carried out with the PIV system described previously to ensure that the tendrils were indeed rotating. Velocity measurements were taken at the locations shown in Figure 56 and vorticity fields were calculated. A street of counter-rotating von Kármán vortex pairs convecting downstream can be identified in Figure 57. In contrast, Figure 58 illustrates a pattern of regular, albeit very weak, conter-rotating vortex pairs with a spacing that is much shorter than the spacing of von Kármán vortex pairs and apparently equal to the spacing of tendrils as observed by flow visualization. These vortex pairs are undoubtedly tendrils and have a vorticity that is consistently organized in space, unlike the background "noise" vorticity that is randomly distributed in the image.

6.4.2 Regime Categorization

Videos of each flow case were reviewed and each case was categorized into a regime in which the tendrils had a distinct generation and evolution. These regimes have been identified in Figure 59 in chart form using the same axes as those in Figure 42, as these axes also gave the clearest distinction of tendril regimes. In total, four regimes were identified, as follows:

- *pipe-end-vortex-suction* regime,
- *intermittent-tendril-formation* regime,
- *regular-tendril-formation* regime and

- *unsplit-shear-layer-vortex* regime.

The pipe-end-vortex-suction regime, shown in Figure 59 and Figure 60, corresponds to a low cross-flow Reynolds number and a low momentum-flux ratio. In this regime, the jet did not posses sufficient momentum to escape, even in part, the suction of the pipe-end vortex and, consequently, no tendrils were formed. This regime was found for cross-flow Reynolds numbers below approximately 2500 and momentum-flux ratios less than 0.08 within the tested conditions. One may speculate that this regime extends to lower momentum-flux ratios within the same cross-flow Reynolds number bounds, as such cases would correspond to an even weaker jet, which would be more easily pulled downward into the pipe-end vortex. This regime could also extend to slightly higher momentum-flux ratios, but not likely above the value of $R \approx 0.08$ as it is speculated that above this value, the jet would have sufficient momentum to convect downstream.

The regular-tendril-formation regime, shown in Figure 59, corresponds to a momentum-flux ratio and a jet Reynolds number that were higher than those in the previous regime. Under these conditions, the tendrils were produced in a consistent manner. Each shear-layer vortex "head" was attached to a pair of tendrils. It is this regime from which previous descriptions of tendrils have been derived (Figure 26, Figure 40). This regime existed generally for $Re_j > 360$ and $0.08 < R < 0.28$ up to a $Re_\infty \approx 1600$. For $Re_\infty > 1600$, this regime extended for Re_j as low as about 450. It may be speculated that this regime continues to higher cross-flow Reynolds number than were tested, as the tendrils are thought to be a feature of the regular-mixing-layer-type regime. Though not specifically identified by Huang and Lan, tendrils seem to appear in some flow visualization images by these authors.

The regular-tendril-formation regime could extend to slightly lower cross-flow Reynolds numbers; however not much lower than the tested values, according to the argument in section 6.3.1 that the Kelvin-Helmholtz instability will lose strength at lower Reynolds numbers, hence retarding the production of shear-layer vortices and, in turn, preventing tendril production.

The intermittent-tendril-formation regime, shown in Figure 59 and Figure 61, corresponds to higher cross-flow Reynolds numbers as well as a small band of jet Reynolds numbers between the pipe-end-vortex-suction and regular-tendril-formation regimes. The intermittent-tendril-formation regime had the appearance of being a transition between the pipe-end-vortex-suction and regular-tendril-formation regimes. A fraction of shear-layer vortices were sucked downward by the pipe-end vortex in a fashion similar to that in the pipe-end-vortex-suction regime; however, the remainder were stretched into a tendril pair as they would have been in the regular-tendril-formation regime. As mentioned previously, this regime was intermediate between the pipe-end-vortex-suction regime and the regular-tendril-formation regime, corresponding to momentum-flux ratios that are sufficiently large for the jet to overcome the suction of the low-pressure region on the lee side of the pipe. However, there was a region in this regime at the lowest tested momentum-flux ratios, at which the cross-flow Reynolds number was sufficiently high for the tendrils to be pulled downstream rather than being sucked down behind the pipe. The intermittent-tendril-formation regime is likely to extend to lower cross-flow Reynolds numbers, serving as a transition between the pipe-end-vortex-suction regime and the regular-tendril-formation regime.

The unsplit-shear-layer-vortex regime shown in Figure 59 corresponds to the highest

momentum-flux ratios tested in the present study. In this regime, the jet fluid had sufficient momentum to escape the pull of the low-pressure region behind the pipe. In consequence, the shear-layer vortices were not split and tendrils were not produced. This regime was thought to encompass all flows with momentum-flux ratios above those tested for both higher and lower cross-flow Reynolds numbers as these cases would approach the case of a free jet from a pipe for which there would be no low-pressure region as there would be no cross-flow. It appears in Figure 47, Figure 48, and Figure 49.

6.4.3 Frequency Variation

Not surprisingly, the relationship between the Strouhal number of the tendrils and the momentum-flux ratio was similar to that for the shear-layer vortices. The Strouhal number was calculated by counting each tendril pair as one occurrence similar to the calculation of the Strouhal number for von Kármán vortices. As the momentum-flux ratio increased, the Strouhal number decreased, as shown in Figure 62. The data could be fitted fairly well by a power-law type of function, as

$$St_d = 0.43 \cdot R^{-0.63}. \tag{21}$$

Note that the exponent in the fitted line is very close to that of the exponent for the shear-layer vortices; however, the coefficient is approximately half that of the coefficient for the shear-layer vortices. This is due to the fact that the cases which yielded frequency data were only those within the intermittent-tendril-formation regime, so that not every observed shear-layer vortex produced a pair of tendrils. For this reason, the results in Figure 62 should be used only for the purpose of identifying the trend and not for quantitative purposes. As

with the shear-layer vortices, Reynolds number was not observed to affect the Strouhal number of the tendrils.

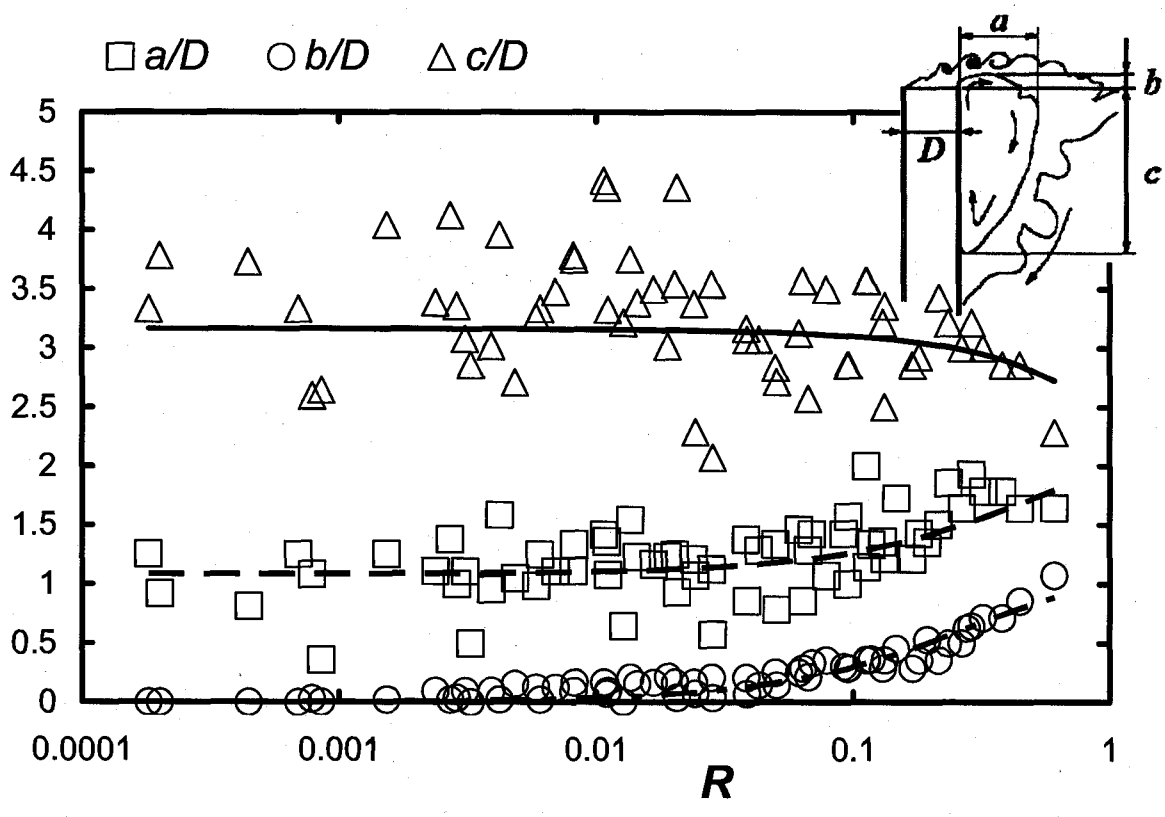

Figure 41 – Variation of pipe-end vortex size with rough curve fits for visual purposes (– – – equation 13, — — — equation 14, —— equation 15)

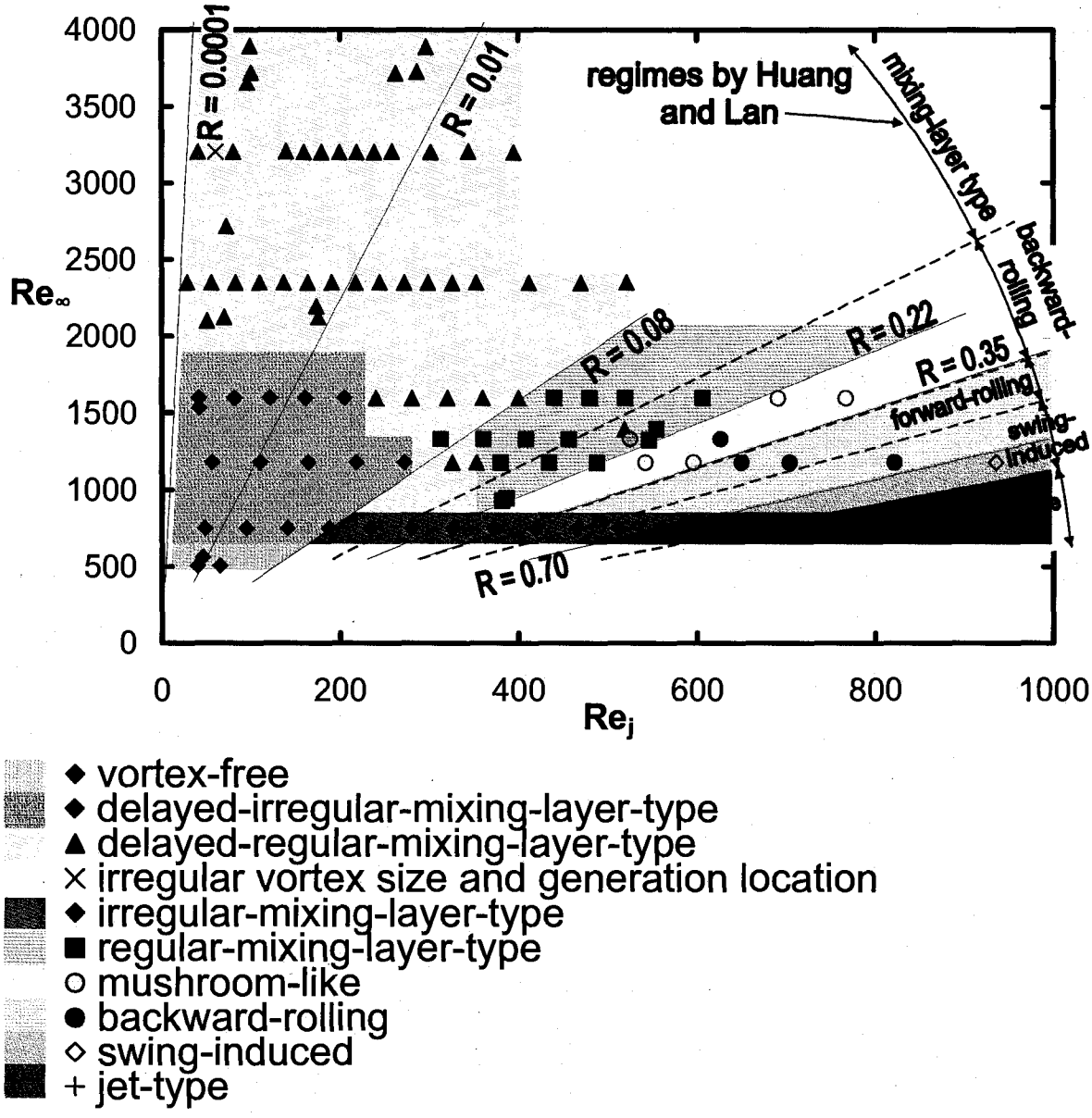

Figure 42 – Regime map for shear-layer vortices

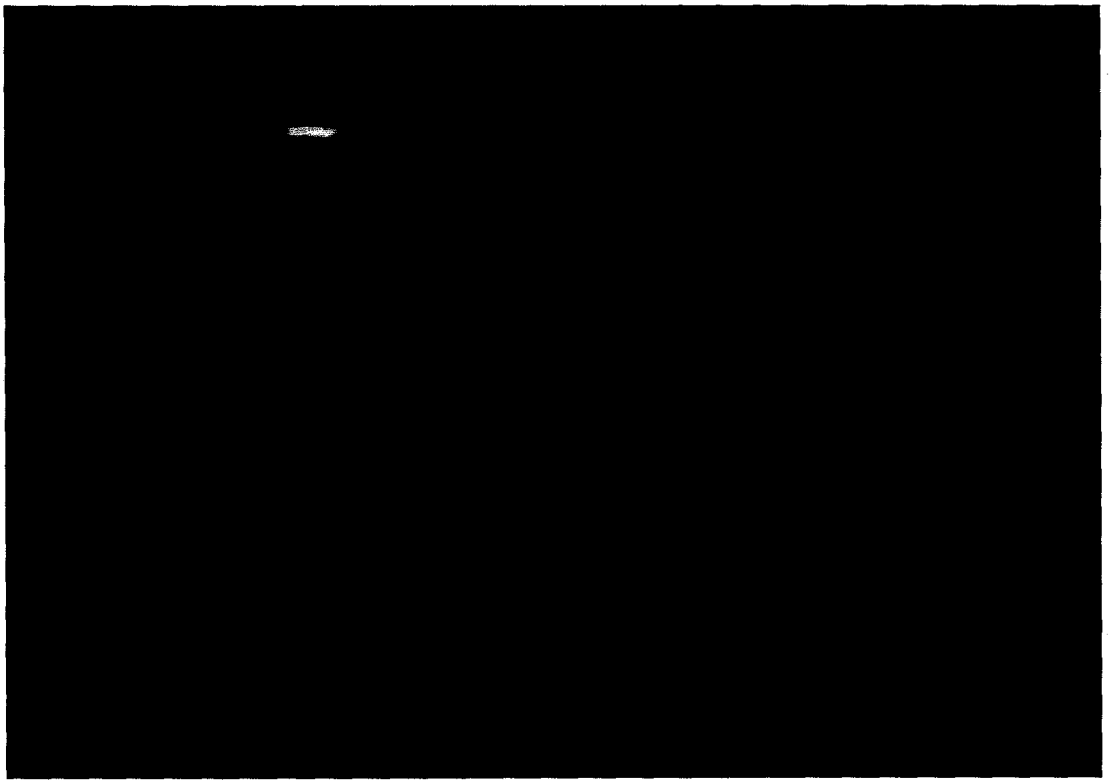

Figure 43 – Image of vortex-free regime (d = 12.95 mm, R = 0.0083, Re_j = 40, Re_∞ = 505)

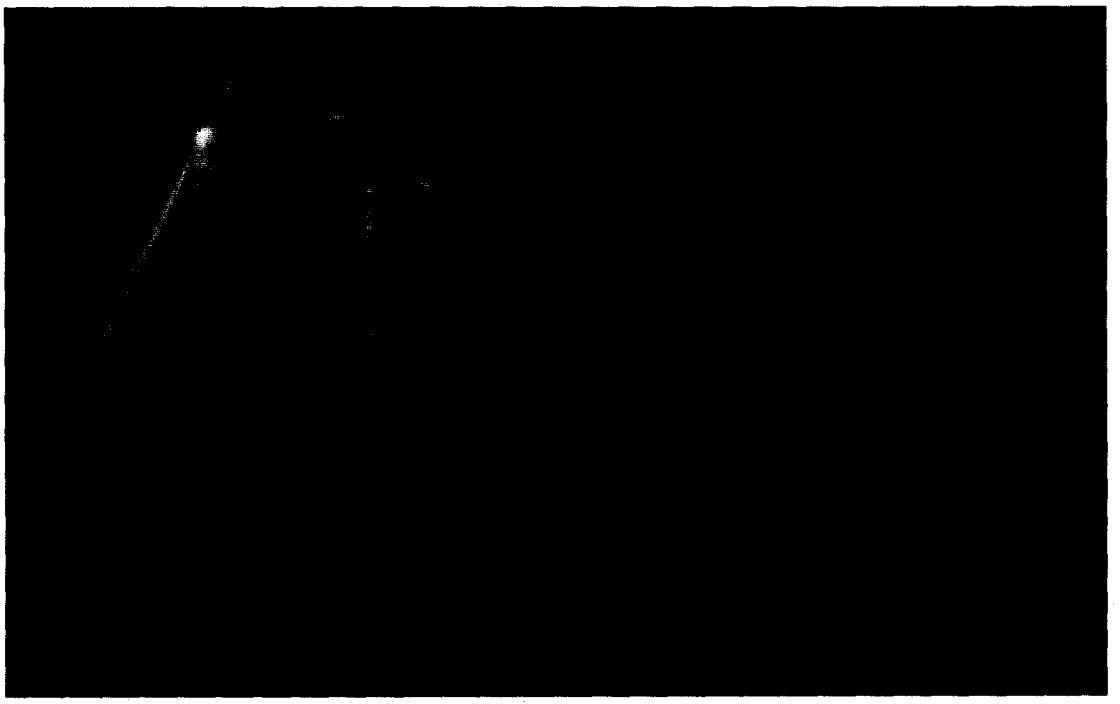

Figure 44 – Image of delayed-irregular-mixing-layer-type regime (d = 19.38 mm, R = 0.0009, Re_j = 42, Re_∞ = 1533)

Figure 45 – Image of delayed-regular-mixing-layer-type regime ($d = 22.55$ mm, $R = 0.050$, $Re_j = 469$, $Re_\infty = 2349$)

Figure 46 – Image of mushroom-like vortex regime ($d = 18.79$ mm, $R = 0.19$, $Re_j = 525$, $Re_\infty = 1330$)

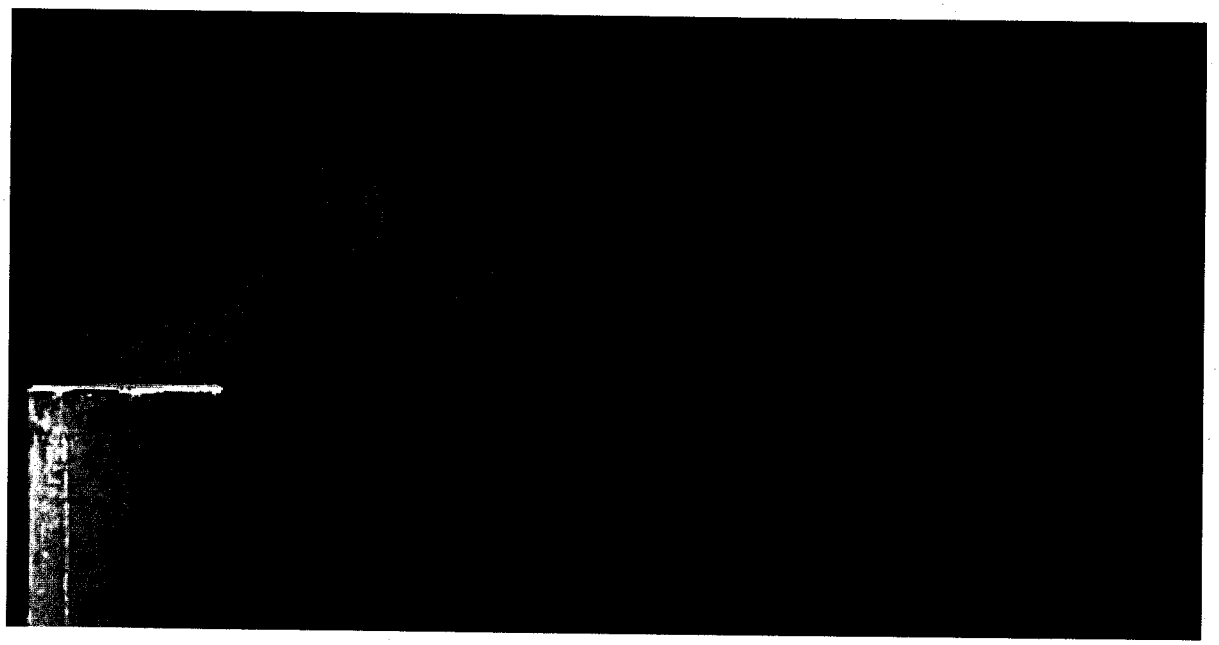

Figure 47 – Image of backward-rolling vortex regime ($d = 18.79$ mm, $R = 0.28$, $\mathrm{Re_j} = 626$, $\mathrm{Re_\infty} = 1330$)

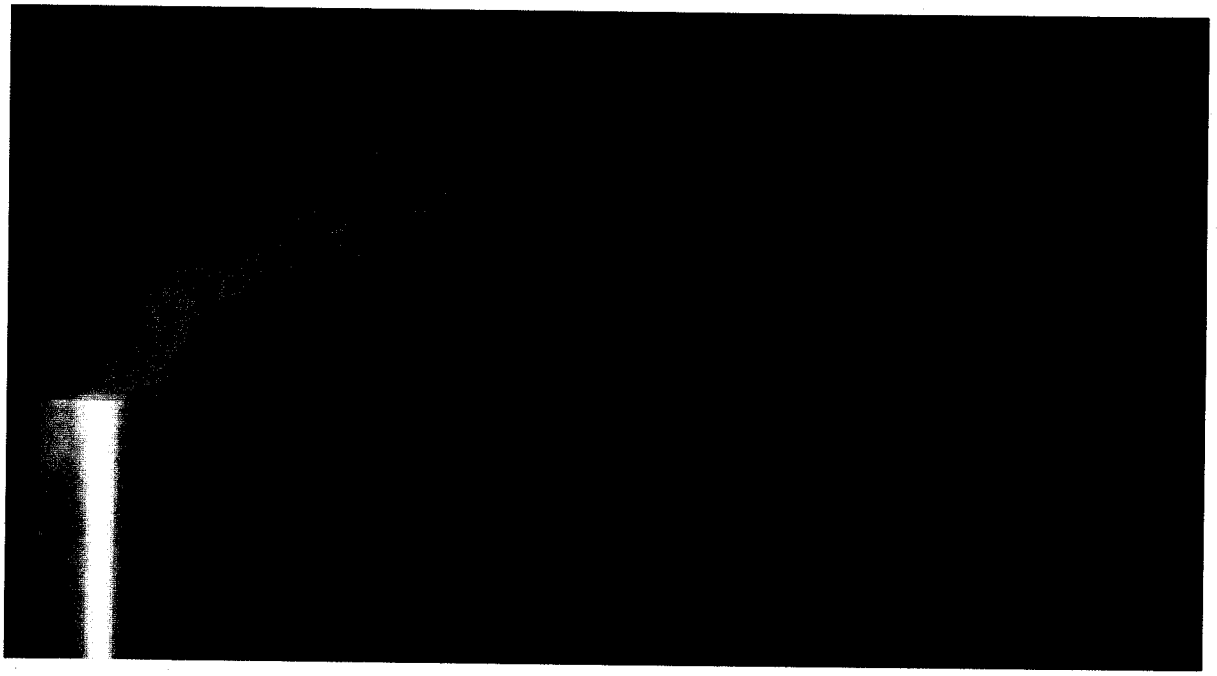

Figure 48 – Image of swing-induced vortex regime ($d = 16.64$ mm, $R = 0.79$, $\mathrm{Re_j} = 936$, $\mathrm{Re_\infty} = 1178$)

Figure 49 – Image of jet-type vortex regime ($d = 16.64$ mm, $R = 0.99$, $Re_j = 1051$, $Re_\infty = 1178$)

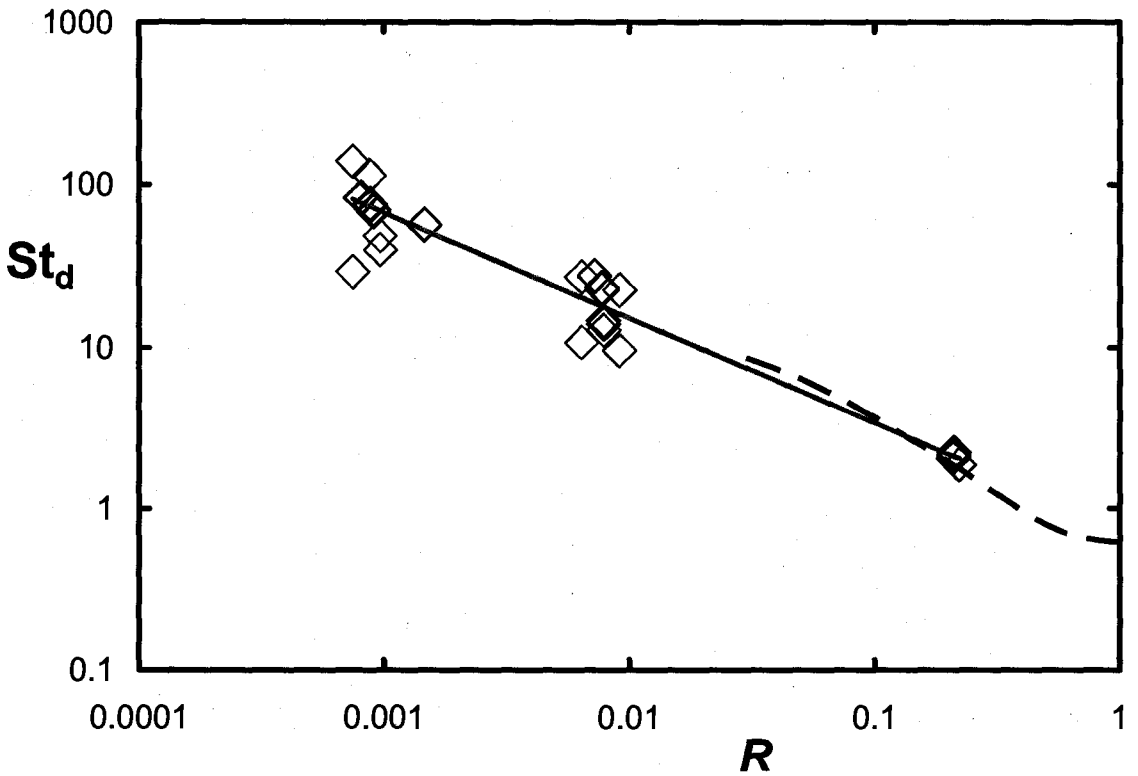

Figure 50 – Strouhal number versus momentum-flux ratio for shear-layer vortices; ◊ measurements from present study, — equation 16 fitted to the present data, - - - equation 17, fitted by Huang and Lan (2005) to their data

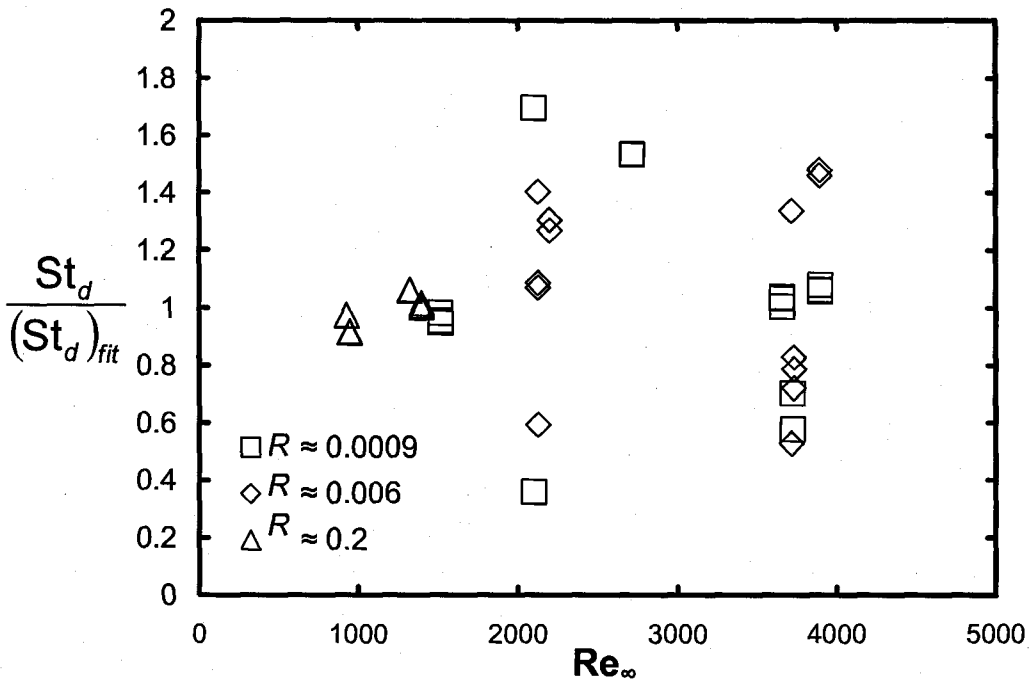

Figure 51 – Strouhal number versus cross-flow Reynolds number, for approximately constant values of the momentum-flux ratio; the values have been normalized by the value given by the fitted equation 16

Figure 52 – Frame from video sequence used for shear-layer vortex velocity measurement (d = 18.79 mm, R = 0.069, Re_j = 313, Re_∞ = 1330)

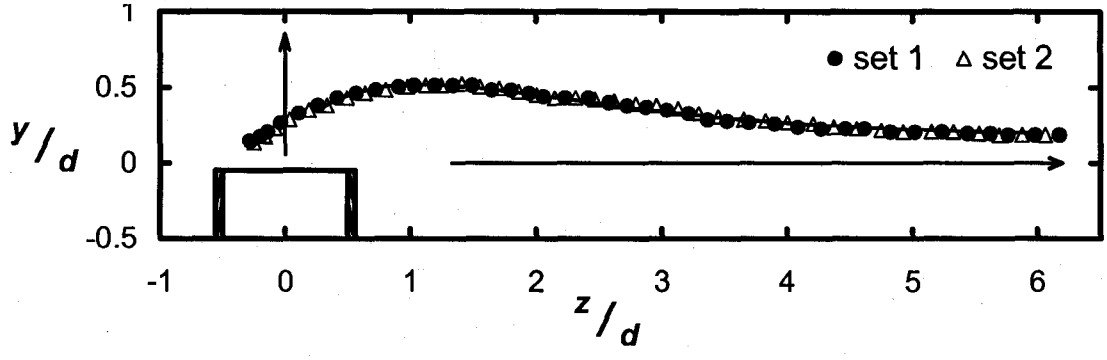

Figure 53 – Location of the axis of a single shear-layer vortex on the plane of symmetry, as it was convected downstream, — equation 18 (d = 18.79 mm, R = 0.069, Re_j = 313, Re_∞ = 1330)

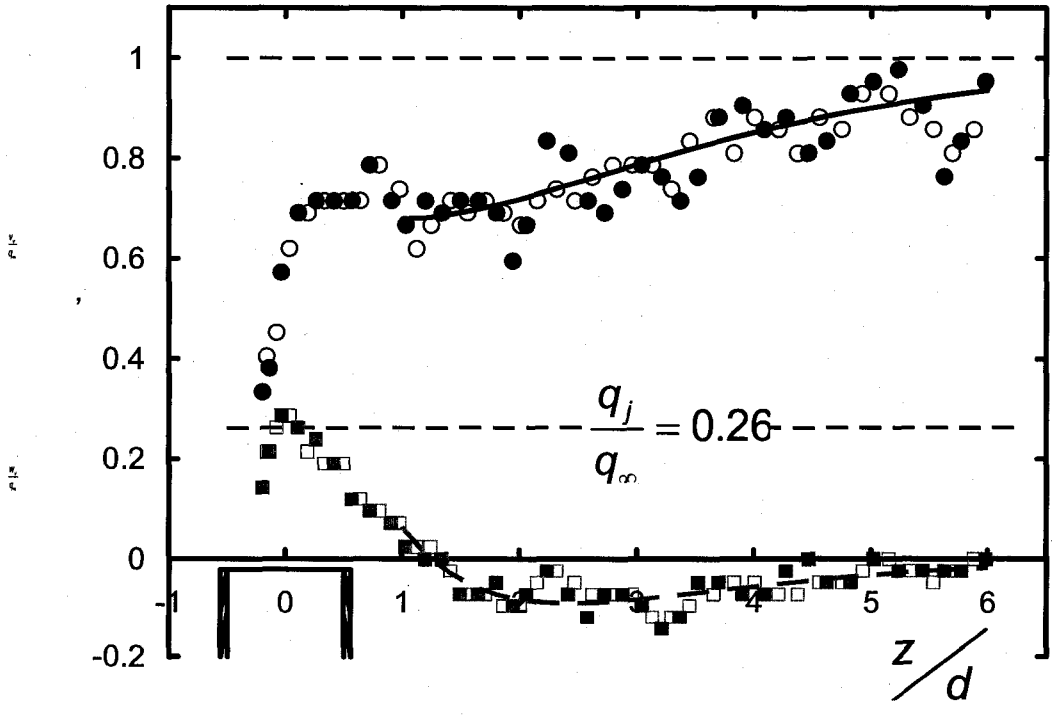

Figure 54 – Dimensionless velocity components of vortex axis, ■ – set 1 v_v, □ – set 2 v_v, ● – set 1 w_v, ○ – set 2 w_v, --- equation 19, — equation 20 (d = 18.79 mm, R = 0.069, Re_j = 313, Re_∞ = 1330)

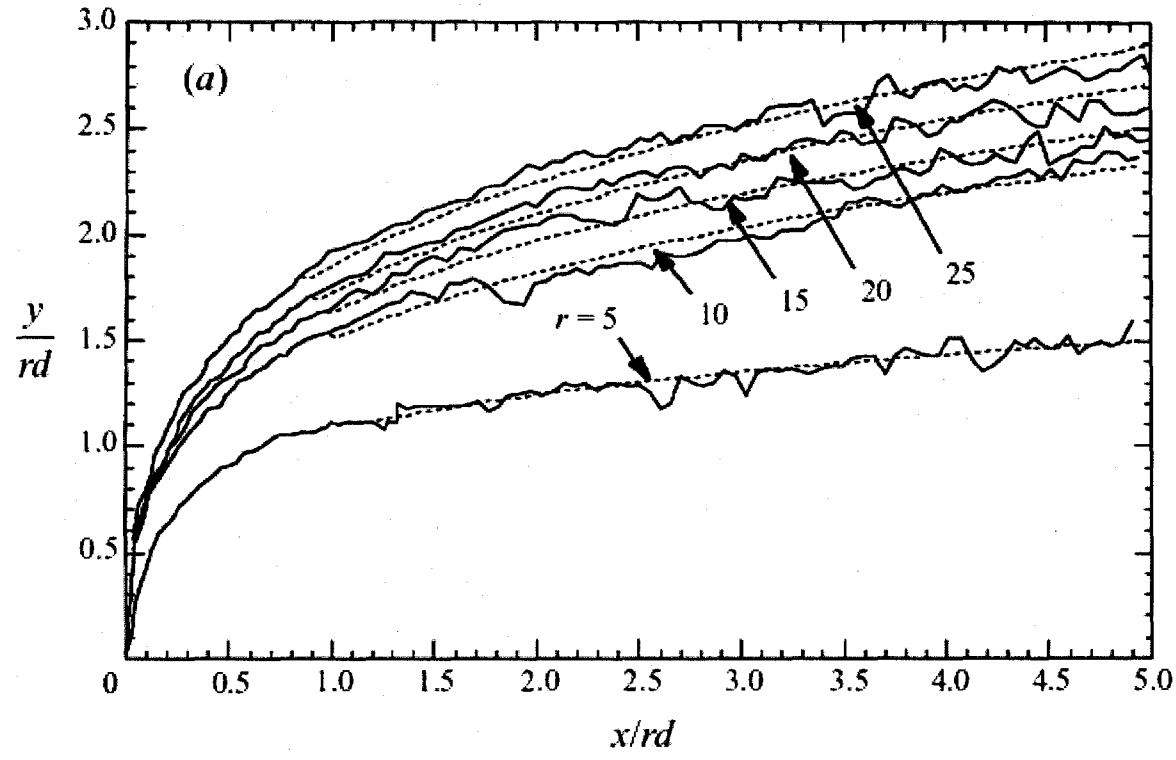

Figure 55 – Trajectory of jet centreline from a wall-issued jet in a cross-flow from Smith and Mungal (1998) (r is the velocity ratio, $R = r^2$ due to neutral density

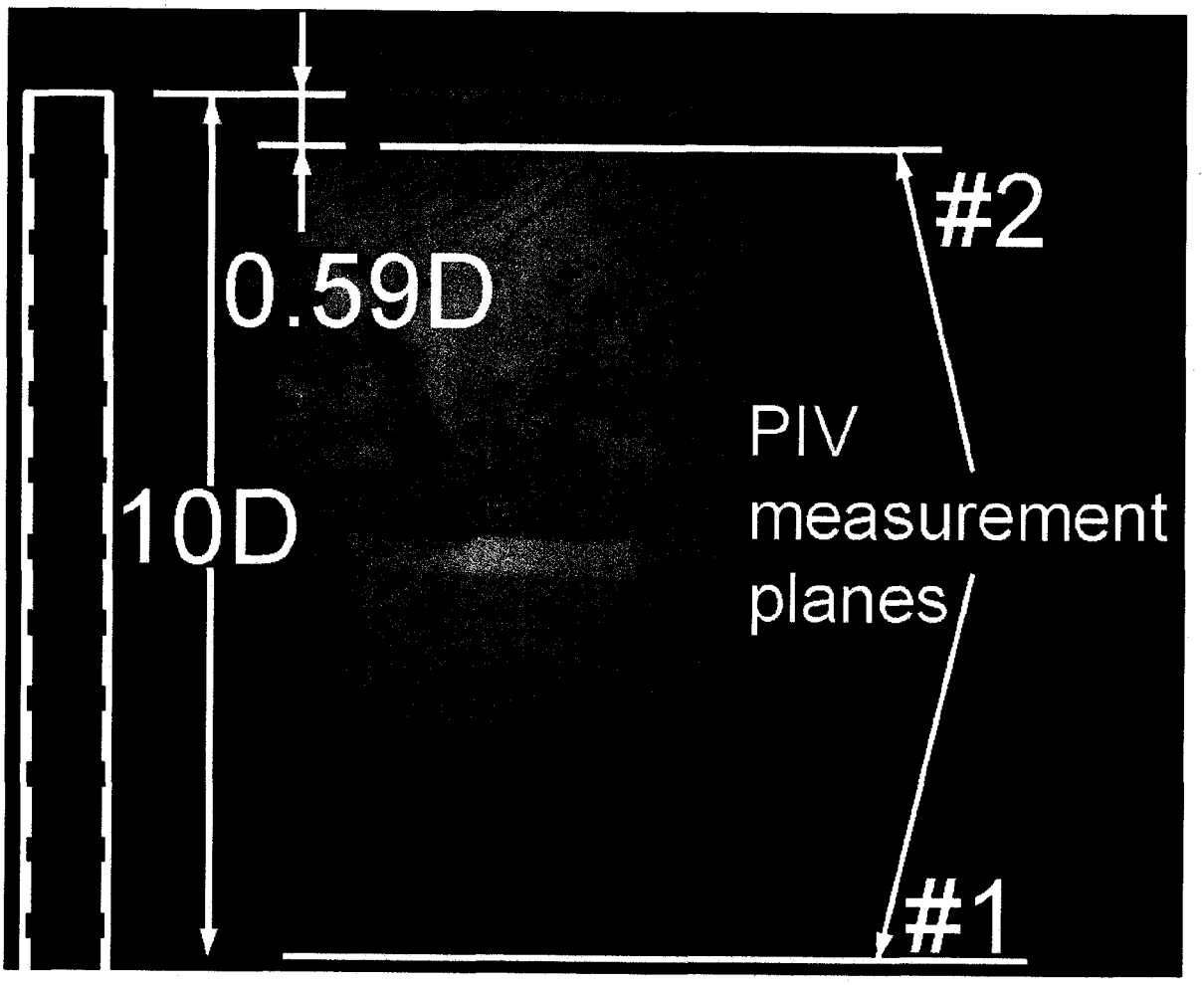

Figure 56 – Sketch showing measurement plane locations of PIV measurements (d = 19.38 mm, R = 0.076, Re_j = 327, Re_∞ = 1330)

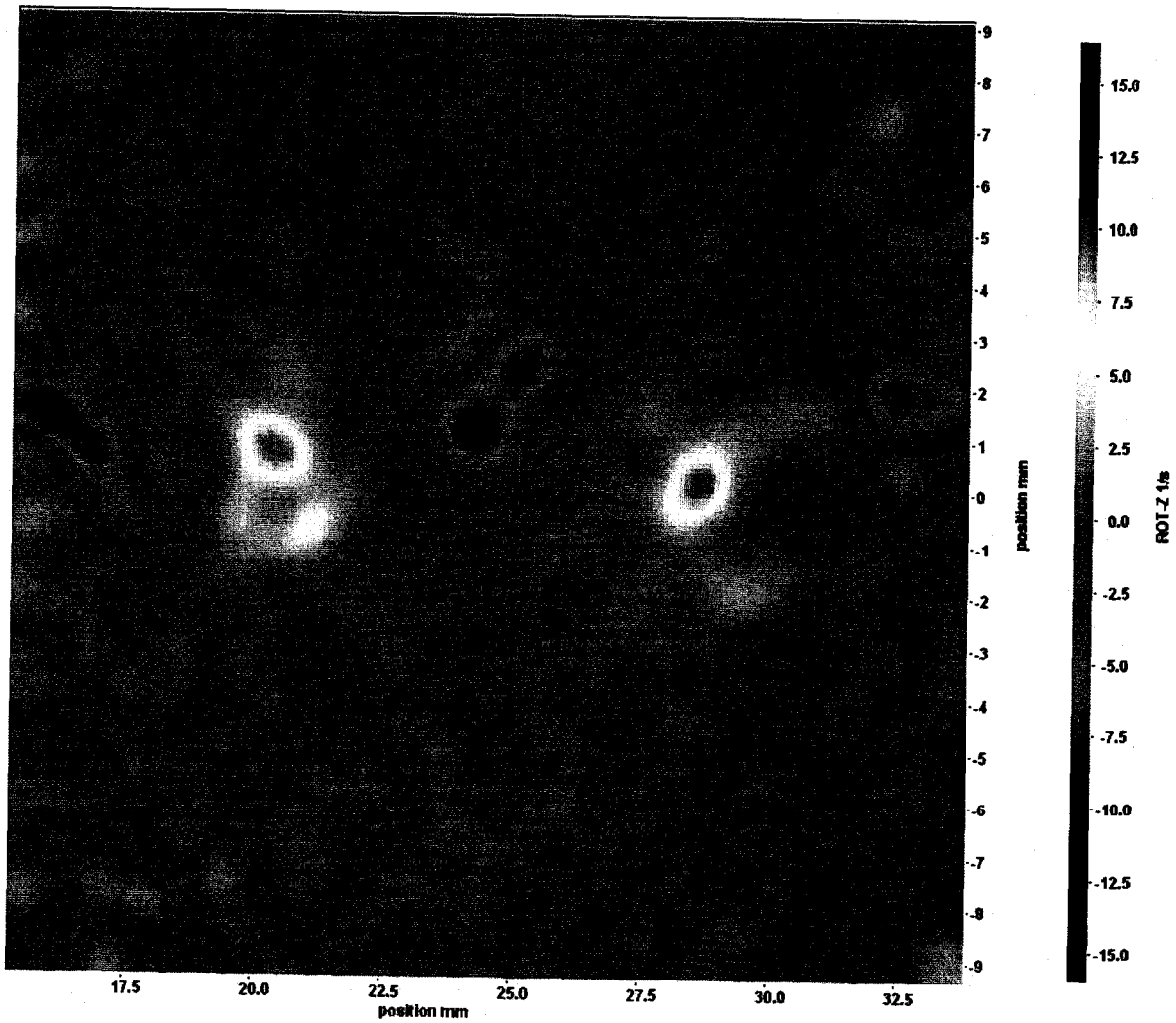

Figure 57 – Vorticity field from PIV measurement at location #1 (d = 19.38 mm, R = 0.076, Re_j = 327, Re_∞ = 1330, pipe axis at origin)

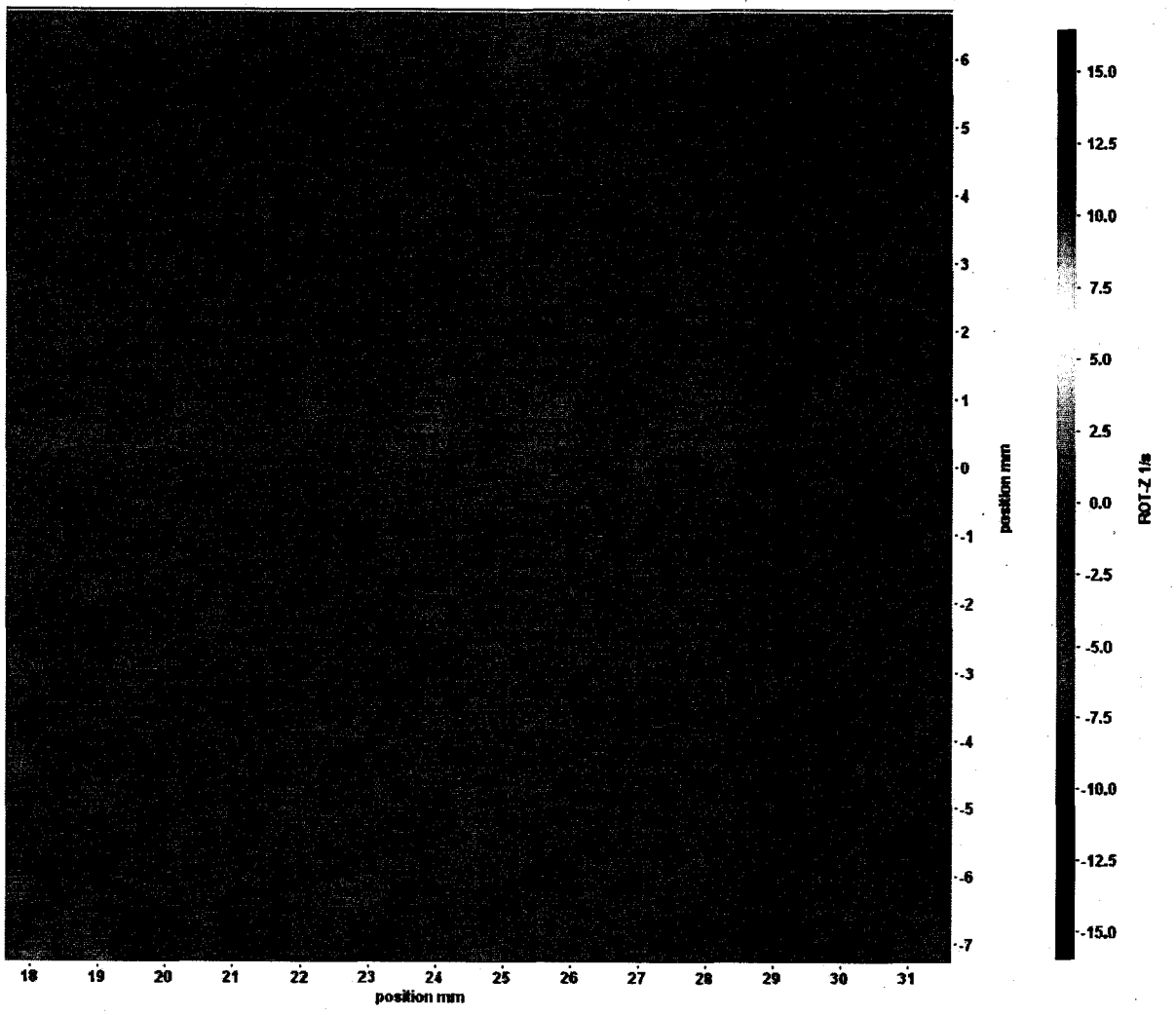

Figure 58 – Vorticity field from PIV measurement at location #2 (d = 19.38 mm, R = 0.076, Re_j = 327, Re_∞ = 1330, pipe axis at origin)

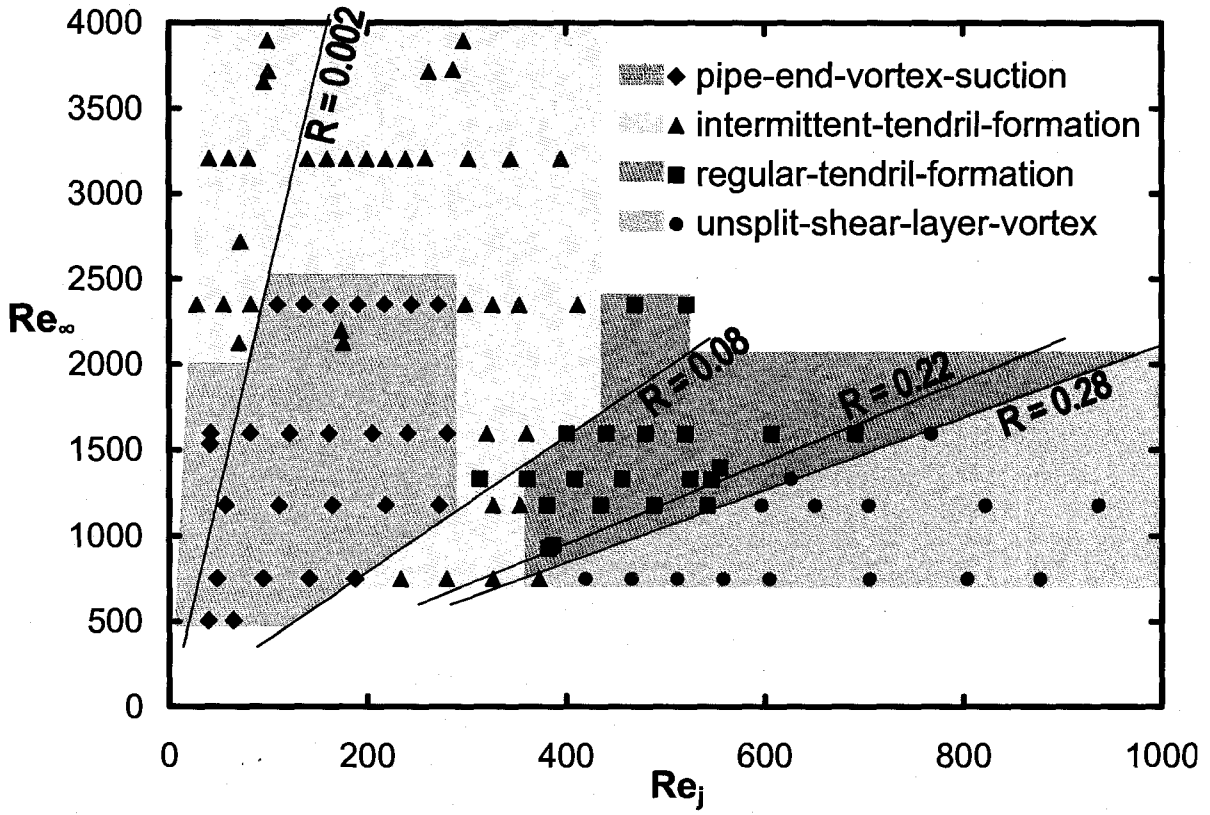

Figure 59 – Regime map for tendrils

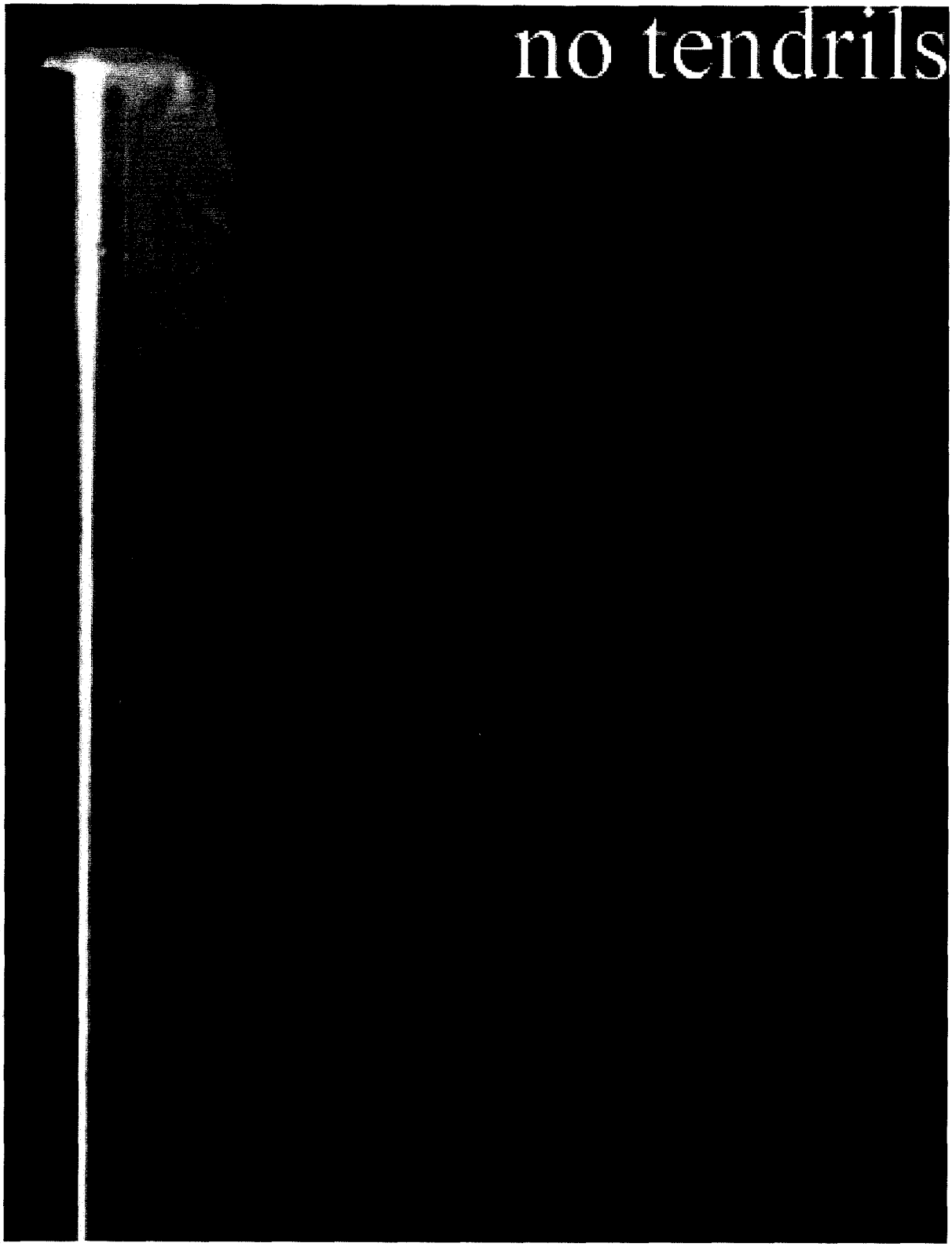

Figure 60 – Image of pipe-end-vortex-suction tendril regime ($d = 22.55$ mm, $R = 0.007$, $Re_j = 121$, $Re_\infty = 1596$)

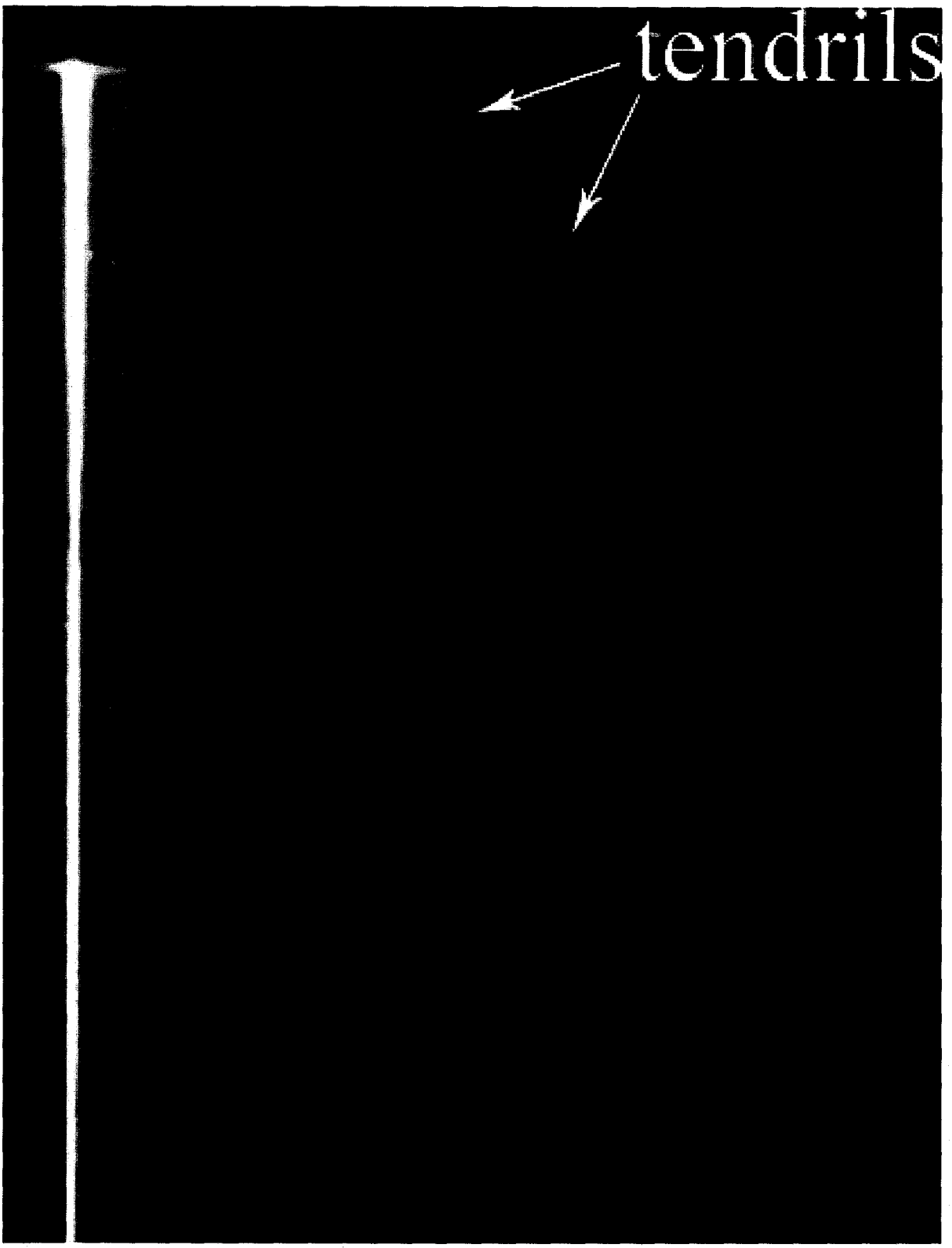

Figure 61 – Image of intermittent-tendril-formation regime ($d = 22.55$ mm, $R = 0.050$, $Re_j = 320$, $Re_\infty = 1596$)

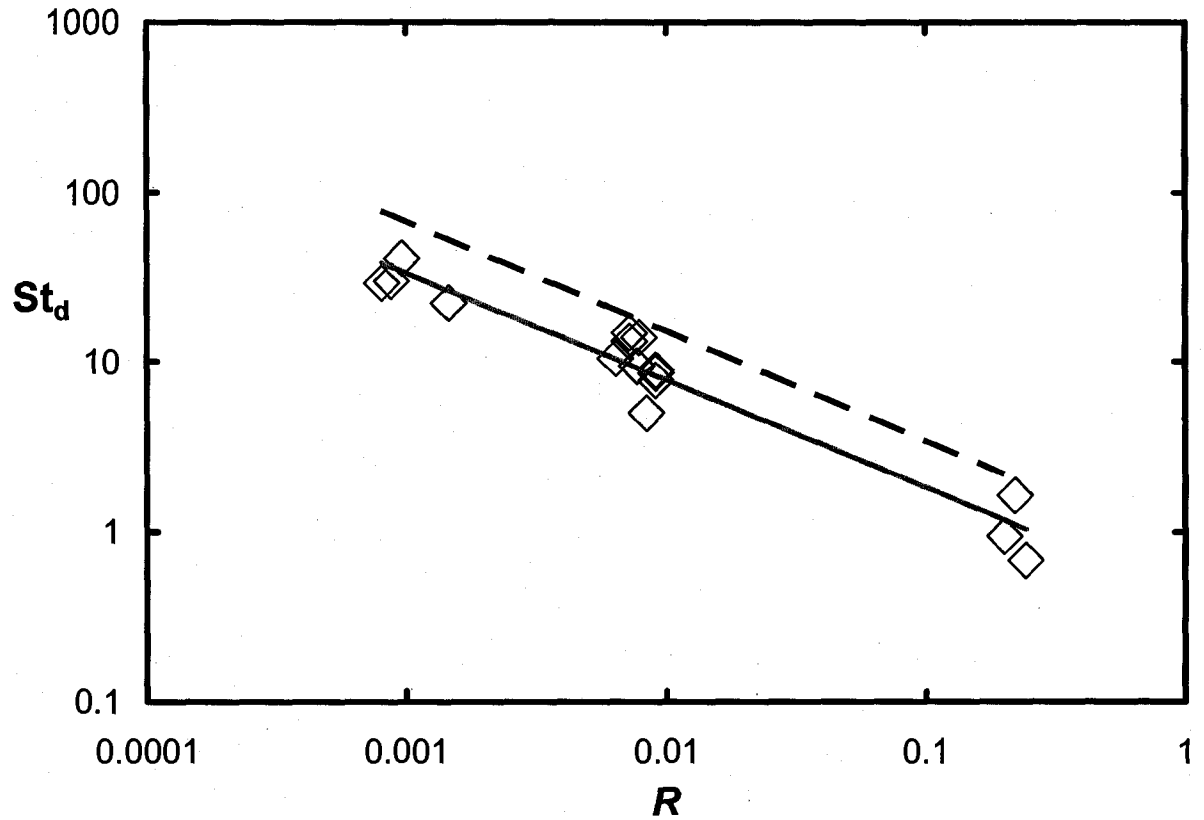

Figure 62 – Strouhal number versus momentum-flux ratio for tendrils, —— equation 21, fitted to the present data, - - - equation 16, fitted to the shear-layer vortices

Chapter 7 Discussion

7.1 Pipe-End Vortex

Under stationary flow conditions, the total vorticity contained in the pipe-end vortex would remain essentially constant. Vorticity is convected into the vortex by the entrainment of the jet fluid, which contains the vorticity originating in the interior of the pipe flow as well as additional amounts as discussed in 5.2.3. Additionally, vorticity is also generated within the pipe-end vortex on the downstream end of the pipe. The jet fluid travelling downward along the downstream end of the pipe-end vortex impinges upon the pipe below the pipe-end vortex and hence creates a stagnation point. From this point, the jet fluid flows either downward along the pipe or upward into the pipe-end vortex. This pressure gradient, from higher at the stagnation point to lower within the vortex, is responsible for generating the vorticity found in the boundary layer on the lee-side of the pipe as pictured in Figure 63. This vorticity had vortex lines circumferentially along the downstream extreme of the pipe as supported by Rosenhead (1963, p. 46-60) in his discussion pertaining to vortex lines running perpendicular to the flow direction of a boundary layer on a surface. The vorticity generated in this manner has an opposite sign to that generated on the interior of the pipe that is pulled into the pipe-end vortex. Vorticity is lost by convection from the sides of the vortex to the cross-flow fluid travelling around the pipe and from the lower part of the vortex, downwards

along the lee-side of the pipe. Some vorticity is lost by cross-diffusive annihilation of vorticity of opposite senses (i.e., that which is generated in the pipe and that which is generated within the pipe-end vortex) as discussed by Morton (1984), and some additional amount could be lost by diffusion to the surroundings, although these amounts are difficult to estimate. These mechanisms have been illustrated in Figure 63. The sign of the vorticity generated by the cross-flow on the upstream exterior surface of the pipe as well as that generated on the downstream interior of the pipe-flow match the large-scale turning sense of the pipe-end vortex, making the integration of the vorticity from these two sources into the pipe-end vortex feasible.

7.2 Shear-Layer Vortices

As mentioned in Chapter 5, there are two sources of vorticity for these coherent structures: the vorticity generated within the boundary layer in the interior of the pipe and that generated by acceleration of the cross-flow on the upstream side of the pipe exterior and on the upstream end of the rim of the pipe. These two sources generate vorticity in opposing directions on the plane of symmetry. This difference in sign can assist in explaining the evolution of the shear-layer vortices.

Flows at the lowest Reynolds numbers tested, and at momentum-flux ratios around 0.01, were within the vortex-free regime, in which no shear-layer vortices were observed to exist. One is reminded that it is not the velocity ratio across a mixing layer (i.e., the square root of R in the present type of flows) that determines the stability of the mixing layer, but

the velocity difference across it (i.e., the difference between the jet fluid velocity and the cross-flow velocity). At sufficiently low Reynolds numbers, this velocity difference would be sufficiently small, irrespectively of the value of the momentum-flux ratio, for the mixing layer to be stable (Panton, 2005, p. 679). Conversely, at higher Reynolds numbers, even flows with momentum-flux ratios two orders of magnitude lower than the previous case would have a sufficiently large velocity difference across the interface for the mixing layer to be unstable and the Kelvin-Helmholtz instability mechanism to become active. This explains why the delayed-irregular-mixing-layer-type and delayed-regular-mixing-layer-type regimes existed at lower momentum-flux ratios than the vortex-free regime.

At the lower momentum-flux ratios tested, any shear-layer vortices that formed rolled in a 'forward' direction, namely, in a sense which would be caused by the cross-flow turning over the pipe tip. In the presently chosen orientation of the images, this rolling on the symmetry plane would be viewed as clockwise. The total vorticity generation rate in the interior of the relatively slow pipe-flow would have been much lower than that at a relatively high Reynolds number. One may speculate that, if one held the cross-flow Reynolds number constant at a value between 1100 and 1600 and raised the jet Reynolds number, hence increasing the momentum-flux ratio and reducing the velocity difference, the flow would become more stable. This hypothesis was confirmed by the present observations that vortices were generated at more regular rates and sizes as the jet Reynolds number was increased within this range.

As the jet Reynolds number further increased, the radial velocity gradient in the pipe increased, which corresponds to a flow with a higher level of vorticity coming out of the

pipe. The vorticity contained in the jet at the lower tested momentum-flux ratio flows would be significantly weaker than the vorticity with the opposite sign generated along the upstream outer surface of the pipe near its tip. An increase in jet-fluid velocity brought an increase in the convection velocity of the shear-layer vortices. This increase of convection velocity as well as the increased vorticity generation from the interior of the pipe became evident in the form of vortices turning in the opposite direction of the mixing-layer-type vortices at the onset of the mushroom-like regime. A further increase in the jet Reynolds number further increased the vorticity originating from the interior of the pipe which eventually over-powered the opposing vorticity from the outer surface of the pipe, marking the backward-rolling regime. At higher jet-Reynolds numbers yet again, the velocity difference at the mixing-layer between the jet and cross-flow fluids became small enough for the shear-layer vortices to become weaker as the flow became more stable in the swing-induced regime. A nearly stable exit was observed when the momentum-flux ratio approached unity, removing the velocity difference and hence the presence of the mixing layer. For yet higher values of the momentum-flux ratio, jet vorticity dominated, and the vortices at the interface of the jet and the cross-flow were of the jet type.

7.3 Tendrils

In this uniform density flow, the only mechanism available for vorticity production were pressure gradients along the boundary layers around the inner and outer pipe surfaces. This implies that, as the tendrils formed downstream of the pipe-end vortex and hence away from the pipe, no vorticity was generated for these structures after they were formed from the

shear-layer vortices. The solenoidality condition of vorticity shown in equation 10 states that the amount of vorticity contained in the cross-sectional area of an "elementary vortex tube" as stated by Rosenhead (1963, p. 50) does not vary. Considering the dyed fluid contained within the visible portion of the shear-layer vortices to be within a vortex tube, when this tube is stretched into a narrower cross-section as it does when the tendrils are formed, the vorticity along these tubes must increase.

As these structures stretched, equation 3 dictates that the vorticity would have intensified. The counter-rotating property of the tendril pairs has the potential to create self-induced motion, as each branch would exercise a force on the other. This self-induced motion has the potential to combine with the previously mentioned mechanism for tendrils changing their initial inclination toward the base of the pipe-end vortex, therefore intensifying this effect. As the tendrils convect further downstream, it was observed that the inclination actually changes beyond a vertical orientation to an inclination such that the tendril lower parts began to lead their tops.

As vortex lines cannot terminate within a fluid, the tendrils must tie into other structures farther downstream. Mechanisms for this were mentioned previously in section 5.4.4. The potential link between tendrils and the von Kármán vortices requires additional experimentation as this is potentially a strong mechanism for funnelling jet fluid in high concentrations downward, toward the "ground". As mentioned in Chapter 1, Johnson et al. (2001) previously observed what they referred to as "fuel stripping" where highly flammable and lighter-than-air methane travelled through an open flame in a downward direction and remained unburned. The tendrils linking up with the von Kármán vortices is potentially the

mechanism that kept the methane at sufficiently high concentrations such that it did not meet stoichiometric ratios and was sufficiently strong to overcome the buoyancy force that the methane would have had in air.

7.4 Shear-Layer Vortex and Tendril Regime Map Comparison

A comparison of the regime maps of the shear-layer vortices and the tendrils found in Figure 42 and Figure 59, respectively, shows that their appearances are similar. Though the boundaries in the two figures do not exactly coincide, rough correspondence can be recognized between regimes of the respective coherent structures. In general, the vortex-free and delayed-irregular-mixing-layer-type regimes on the shear-layer vortex map correspond to the pipe-end-vortex-suction regime on the tendril map, the regular-mixing-layer-type regime corresponds to the regular-tendril-formation regime, and all higher momentum-flux ratio shear-layer vortex regimes correspond to the unsplit-shear-layer-vortex regime.

The vortex-free and the delayed-irregular-mixing-layer-type regimes of the shear-layer vortices fit entirely within the conditions of the pipe-end-vortex-suction regime of the tendrils.

Above a cross-flow Reynolds number of approximately 2500, the delayed-regular-mixing-layer-type regime and the intermittent-tendril-formation regime prevailed for the tested conditions. Below this value and above the upper limit of the delayed-irregular-

mixing-layer-type regime at $Re_\infty \approx 2000$, the shear-layer vortices remained in the delayed-regular-mixing-layer-type regime, but the tendril regime depended upon the jet Reynolds number. Below a jet Reynolds number of approximately 100, as well as between approximately 280 and 440, the intermittent-tendril-formation regime prevailed; however, in the range $100 < Re_j < 280$, the pipe-end-vortex-suction regime prevailed.

In a test case for which the cross-flow Reynolds number was held constant at 2350 and the jet Reynolds number was incrementally increased from 28 to 521, a peculiar phenomenon was observed: the tendrils began in the intermittent-tendril-formation regime, evolved into the pipe-end-vortex-suction regime, then converted back into the intermittent-tendril-formation regime before moving to the regular-tendril-formation regime. This shift seems to be a change in character of the shear-layer vortices. Though each case fits within the delayed-regular-mixing-layer-type regime, the size of the vortices and the downstream location at which they were generated seemed to vary. The larger shear-layer vortices generated at lower momentum-flux ratios persisted and occasionally developed into tendrils. None of the vortices at slightly higher momentum-flux ratios, which were slightly smaller in size, resulted in tendrils. Consistent with other flow conditions, when the jet Reynolds number exceeded approximately 280, some of the shear-layer vortices developed into tendrils.

Between jet Reynolds numbers of approximately 280 and 360 and up to 420 for momentum-flux ratios below 0.08, both the delayed-regular-mixing-layer-type regime and the intermittent-tendril-formation regime prevailed. These two regimes seemed to represent transitions between flows with lower and higher jet Reynolds numbers.

The upper extreme momentum-flux ratio value of the regular-tendril-formation regime was $R \approx 0.28$, which was only slightly higher than the upper R limit of the regular-mixing-layer-type regime. Tendrils were produced at the onset of the mushroom-like vortex regime, but not at higher momentum-flux ratios. As previously mentioned, all higher momentum-flux ratio shear-layer regimes lay within the unsplit-shear-layer-vortex regime.

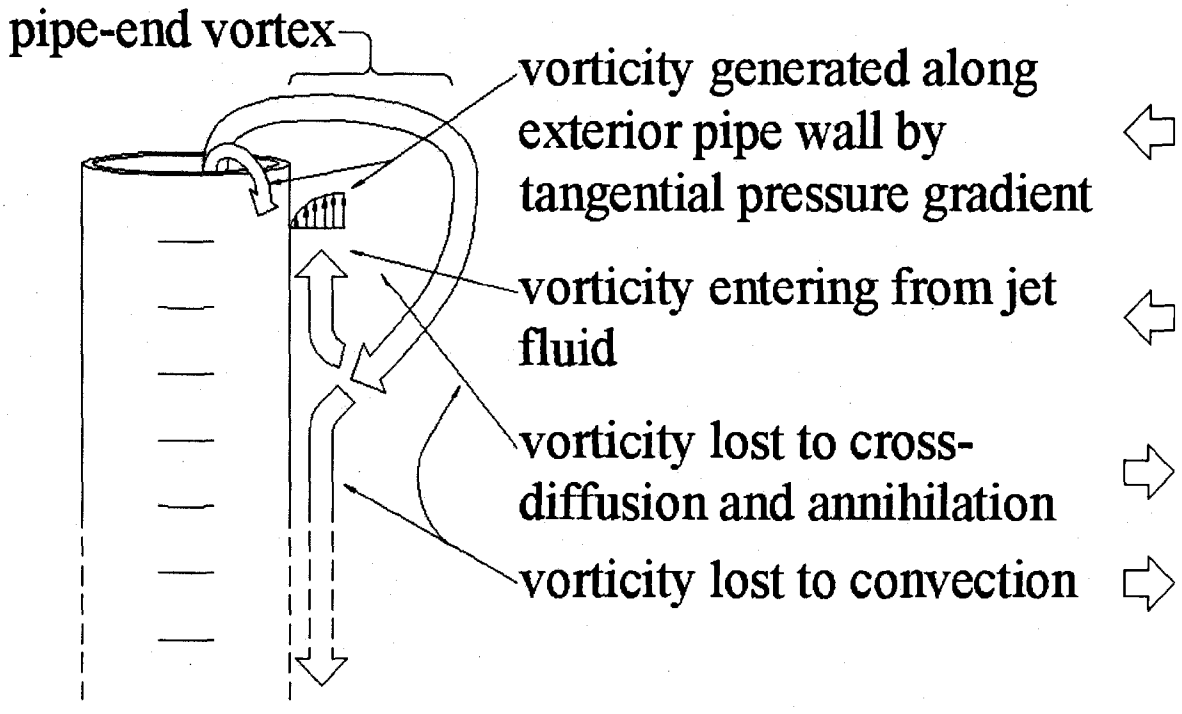

Figure 63 – Vorticity balance for pipe-end vortex

Chapter 8 Conclusions and Recommendations for Future Work

8.1 Conclusions

The objective of the present study was to document the large-scale structure of an elevated jet in a cross-flow, focusing on the low momentum-flux ratio range, which has received little attention in previous studies. Four major types of coherent structures were observed in this flow: von Kármán vortices, a stationary pipe-end vortex, shear-layer vortices and tendrils. The von Kármán vortices were similar to those found in the wakes of previous studies on finite cylinders with a free end in the flow. The pipe-end vortex is unique to the low-momentum elevated-jet in a cross-flow, as it is caused by the jet fluid being pulled into the low-pressure region behind the pipe-end and adding some of its vorticity to this coherent structure. The behaviour of the shear-layer vortices changed significantly within the tested conditions, but they were generally similar to those which would be expected from a Kelvin-Helmholtz shear-layer instability. Generally, the tendrils were thin structures that appeared in counter-rotating pairs. No previous research is available pertaining to tendrils aside from a brief mention in one paper. They were products of the shear-layer vortices and their properties depended on flow conditions.

Within the tested conditions, the von Kármán vortices did not significantly change

character. Their inclinations changed through their travel in all observed flow conditions. After being shed from the pipe, their upper portion became inclined toward the base of the pipe-end vortex. As they became convected downstream, this inclination changed in a manner opposite to that previously observed behind finite cylinders with a free-end in a flow.

The pipe-end vortex had a complex inner structure, although this was only documented roughly on a plane perpendicular to the pipe-axis. The dimensions of the pipe-end vortex on the plane of symmetry were measured and were found to depend on the momentum-flux ratio once it exceeded approximately 0.01. The Reynolds number did not seem to have a strong effect on the measured pipe-end vortex dimensions within the tested conditions. A model for the internal structure of this vortex was proposed, which was compatible with the available observations.

The shear-layer vortices were categorized into eight regimes which were mapped according to their Reynolds numbers and momentum-flux ratios. Three of these regimes were at momentum-flux ratios that were lower than previously documented. The remaining five had momentum-flux ratios in the ranges previously examined by other researchers; however, the present study used lower Reynolds numbers which is thought to be responsible for the regimes appearing at different momentum-flux ratios than previously documented. The tendrils were divided into four regimes and were mapped in a manner similar to that used for the shear-layer vortices.

The Strouhal number of the shear-layer vortices was calculated for a range of flow conditions. It was found to be insensitive to Reynolds number and had a power-law-type dependence on the momentum-flux ratio. At the higher momentum-flux ratios tested, the

curve to the data from the present study corresponded well with an exponential function proposed by another researcher. Similarly, the Strouhal number of the tendrils was also plotted versus the momentum-flux ratio and had a trend similar to that of the shear-layer vortices.

The convection velocity of a shear-layer vortex core was calculated over its travel from its location of generation to approximately six diameters downstream of the pipe axis for a representative set of flow conditions. Strong acceleration was found in both the streamwise and spanwise directions immediately after generation, after which the spanwise velocity dropped off, became negative, then slowly approached zero as the shear-layer vortex travelled downward after the pipe-end vortex, then levelled off approaching the streamwise direction. The streamwise velocity had a slight plateau and a slight lowering prior to slowly increasing toward the free-stream velocity.

Mechanisms were proposed for the origin and evolution of the different types of coherent structures. As discussed by many previous researchers, the source of vorticity for the von Kármán vortices is the boundary layer on the sides of the pipe. The pipe-end vortex acquires its vorticity from the shear-layer vortices as well as the small boundary layer that develops on the outer, lee surface of the pipe near its end. The shear-layer vortices have two sources of vorticity, that from the fully developed jet fluid exiting the pipe as well as that from the cross-flow fluid flowing upward along the outer pipe surface on its upstream end. The tendrils receive their vorticity from the shear-layer vortices as they are stretched and the vorticity is intensified.

As the various vortex types evolve, numerous possibilities exist for the interactions between the vortices. As the pipe-end vortex is a stationary vortex of a consistent size for a given flow condition and was observed to be gaining vorticity, it must also lose vorticity. Vorticity escaped down the pipe along the lee surface and though not directly observed, it also would have lost vorticity to convection through its sides to the cross-flow. Cross-diffusion of vorticity with opposite directions would also have occurred within the vortex. The vorticity from the shear-layer vortices was passed along to the tendrils as well as being pulled into the pipe-end vortex. As the tendrils and the von Kármán vortices became convected downstream, their vortex lines leading back to the pipe would not have been able to do so indefinitely. A few mechanisms are proposed for the evolution of these vortices including linking up to each other, in manners similar to those by which von Kármán vortices in cellular vortex shedding link across cellular boundaries.

8.2 Recommendations for Future Work

The following direct extensions of the present work could be investigated to clarify some issues that were insufficiently examined in the present study:

- There are several areas in the regime maps for both the shear-layer vortices and the tendrils that could be filled with additional data points. Specifically, within the bounds of the present experimental set-up, if the cross-flow Reynolds number were set at 750 and the jet was cycled through its range, a few questions would be answered as to which regimes prevail between the

vortex-free regime and the lower extent of the other shear-layer vortex regimes.

- Though qualitative observations have narrowed down the possibilities that exist for downstream evolution of the tendrils, a quantitative study could make more firm conclusions. For a representative set of conditions, particle image velocimetry measurements could be taken along various planes perpendicular to the pipe axis, several diameters downstream of the pipe. Lower planes should exclusively show von Kármán vortices and an upper plane would reveal the smaller tendrils assuming sufficient sensitivity of the measurement system. This test would hopefully answer the question whether there is a link between the von Kármán vortices and the tendrils under these flow conditions.

- To investigate the ability of the tendrils to funnel jet fluid downward, a barrier could be placed at the pipe-end and observations made about the path of the jet fluid.

In addition, a few fundamental questions raised by the present work deserve further attention:

- The mechanisms that determine the location where the shear-layer vortices are generated remain obscure. In shear-layer vortex regimes associated with lower jet Reynolds numbers, the shear-layer vortices do not form directly at the pipe tip like the flows at higher jet Reynolds number or higher

momentum-flux ratio. Parallels can likely be drawn between the stability of these flows and those of a free jet.

- The Strouhal number of the shear-layer vortices was found to depend upon the momentum-flux ratio and to be insensitive to the Reynolds number. Further investigation into the mechanisms of the Kelvin-Helmholtz instability could reveal the mechanisms that are responsible for the variation of the Strouhal number.

- The shear-layer vortices are generated at irregular frequencies within a given flow range case within the delayed-irregular-mixing-layer-type vortex regime. Further study could reveal whether this is a flow stability issue or where there is another interaction taking place in this regime not revealed by the present study.

References

Andreopoulos, J. 1985 On the structure of jets in a cross-flow. *J. Fluid Mech.* **157,** 163-197.

Batchelor, G. K. 1967 *An Introduction to Fluid Dynamics.* Cambridge University Press. New York, N.Y.

Briggs, G. A. 1969 Plume rise. *U. S. A. E. C Crit. Rev. Series* **TID-25075,** 1-81.

Camussi, R., Guj, G. and Stella, A. 2002 Experimental study of a jet in a crossflow at very low Reynolds number. *J. Fluid Mech.* **454,** 113-144.

Canepa, E. 2004 An overview about the study of downwash effects on dispersion of airborne pollutants. *Environ. Modell. Softw.* **19,** 1077-1087.

Cowdrey, C. F. 1962 A note on the use of end plates to prevent three-dimensional flow at the ends of bluff cylinders. *UK NPL Aero.* **C.P. 683,** 1-12.

CVI Laser Optics LLC. 2007 *CVI laser optics, components and assemblies.* http://www.cvilaser.com

Dunn W. 1997 *Visualization of Flow Past a Model of the CF-18 Aircraft in a Water Tunnel.* MASc Thesis. Department of Mechanical Engineering, University of Ottawa, Ottawa, Ontario, Canada.

Dunn W. 2004 *Vortex Shedding from Cylinders with Step-Changes in Diameter in Uniform and Shear Flows.* Doctoral Dissertation. Department of Mechanical Engineering, University of Ottawa, Ottawa, Ontario, Canada.

Dunn, W. and Tavoularis, S. 2006 Experimental studies of vortices shed from cylinders with a step-change in diameter. *J. Fluid Mech.* **555,** 409-437.

Eiff, O. S., Kawall, J. G. and Keffer, J. F. 1995 Lock-in of vortices in the wake of an elevated round turbulent jet in a crossflow. *Exp. Fluids* **19,** 203-213.

Eiff, O. S. and Keffer, J. F. 1997a On the structures in the near-wake region of an elevated turbulent jet in a crossflow. *J. Fluid Mech.* **333,** 161-195.

Eiff, O. S. and Keffer, J. F. 1997b Aspects of ring vortex lock-in for the turbulent jet discharging from a stack. *Exp. Therm. Fluid Sci.* **14,** 52-59.

Eiff, O. S. and Keffer, J. F. 1999 Parametric investigation of the wake-vortex lock-in for the turbulent jet discharging from a stack. *Exp. Therm. Fluid Sci.* **19,** 57-66.

Fric, T. F. and Roshko, A. 1994 Vortical structure in the wake of a transverse jet. *J. Fluid Mech.* **279,** 1-47.

Fröhlich, J. and Rodi, W. 2004 LES of the flow around a circular cylinder of finite height. *Int. J. Heat. Fluid Flow* **25,** 537-548.

Gopalan, S., Abraham, B. M. and Katz, J. 2004 The structure of a jet in cross flow at low velocity ratios. *Phys. Fluids* **16,** 2067-2087.

Hasselbrink, E. F. and Mungal, M. G. 2001 Transverse jets and jet flames. Part 1. Scaling laws for strong transverse jets. *J. Fluid Mech.* **443,** 1-25.

Hsieh, R. H. and Huang, R. F. 2003 Tomographic flow structures of a round jet in a crossflow. *J. Chin. Inst. Eng.* **26,** 71-80.

Huang, R. F. and Hsieh, R. H. 2002 An experimental study of elevated round jets deflected in a crosswind. *Exp. Therm. Fluid Sci.* **27,** 77-86.

Huang, R. F. and Hsieh, R. H. 2003 Sectional flow structures in near wake of elevated jets in a crossflow. *AIAA J.* **41,** 1490-1499.

Huang, R. F. and Lan, J. 2005 Characteristic modes and evolution processes of shear-layer vortices in an elevated transverse jet. *Phys. Fluids* **17,** 1-13.

ISS Inc. 2007 *Excitation and emission wavelengths of fluorophores - resources - ISS.* http://www.iss.com/resources/spectra.html

Johnson, M. R. and Kostiuk, L. W. 2000 Efficiencies of low-momentum jet diffusion flames in crosswinds. *Combust. Flame* **123,** 189-200.

Johnson, M. R., Wilson, D. J. and Kostiuk, L. W. 2001 A fuel stripping mechanism for wake-stabilized jet diffusion flames in crossflow. *Combust. Sci. Technol.* **169,** 155-174.

Johnson, M. R. and Kostiuk, L. W. 2002 A parametric model for the efficiency of a flare in crosswind. In *Twenty-Ninth International Symposium on Combustion Hokkaido University Sapporo Japan, 21-25 July 2002, Sapporo,* 1943-1950.

Kawamura, T., Hiwada, M., Hibino, T., Mabuchi, I. and Kumada, M. 1984 Cylinder height greater than turbulent boundary-layer thickness - flow around a finite circular-cylinder on a flat-plate. *Bull. JSME* **27,** 2142-2151.

Kelso, R. M., Lim, T. T. and Perry, A. E. 1996 An experimental study of round jets in cross-flow. *J. Fluid Mech.* **306,** 111-144.

Kelso, R. M., Lim, T. T. and Perry, A. E. 1998 New experimental observations of vortical motions in transverse jets. *Phys. Fluids* **10,** 2427-2429.

Kislich-Lemyre B. C. 2002 *The Large-Scale Structure of Uniformly Sheared Turbulence and its Distorsion by a Solid Wall at Rest Or in Motion.* Doctoral Dissertation. Department of Mechanical Engineering, University of Ottawa, Ottawa, Ontario, Canada.

Lindsay, K. A. 1984 The kelvin-helmholtz instability for a viscous interface. *Acta Mech* **52,** 51-61.

Margason, R. J. 1993 Fifty years of jet in cross flow research. In *AGARD Meeting on 'Computational and Experimental Assessment of Jets in Cross Flow', April 19-22, 1993, Winchester, UK,* 1-1-1-41.

Morton, B. R. 1984 The generation and decay of vorticity. *Geophys. Astrophys. Fluid Dynamics* **28,** 277-308.

Moussa, Z. M., Trischka, J. W. and Eskinazi, S. 1977 Near field in the mixing of a round jet with a cross-stream. *J. Fluid Mech.* **80,** 49-80.

Munson, B. R., Young, D. F. and Okiishi, T. H. 2002 *Fundamentals of Fluid Mechanics.* John Wiley & Sons, Inc. New York, New York.

OPTIKON Corp. 1996 *Model 95 Ion Laser Operator's Manual.* OPTIKON Corporation. Kitchener, Ontario, Canada.

Overcamp, T. J. and Ku, T. 1986 Effect of a virtual origin correction on entrainment coefficients as determined from observations of plume rise. *Atmos. Environ.* **20,** 293-300.

Panton, R. L. 2005 *Incompressible Flow.* John Wiley & Sons, Inc. Hoboken, New Jersey.

Park, C. W. and Lee, S. J. 2000 Free end effects on the near wake flow structure behind a finite circular cylinder. *J. Wind Eng. Ind. Aerodyn.* **88,** 231-246.

Park, C. W. and Lee, S. J. 2004 Effects of free-end corner shape on flow structure around a finite cylinder. *J. Fluids Struct.* **19,** 141-158.

Roh, S. C. and Park, S. O. 2003 Vortical flow over the free end surface of a finite circular cylinder mounted on a flat plate. *Exp. Fluids* **34,** 63-67.

Rosenhead, L., ed. 1963 *Laminar Boundary Layers.* Oxford University Press. Oxford, UK.

Sivadas, V., Pani, B. S., Büttefisch, K. A. and Meier, G. E. A. 1997 Flow visualisation studies on growth of area of deflected jets. *Exp. Fluids* **23,** 105-112.

Smith, S. H., Lozano, A., Mungal, M. G. and Hanson, R. K. 1993 Scalar mixing in the subsonic jet in crossflow. In *AGARD Meeting on 'Computational and Experimental*

Assessment of Jets in Cross Flow', April 19-22, 1993, Winchester, UK, 6-1-6-13.

Smith, S. H. and Mungal, M. G. 1998 Mixing, structure and scaling of the jet in crossflow. *J. Fluid Mech.* **357,** 83-122.

Su, L. K. and Mungal, M. G. 2004 Simultaneous measurements of scalar and velocity field evolution in turbulent crossflowing jets. *J. Fluid Mech.* **513,** 1-45.

Sumner, D., Heseltine, J. L. and Dansereau, O. J. P. 2004 Wake structure of a finite circular cylinder of small aspect ratio. *Exp. Fluids* **37,** 720-730.

Szepessy, S. 1993 On the control of circular cylinder flow by end plates. *Eur. J. Mech. , B/Fluids* **12,** 217-243.

Szepessy, S. and Bearman, P. W. 1992 Aspect ratio and end plate effects on vortex shedding from a circular cylinder. *J. Fluid Mech.* **234,** 191-217.

Tatom, F. B. 1986 Prediction of stack plume downwash. *J. Fluids Eng. -Trans. ASME* **108,** 379-382.

Tavoularis, S. 2005 *Measurement in Fluid Mechanics.* Cambridge University Press. New York, New York.

Wark, K. and Warner, C. F. 1981 *Air Pollution: Its Origin and Control.* Harper & Row, Publishers, Inc. New York, N.Y.

Yuan, L. L. and Street, R. L. 1998 Trajectory and entrainment of a round jet in crossflow. *Phys. Fluids* **10,** 2323-2335.

Yuan, L. L., Street, R. L. and Ferziger, J. H. 1999 Large-eddy simulations of a round jet in crossflow. *J. Fluid Mech.* **379,** 71-104.

Zdravkovich, M. M. 1997 *Flow Around Circular Cylinders, Volume 1: Fundamentals.* Oxford University Press. Oxford, England.

Zdravkovich, M. M. 2003 *Flow Around Circular Cylinders, Volume 2: Applications.* Oxford University Press. New York, N.Y.

Appendix A Optical Calculations

Laser Doppler velocimetry measurements were taken through an interface with differing indices of refraction and the LDV head was moved perpendicularly to the interface. As such, the difference of movement of the LDV head and the measurement volume needed to be accounted for. The calculations for this are found here:

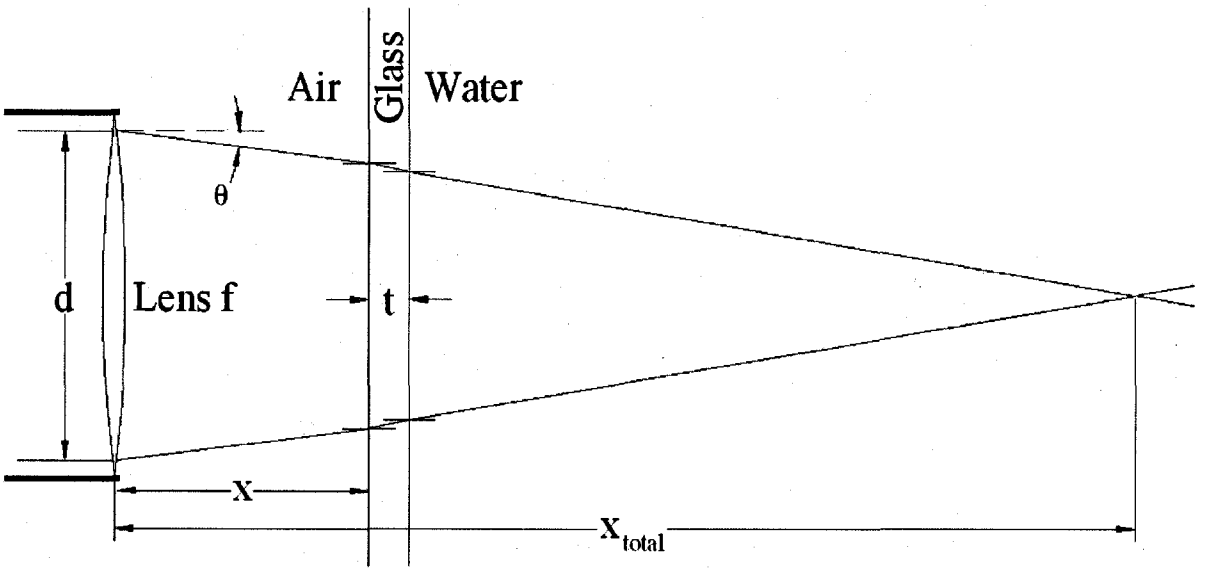

$$X_{total} := a \cdot x + b$$

where

$$a := \left(1 - \frac{\sqrt{n_w^2 - n_a^2 \sin(\theta)^2}}{n_a \cdot \cos(\theta)} \right)$$

$$b := \left(1 - \frac{\sqrt{n_w^2 - n_a^2 \sin(\theta)^2}}{\sqrt{n_g^2 - n_a^2 \sin(\theta)^2}} \right) t + \left(\frac{\sqrt{n_w^2 - n_a^2 \sin(\theta)^2}}{2 n_a \cdot \sin(\theta)} \right) d$$

n_a - index of refraction of air

n_g - index of refraction of glass

n_a - index of refraction of water

Appendix B LDV Settings

LDV Settings from Dantec BSA Flow Software	
Property	Processor Setting
Load SWunits	0
Hardware Mode	0
Transmission packet size	512
Max time between data packets	500
System monitor update frequency	30
Minimum time between calibration	15
Input channel block size	2048
Burst update frequency.	30
Leak step.	0.5
Calibration AC modulation	10
Record Calibration measurement	0
Leak timer	0
eProm version	0
Numbers Of PCBuffers	300
DSP FIFO Size	10
Minimum Peak	0
High voltage activation	1
Anode current warning level	90
Data collection mode	0
Duty-cycle	100
Dead-time	0
Calibration mode	0
40 MHz frequency shift	1
Variable frequency shift	0
Variable shift frequency	40000000

Property	Group 1 Setting	Group 2 Setting
Max. samples	1000000	5000
Max. acquisition time	60	30
Filter method	1	1
Burst window	0	0
Scope zoom	400	400
Spherical validation	0	0
Encoder data	0	0
High voltage	0	0
Invalid data	0	0

Property	LDA1 Setting	LDA2 Setting
Center frequency	0	0
Bandwidth	234375	234375
Record length	128	128
High voltage level	1600	1600
Signal gain	30	30
Burst detector SNR level	0	0
Scope display	1	1
Scope trigger channel	-1	-1
Decimation filter	0	0
Burst frequency	10000	10000
Burst type	0	0
Auto leaktuning	1	1
Leaktuning	1	1
Leak trim 1	0	0
Leak trim 2	0	0
Graph of Leaktuning	0	0
Kvadratur dump	0	0
Leak dump	0	0
HW Test	0	0
Offset Q	1.3	1.3
Offset I	1.7	1.7
Gain balance	5	5
Phase balance	1	1
Scope samples	1024	1024
Anode current limit	1500	
Frequency shift	1	1
Frequency shift direction	0	0
External shift frequency	30000000	30000000
Anode cut		1500

Property	Optical LDA System - U1	Optical LDA System - U2
Wavelength	514.5	488
Focal length	310	310
Beam diameter	1.35	1.35
Expander ratio	1.95	1.95
Beam spacing	38	38
Number of fringes	35	35
Fringe spacing (um)	2.168	2.056
Beam half-angle (deg)	6.815	6.815
Probe volume - dx (mm)	0.078	0.074
Probe volume - dy (mm)	0.077	0.073